



Recent progress of all-polymer solar cells – From chemical structure and device physics to photovoltaic performance



Hang Yin^{a,1,***}, Cenqi Yan^{b,1,***}, Hanlin Hu^{c,1,****}, Johnny Ka Wai Ho^a, Xiaowei Zhan^d, Gang Li^b, Shu Kong So^{a,*}

^a Department of Physics and Institute of Advanced Materials, Hong Kong Baptist University, Kowloon Tong, Hong Kong Special Administrative Region

^b Department of Electronic and Information Engineering, The Hong Kong Polytechnic University, Hung Hom, Kowloon, Hong Kong Special Administrative Region

^c Shenzhen Key Laboratory of Polymer Science and Technology, College of Materials Science and Engineering, Shenzhen University, Shenzhen 518057, PR China

^d Department of Materials Science and Engineering, College of Engineering, Key Laboratory of Polymer Chemistry and Physics of Ministry of Education, Peking University, Beijing 100871, PR China

ARTICLE INFO

Keywords:

All-polymer solar cells
Organic solar cells
Chemical structure
Device physics
Electron transport

ABSTRACT

Single junction organic solar cells (OSCs) have now achieved power conversion efficiencies (PCEs) exceeding 17 %. Most of these high performance OSCs contain fullerene acceptors (FAs) and non-fullerene small-molecule acceptors (NFSMAs). In contrast, there are very limited usages of polymer acceptors. Recently, there are escalating recognition among perylene-diimide/naphthalene-diimide (PDI/NDI) and B—N-unit n-type polymers as electron acceptors in the all-polymer solar cells. FAs like PC₇₁BM suffer from multiple limitations. They include restricted energy level tuning, weak absorptions in visible region, narrow spectral breadth, and morphological instability. In contrast to FAs, NFSMAs offer numerous advantages. They include strong and broad absorption in the visible and even the NIR region, tunable energy levels, and simple synthesis and purification procedures. Despite these advantages, the long-term device stability and large-area roll-to-roll (R2R) fabrication remain the major issues for the commercialization for NFSMA-based OSCs. All-polymer solar cells, on the other hand, largely address the problems of device stability and large-area film processing. Many all-polymer solar cells have been demonstrated to possess long-term thermal, photo and mechanical stability. Meanwhile, the precursor solutions for all-polymer solar cells enjoy superior control in the solution viscosity, which is an important factor for the solution processing of large-scale OSCs. Before 2015, all-polymer solar cells received little attention due to their disappointing device performance. Afterwards, PCEs of all-polymer solar cells are picking up. Currently, the best cells have achieved PCEs in excess of 11 %. Here, we provide a systematic review on the evolution of n-type polymeric acceptors used in OSCs. In addition, we summarize the morphological and charge carrier transport properties of all-polymer solar cells and compare with their small molecule acceptor counterparts. The outstanding properties of all-polymer solar cells are discussed from the perspectives of morphology and electron transport in bulk heterojunctions (BHJs). The concept of electron percolation in all-polymer BHJs is introduced and correlated with the excellent device stability. This review should have a broad appeal and enable researchers in comprehending the achievements, challenges, and future directions of all-polymer solar cells.

1. Introduction

The gigantic growth in energy demands worldwide has caused serious environmental pollution and global energy shortages [1–4]. As alternatives to fossil fuels, renewable energy resources could potentially

be a resolution and address the need for sustainable development [5–11]. According to the statistical data in 2016 from the World Energy Council, the renewable energy consumption has increased worldwide gradually over the years of 2005, 2010, and 2015. In particular, unprecedented demand for developments in solar-power generation has

* Corresponding author.

** Corresponding author.

*** Corresponding author.

**** Corresponding author.

E-mail address: skso@hkbu.edu.hk (S.K. So).

¹ These authors contribute equally to this work.

been revealed. The installed gross capacity of photovoltaic (PV) panels reached 227 GW in 2015, supplying about 1 % of the global electricity consumption.

Organic photovoltaic (OPV) solar cells have been steadily developed over the past decade. They are expected to have great potential in the solar industry because of their low costs, mechanical flexibility, excellent processability, and the capability of large-area roll-to-roll (R2R) manufacturing [12–15]. The development of fused-ring electron acceptors (FREAs) [16–25] has allowed record power conversion efficiencies (PCEs) to exceed 17 % for both single-junction and tandem bulk-heterojunction (BHJ) devices [26,27]. However, the long-term device stability and large-area R2R processing techniques must be improved for both fullerene-based and non-fullerene (NF) small-molecule-acceptor (SMA)-based OPV cells before they are ready for commercialization [28–30].

Encouragingly, all-polymer solar cells largely address such problems in organic solar cells (OSCs) [31]. All-polymer solar cells are a kind of OPV cells with a bulk heterojunction (BHJ) active layer of a polymeric electron donor and a polymeric electron acceptor. The ‘all-polymer’ concept can be compared with the ‘small-molecule’ (SM) concept in three types of BHJ films: (i) polymer donor + SM acceptor; (ii) SM donor + polymer acceptor; and (iii) all-SM BHJ films. While (ii) is less studied, a comparison between the all-polymer BHJs and the SM-based (i) and (iii) reveals a distinct feature in the all-polymer cells that electron carriers may migrate over the long chains of the polymeric acceptor [32–34]. This unique feature, as it turns out, leads to special advantages for all-polymer solar cells. We will discuss these advantages in the latter part of this review.

Although the efficiency of all-polymer solar cells is lagging behind the SMA-based solar cells, all-polymer solar cells surpass the SMA-based solar cells in long-term thermal, photo- and mechanical stability. The

precursor solutions or all-polymer cells possess better control of solution viscosity, which is an important factor for solution-processing of large-scale OSCs [35–37]. All-polymer solar cells received little attention before 2015 due to their disappointing device performance. However, their efficiencies have then rapidly increased to more than 11 %, comparable to their SMA counterparts [38]. Meanwhile, extensive mechanistic studies have revealed the optical and electronic properties of all-polymer solar cells [39,40]. Fig. 1 summarizes the all-polymer solar cell power conversion efficiencies (PCEs) using different n-type polymer acceptors, together with the chemical structures of their electron-accepting moieties.

In this review, we summarize the evolution of n-type polymeric acceptors used in all-polymer solar cells. Then, we discuss their morphological and charge carrier transport properties and compare them with their SMA counterparts. Typically, n-type polymeric acceptors can be classified into cyanated polyphenylenevinylanes (CN-PPV), benzothiadiazole-based polymers, rylene diimide polymers, diketopyrrolopyrrole based polymers, B←N based polymers, indacenodithiophene based polymers, and bithiophene imide based polymers. By varying the chemical structures, the electronic, optical and morphological characteristics of these classes of materials can be extensively modulated for various donor materials. Some all-polymer BHJs achieve PCEs rivaling those of other types of OSCs. Mechanistically speaking, control of the molecular weight of polymer donors and polymer acceptors and of their relative ratio is critical for strong intermolecular assembly of both the donor and the acceptor. This is a crucial factor for the charge transport properties and phase separation. Although large-scale phase separation often occurs in all-polymer solar cells, it can be controlled by engineering the molecular weights, blend ratios, and the solution process. Particularly, the morphology of all-polymer solar cells can be subtly tuned by post-treatment. After the discussion of morphology, the

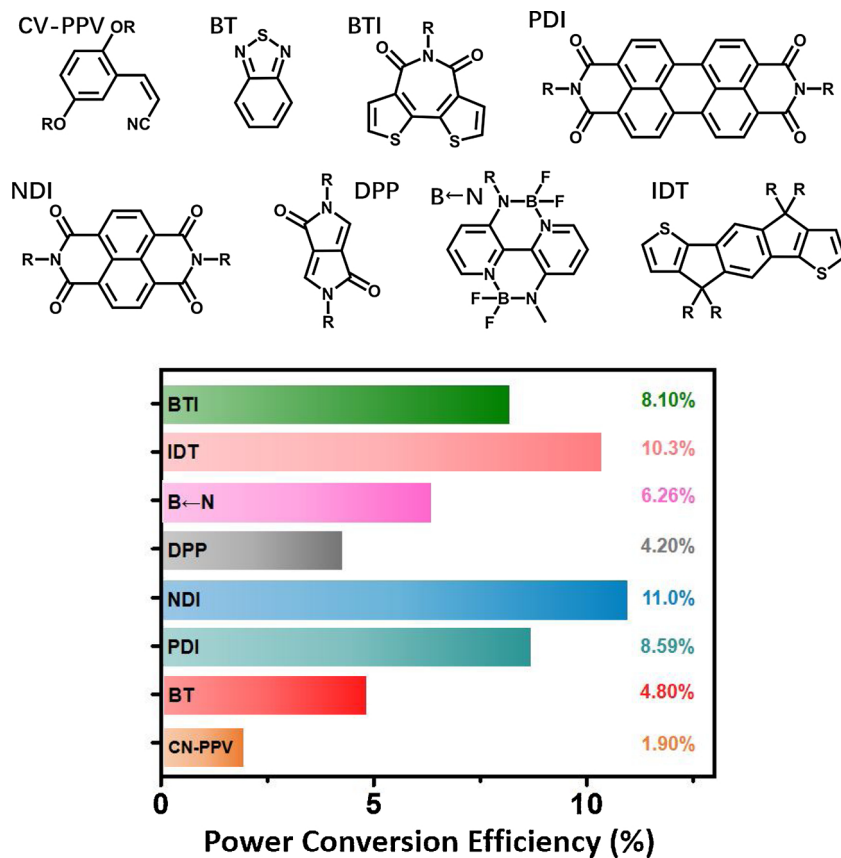


Fig. 1. Recorded power conversion efficiencies (PCEs) of all-polymer solar cells with different n-type polymer acceptors, together with the chemical structures of their electron-accepting moieties.

electron transport properties in all-polymer BHJs are reviewed and compared with other types of BHJs. From the electron transport data, we observe that electrons transport advantageously in a polymer BHJ with suppressed Poole-Frenkel effect and reduced energetic disorder. We deduce that the electron-transporting pathway in all-polymer BHJs must be superior to that in other types of OSCs. As a result, all-polymer BHJs are highly tolerant to compositional variations. This review targets a wide scientific community to help researchers appreciate the achievements, understand the challenges, and gain insights into future development directions of all-polymer solar cells.

2. Chemical structures of polymeric electron acceptors

Well-developed polymeric electron-accepting materials can be broadly classified into seven categories: cyanated poly(phenylenevinylene)s, benzothiadiazole-based polymers, rylene diimide polymers, diketopyrrolopyrrole-based polymers, B—N-based polymers, indacenodithiophene-based polymers, and bithiophene imide-based polymers. The electronic, optical, and morphological characteristics of polymer acceptors can be extensively modulated through variations in chemical structures to allow for matching with various donor materials and leading to polymer acceptors with PCE values that, in some cases, rival those found for other types of OSCs. Fig. 2 shows selected donor materials that are used in typical all-polymer BHJ solar cells.

polymers, diketopyrrolopyrrole-based polymers, B—N-based polymers, indacenodithiophene-based polymers, and bithiophene imide-based polymers. The electronic, optical, and morphological characteristics of polymer acceptors can be extensively modulated through variations in chemical structures to allow for matching with various donor materials and leading to polymer acceptors with PCE values that, in some cases, rival those found for other types of OSCs. Fig. 2 shows selected donor materials that are used in typical all-polymer BHJ solar cells.

2.1. Cyanated poly(phenylenevinylene)s

Conjugated polymers based on cyanated poly(phenylenevinylene) (CN-PPV) backbones [chemical structures in Fig. 3(a)] were first investigated independently by Friend et al. [41] and by Heeger et al. [42]. Both teams demonstrated that the BHJ strategy provided the spatially

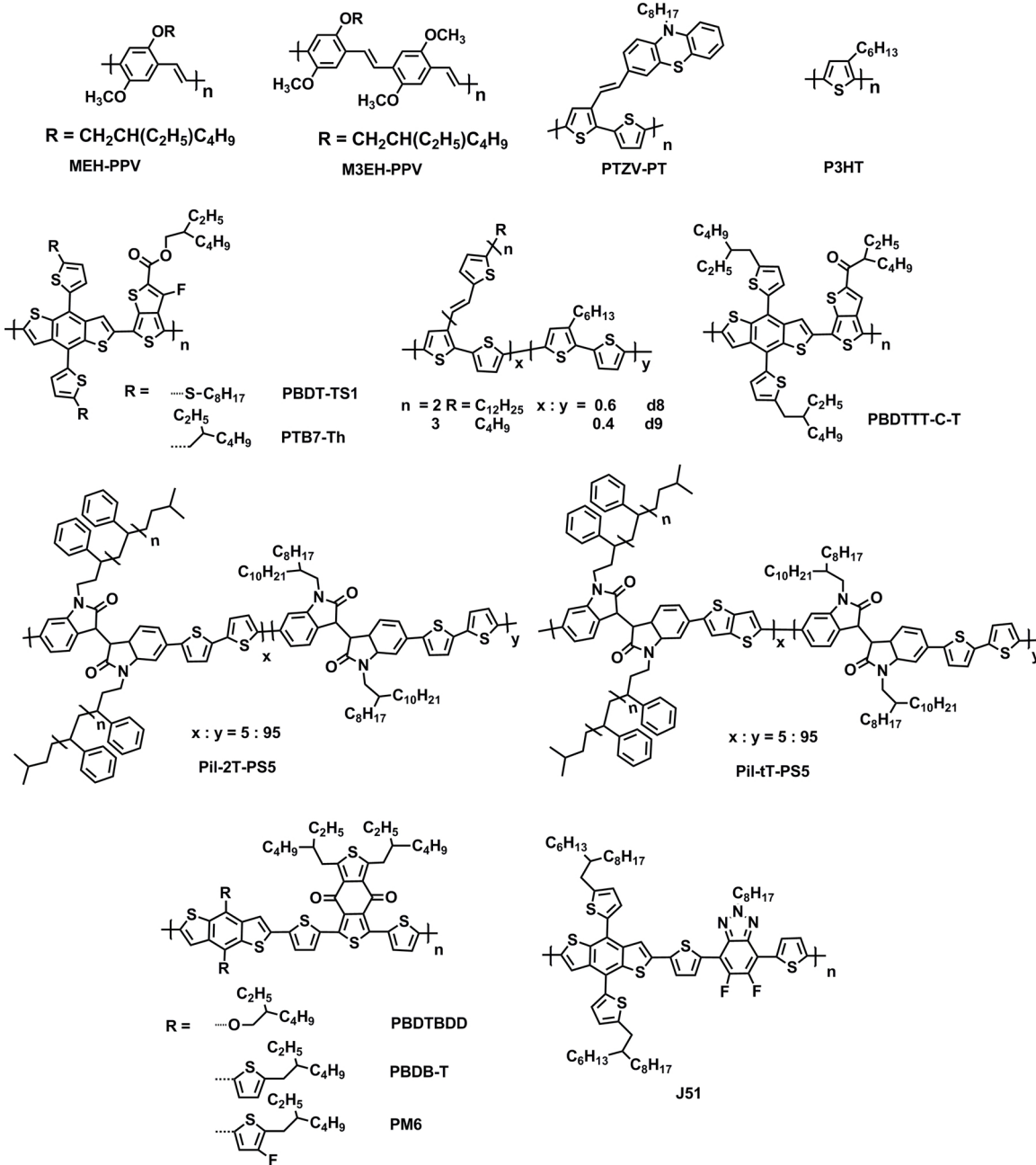


Fig. 2. Chemical structures of selected polymeric donors used in all-polymer BHJ solar cells.

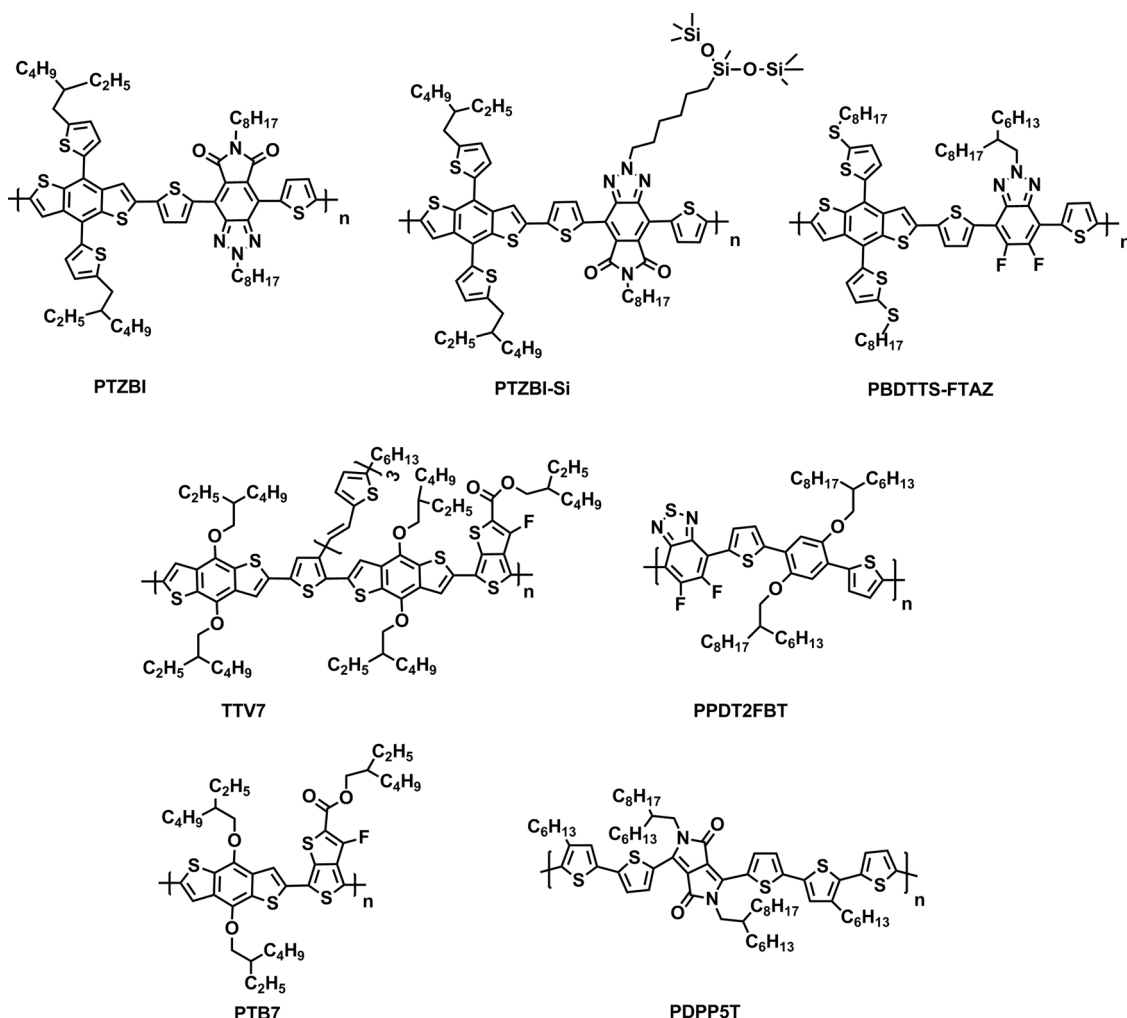


Fig. 2. (continued)

distributed interfaces necessary for efficient exciton dissociation. Friend et al. used a mixture of donor 2-methoxy-5-(2'-ethylhexyloxy)-*p*-phenylene vinylene (MEH-PPV) and acceptor C6-CN-PPV to fabricate all-polymer solar cells and investigated their blend-phase segregation using transmission electron microscopy (TEM), scanning tunneling electron microscopy (STEM), and parallel electron-energy-loss spectroscopy (PEELS). These devices exhibited a photoresponse with an open-circuit voltage (V_{OC}) of 0.6 V and external quantum efficiencies (EQEs) of up to 6 %, which increased substantially to 15 % and 40 % at reverse biases of 3.5 and 10 V, respectively. These performances were superior to those measured for MEH-PPV (0.04 %) and C6-CN-PPV ($\sim 10^{-3}$ %) pure films. In the parallel study by Heeger and coworkers [32], devices based on MEH-PPV donors and MEH-CN-PPV acceptors exhibited EQEs of ~ 5 % and PCEs of ~ 0.9 % ($V_{OC} = 1.25$ V), which were 15–25 times and 100 times greater than photodiodes fabricated with pure MEH-PPV and MEH-CN-PPV, respectively. The absorption and photoluminescent spectra from MEH-PPV, CN-PPV, and CN-PPV:MEH-PPV blends indicated only the occurrence of photoinduced charge transfer, and no ground-state charge transfer was evident. In a further study, Friend and coworkers [43] exploited POPT and MEH-CN-PPV to fabricate laminated two-layer devices, which achieved an EQE of 29 % at 480 nm excitation and PCE of 1.9 % with fill factor (FF) of ~ 30 % to 35 %. Carter and co-workers reported that single-polymer devices based on poly(2-methoxy-5-(2'-ethylhexyloxy)-1,4-phenylene-1,2-ethenylene-2,5-dimethoxy-1,4-phenylene-1,2-ethenylene) (M3EH-PPV) with a TiO₂/polymer/Au configuration displayed a PCE of 0.40 %; whereas dipolymer devices that comprise blends of M3EH-PPV and CN-ether-

PPV afforded a PCE of 0.75 % when their electrodes had the same compositions and a PCE of 1.0 % when their electrodes comprised poly(3,4-ethylenedioxythiophene) (PEDOT) and Ca [44].

Neher and coworkers reported detailed studies on M3EH-PPV:CN-ether-PPV blends [45]. They proposed that as M3EH exhibited much poorer solubility in chlorobenzene (CB) than CN-ether-PPV, using CB as a solvent during spin-coating lead to the formation of a vertical composition-graded layer, rather than a homogeneous blend. This created a nearly ideal structure for exciton separation and charge transport and yielding PCEs of up to 1.7 %, with a maximum EQE of 31 % ($V_{OC} = 1.36$ V, FF = 35 %, I_{SC} (short-circuit current) = 3.54 mA).

Li and coworkers fabricated all-polymer solar cells using phenothiazine-vinylene polythiophene (PTZV-PT) donors and poly(1,4-diethoxyxyl-p-2,5-dicyanophenyl-enevinylene) DOCN-PPV acceptors [46]. Strong photoluminescence quenching was observed in the polymer blend, indicating efficient charge separation existed. Post-annealing at 120 °C for 15 min led to a rougher surface and a more extensively interpenetrating network, and thus resulted in a twofold increase in PCE (from 0.41 % to 0.8 %).

2.2. Benzothiadiazole-based polymers

The strongly electron-withdrawing benzothiadiazole (BTD) heterocycle has been often incorporated into linear conjugated donor-acceptor polymers via its C4 and C7 positions. BTD-based polymers have high electron affinity, low bandgaps, favorable π - π intermolecular interactions, and ordered crystal packing. Some representative BTD-based

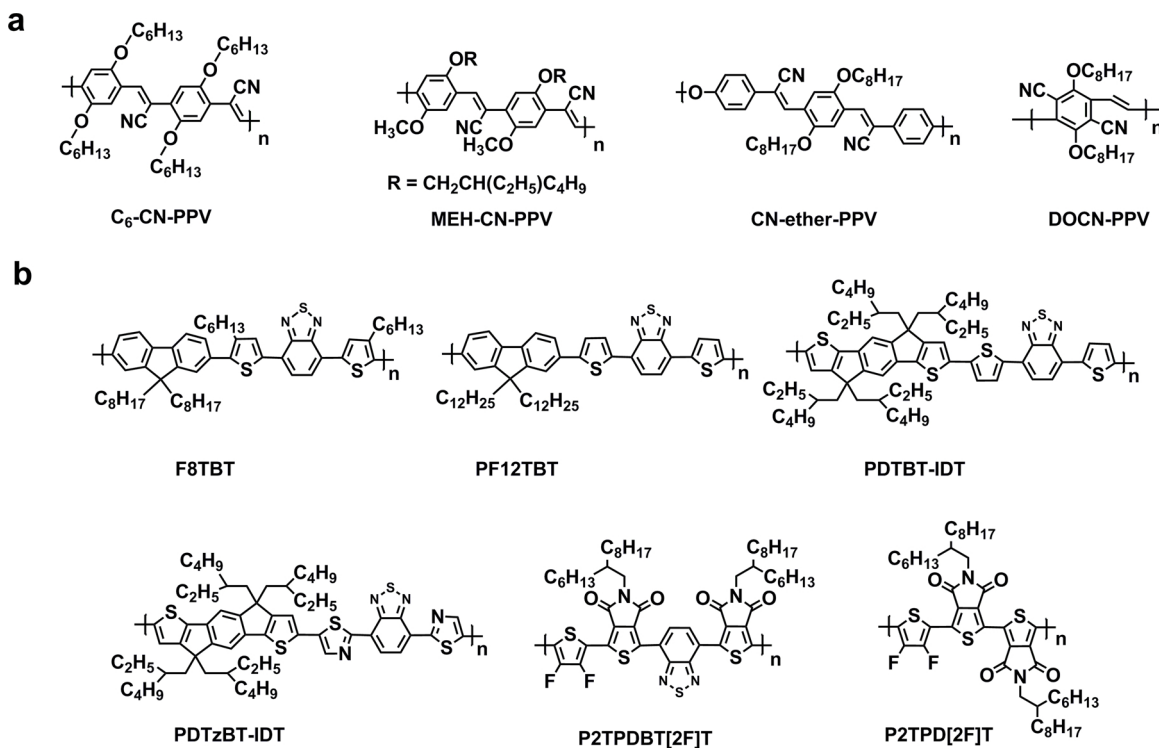


Fig. 3. (a). Chemical structures of selected PPV-based polymeric acceptors. (b). Chemical structures of selected Benzothiadiazole-based polymeric acceptors.

Polymer acceptors are shown in Fig. 3(b), and their corresponding optoelectronic and PV properties are summarized in Table 1.

Poly[(9,9-dioctylfluorene)-2,7-diyl-alt-(4,7-bis(3-hexylthien-5-yl)-2,1,3-benzothiadiazole)-2',2"-diyl] (F8-TBT) copolymers were originally developed as red-emitting polymers for light-emitting diode (LED) applications that require a low TBT concentration (~15 %), because a high chromophore concentration is detrimental to electroluminescence efficiency [51]. In contrast, a 1:1 composition ratio of F8 to TBT is advantageous for PV applications due to the higher absorption cross-section of this mixture. F8TBT, as used by Friend and coworkers, displayed an ambipolar nature (HOMO of -5.37 eV and LUMO of -3.15 eV) and broad absorption from 300 to 700 nm [47]. A P3HT:F8TBT blend (where P3HT is poly(3-hexylthiophene)) displayed a PCE of 1.8 %.

Miyake and coworkers found that poly{2,7-(9,9-didodecyl-fluorene)-alt-5,5-[4',7'-bis(2-thienyl)-2',1',3'-benzothiadiazole]} (PF12TBT), an analog of F8TBT, displayed PV performance sensitive to processing solvent and thermal annealing. A PCE of 2.0 % was obtained for PF12TBT that had been fabricated by nanoscale phase-separation by spin-coating from chloroform and subjected to thermal purification [52]. A higher PCE of 2.7 % was attained using high-molecular-weight PF12TBT (78 kDa), which favored the formation of a PF12TBT network and facilitated charge generation and transport [48].

Pei and coworkers designed poly{2,7-(9,9-didodecyl-fluorene)-alt-5,5-[4',7'-bis(2-thiazolyl)-2',1',3'-benzothiadiazole]} (PDTzBT-IDT) by replacing the thiophene bridge in PDTBT-IDT with thiazole. Because thiazole has stronger electron-withdrawing ability than thiophene, PDTzBT-IDT exhibited a lower HOMO and LUMO and thus had electron mobilities almost two orders of magnitude greater than those of PDTBT-IDT. P3HT:PDTzBT-IDT blends showed a PCE of 1.18 %, twice as high as that of P3HT:PDTBT-IDT blends [49].

In the work of Beaujuge and coworkers, P2TPDBT[2F]T, composed of thiopyrroledione (TPD), difluorothiophene ([2F]T), and BT, afforded a higher PCE (4.8 %) than the BT-free P2TPD[2F]T (2.6 %) in a PBDT-TS1-based device [50]. The incorporation of the BT motif in the backbone narrowed the optical bandgap (from 1.9 to 1.7 eV) and increased electron mobility by two orders of magnitude.

2.3. Rylene diimide polymers

Rylene diimide polymers—that is, polymers based on perylene diimides (PDIs) and naphthalene diimides (NDIs)—are most widely used in n-type polymeric materials [53–55], due to the high electron affinity of the rylene diimide core (caused by the two strong electron-withdrawing diimide groups) and a highly extended π-conjugated structure

Table 1
Optoelectronic properties and OSC device parameters for Benzothiadiazole-based polymeric acceptors.

Acceptor	λ_{max} (nm)	E_{op} (eV)	HOMO/LUMO (eV)	μ_e ($\text{cm}^2 \text{V}^{-1} \text{s}^{-1}$)	Donor	V_{OC} (V)	J_{SC} (mA cm^{-2})	Fill Factor (%)	Highest PCE (%)	Refs.
F8TBT	525	2.22	-5.37/-3.15	8×10^{-5c}	P3HT	1.15	3.60	34	1.20	[47]
L-PF12TBT	550	2.00	-5.50/-3.50	—	P3HT	1.22	3.80	41	1.90	[48]
M-PF12TBT	550	2.00	-5.50/-3.50	—	P3HT	1.24	3.30	50	2.04	[48]
H-PF12TBT	550	2.00	-5.50/-3.50	—	P3HT	1.26	3.88	55	2.70	[48]
P1	610	1.92	-5.43/-3.45	2.9×10^{-4c}	P3HT	1.00	2.60	45	1.18	[49]
P2	595	2.07	-5.28/-3.21	1.1×10^{-2c}	P3HT	0.90	1.50	43	0.58	[49]
P2TPD[2F]T	584	1.76	-5.90/-4.14	2.4×10^{-7d}	PBDT-TS1	1.00	11.00	44	4.80	[50]

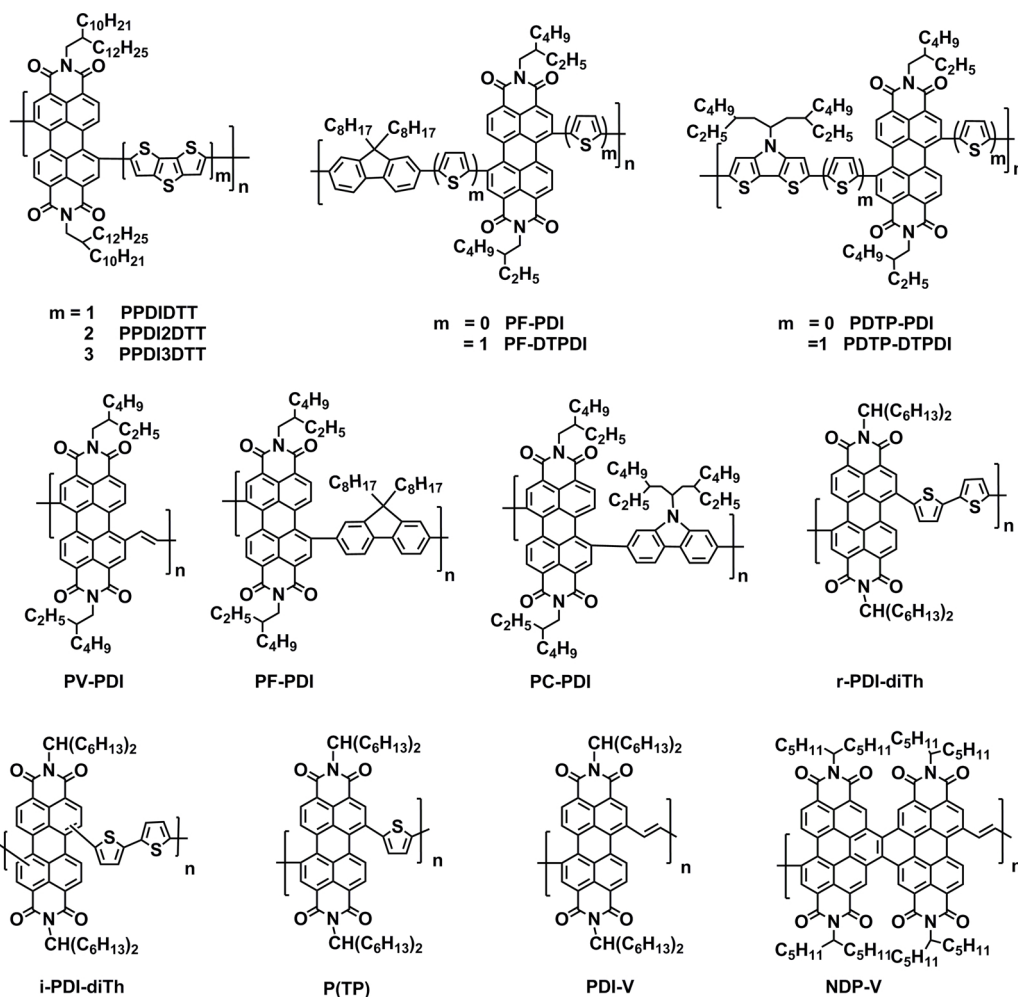


Fig. 4. Chemical structures of selected perylene diimide based polymeric acceptors.

that produces strong intermolecular $\pi-\pi$ interactions. For instance, a representative NDI-based polymer, P(NDI2OD-T2), displays high electron affinity, strong light absorption ability, and high electron mobilities of $0.85 \text{ cm}^2 \text{ V}^{-1} \text{ s}^{-1}$ in organic field effect transistor (OFET) devices and $10^{-3} \text{ cm}^2 \text{ V}^{-1} \text{ s}^{-1}$ in space-charge-limited current (SCLC) devices, attributed to the densely packed intermolecular assembly. Fig. 4 and Fig. 5 summarize chemical structures of selected perylene diimide and naphthalene diimides based polymeric acceptors, and their corresponding optoelectronic and PV properties are summarized in Table 2 and Table 3.

2.3.1. Perylene diimide polymers

The first conjugated PDI polymers, PPDIDTT, PPDI2DTT, and PPDI3DTT, designed by Zhan et al., used electron-donating dithienothiophene (DTT) and DTT oligomers as conjugated bridges [32,56–59]. Accordingly, these PDI polymers have alternating donor and acceptor character, reminiscent of many polymers that have been developed to be donors in OSCs, albeit with higher electron affinities and ionization energies. Because of the alternating donor-acceptor character, onset absorptions are seen at much lower energies in these PDI polymers than in PDI monomers. Absorption occurs over much of the visible spectrum, as a result of overlapping absorption bands that have DTT, PDI, and charge-transfer character. OSCs with d8 or d9 as the donors, and these acceptors, have yielded PCE values of 1.0%–1.5%. A higher PCE of 3.45 % was obtained for a PBDTTT-C-T:PPDIDTT blend in the presence of binary additives (PDI-2DTT and DIO) [60]. PDI-2DTT suppressed the excessive aggregation of PPDIDTT and improved donor/

acceptor mixing, and meanwhile, DIO facilitated the aggregation and crystallization of PBDTTT-C-T, synergistically contributing to the efficiency enhancement. The PCE was further increased to 4.63 % by the method of “diluting concentrated solution”, which involves the dilution of a highly concentrated polymer solution to a regular concentration immediately before spin-coating [61]. The high concentration enables close contact and entanglement of polymer chains and leads to the formation of a polymer network and thus a smaller phase separation and increased charge mobilities in blend films.

As an electron-deficient motif, PDI can be copolymerized easily with a wide variety of electron-rich units to tailor the optoelectronic properties of the resulting polymers. Copolymers of PDIs with other fused-ring bridges, including cyclopentadithiophene (CDT), fluorene, dithienopyrrole (DTP), and carbazole, and with simple aromatic bridges, such as thiophene and vinylene, have also been synthesized and examined in all-polymer solar cells.

Zhou et al. designed a series of PDI-based polymeric acceptors—PF-PDI, PF-DTPDI, PDTP-PDI, and PDTP-DTPDI—by changing the donor segment from fluorene to dithienopyrrole and introducing a thiophene spacer [62]. Polymers that contain DTP have more red-shifted absorption than their fluorine-unit containing counterparts because the DTP moiety has stronger electron-donating ability than fluorene. In addition, the introduction of a thiophene spacer into the polymer backbone increased the conjugation of the copolymer, presumably because the decreased steric hindrance around the PDIs permits a more planar polymer conformation to form. Therefore, the energy levels and the bandgap of PDI-based polymers can be easily tailored: PDTP-DTPDI

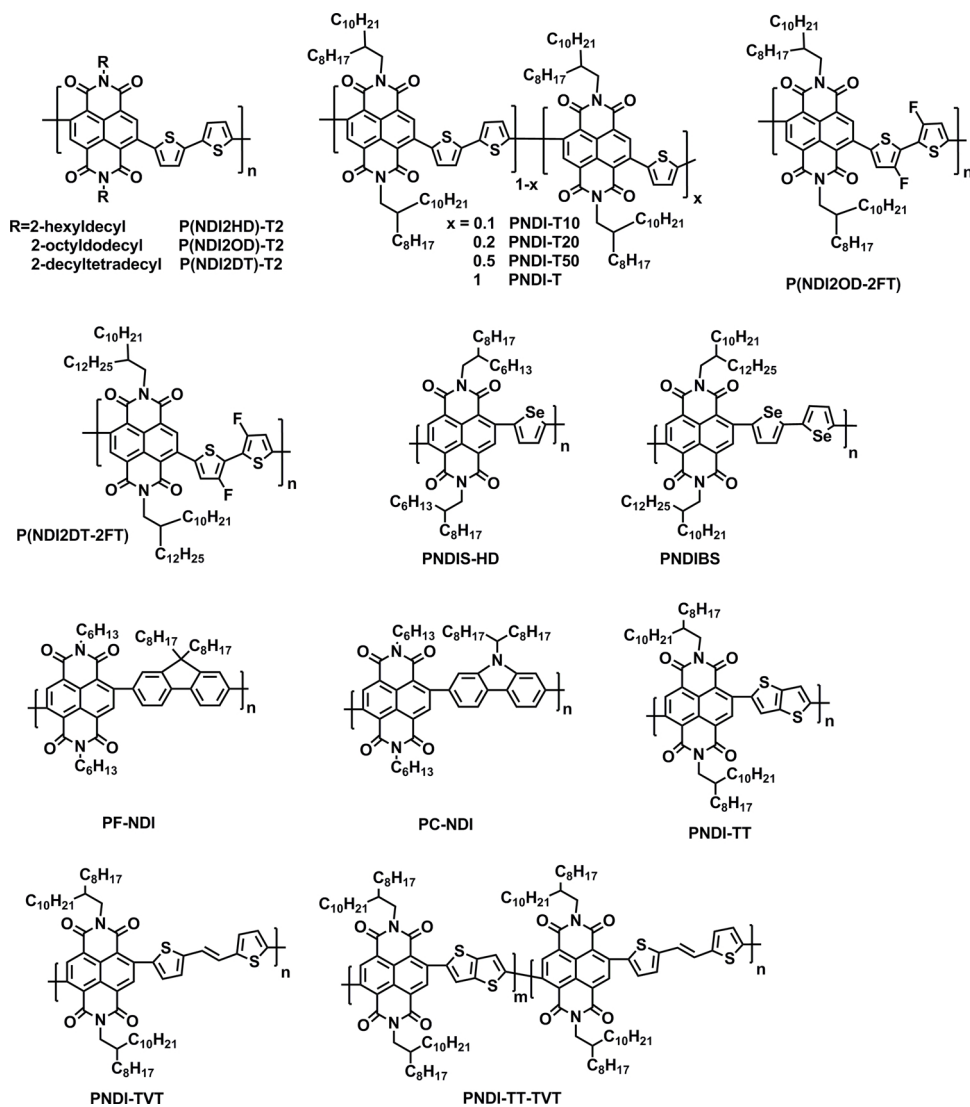


Fig. 5. Chemical structures of selected naphthalene diimide (NDI) based polymeric acceptors.

exhibited the narrowest band gap of 1.24 eV, whereas devices based on P1:PDTP-PDI exhibited the highest PCE of 0.93 %. Zhou et al. also systematically synthesized PDI-based polymeric acceptors (PX-PDIs) by copolymerizing PDI with vinylene (V), thiophene (T), DTP, fluorene (F), dibenzosilole (DBS), and carbazole (C) [63]. By changing the electron-donating segments, the LUMOs of PDI-based polymers can be tailored from 4.05 eV for PV-PDI to 3.61 eV for PF-PDI. A PT1:PC-PDI blend gave the highest PCE of 2.23 % after device optimization.

Pei and coworkers designed regio-regular r-PDI-diTh and regio-random i-PDI-diTh, with bulky and dove-tailed 1-hexylheptyls at the imide nitrogen atoms [64]. The inclusion of 1-hexylheptyl groups improved the solubility of polymeric acceptors, suppressed the inter-chain association of PDI moieties, enhanced donor/accepting mixing, and led to suitable phase segregation in the blend films. r-PDI-diTh, which had fewer structural defects than i-PDI-diTh, gave a higher PCE (2.17 %) with the P3HT donor.

Bao and co-workers reported all-polymer solar cells with PiI-2T-PS5 used as the donor and P(TP) as the acceptor, in which the highest PCE was 4.4 %, with a J_{SC} of 9.0 mA cm^{-2} and a very high V_{OC} of 1.04 V [65]. The polystyrene side chains in PiI-2T-PS5 were found to help restrict excessive phase separation, and a direct correlation was observed between the J_{SC} and the length scale of BHJ phase separation. Moreover, they adopted the method of flow-enhanced solution printing to fabricate PiI-tT-PS5:P(TP) solar cells. This strategy induced crystal

nucleation, increased polymer crystallinity, and reduced microphase separation, leading to the high PCE of 3.2 % of solution-printed solar cells [66].

Yan, Zhao, and coworkers designed PDI-V by replacing the thiophene unit in P(TP) with vinylene linkers, which reduced steric hindrance around the PDI bay region, improved backbone planarity, and therefore potentially promoted $\pi-\pi$ stacking and charge transport [67]. PDI-V exhibited a high electron mobility of $1.5 \times 10 \text{ cm}^2 \text{ V}^{-1} \text{ s}^{-1}$ in neat film and gave a PCE of 7.57 % when matched with PTB7-Th. They later constructed a vinylene-based acceptor (NDP-V) functionalized with a large naphthodiperylenetetraimide moiety that partially restricted the rotational freedom of this portion and therefore increased the polymer's backbone rigidity [68]. As a result, NDP-V displayed increased absorption, strong molecular packing, and favorable morphology, as evidenced by the increased hole and electron mobilities, factors that contributed to make its PCE (8.59 %) higher than that of PDI-V.

2.3.2. Naphthalene diimide polymers

Isolated NDIs have electron affinities comparable with PDIs and, although they absorb at higher energies than PDIs, the spectra of NDI polymers can be redshifted by combining NDI with electron-rich linkers. Conjugated NDI polymers differ from their PDI polymer analogs in that NDI polymers have less steric congestion and hence more planar

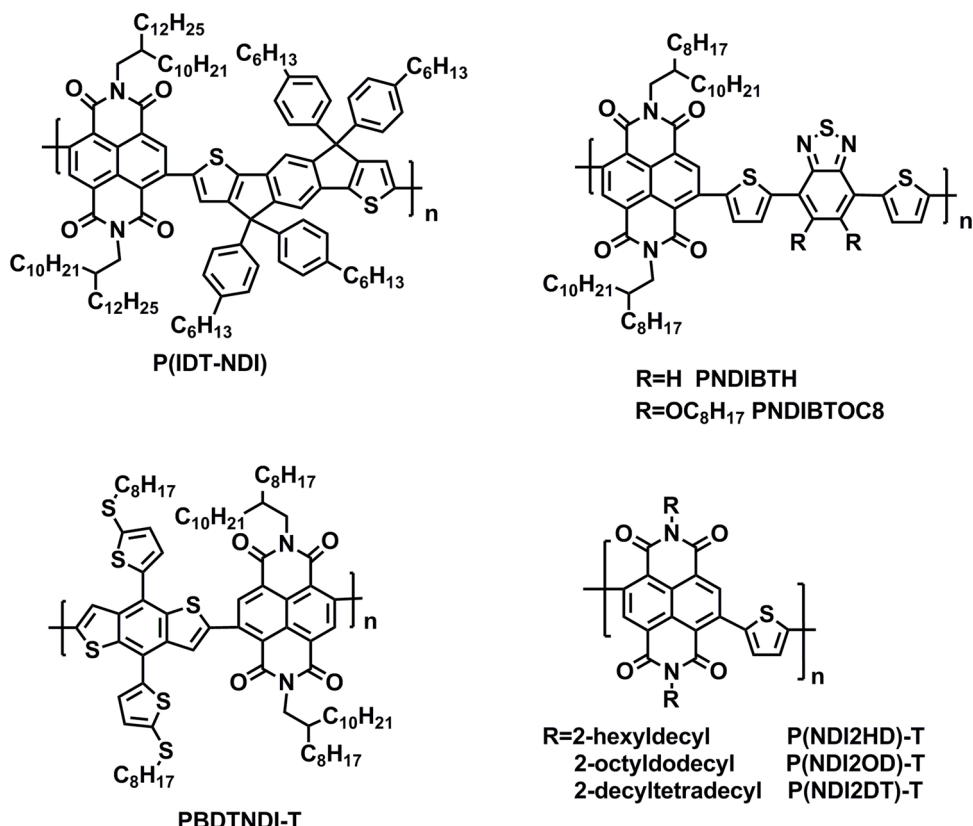


Fig. 5. (continued)

Table 2

Optoelectronic properties and OSC device parameters for perylene diimide based polymeric acceptors.

Acceptor	λ_{\max} (nm)	E_{op} (eV)	HOMO/LUMO (eV)	μ_e ($\text{cm}^2 \text{V}^{-1} \text{s}^{-1}$)	Donor	V_{OC} (V)	J_{SC} (mA cm^{-2})	Fill Factor (%)	Highest PCE (%)	Refs.
PPDIDTT	630	1.7	-5.90/-3.90	1.3×10^{-2} c	D8	0.63	4.2	39	1.03	[32]
PPDIDTT	-	-	-	-	PBDTTT-C-T	0.765	9.77	60.9	4.63	[61]
PPDI2DTT	647	1.5	-5.70/-3.80	-	D9	0.69	5.02	43	1.48	[58]
PPDI3DTT	678	1.5	-5.40/-4.00	7×10^{-4} c	D9	0.69	2.80	40	0.77	[57]
PF-PDI	326/455/570	1.77	-5.93/-3.61	-	P1	0.76	1.77	43	0.58	[62]
PF-DTPDI	376/505/623	1.57	-5.80/-3.69	-	P1	0.64	0.73	29	0.13	[62]
PDT-PDI	361/484/715	1.32	-5.49/-3.83	-	P1	0.66	3.05	46	0.93	[62]
PDT-PDPDI	441/746	1.24	-5.27/-4.00	-	P1	0.60	0.68	31	0.13	[62]
PV-PDI	-	-	-5.83/-4.05	-	PT1	0.58	2.23	38	0.48	[63]
PC-PDI	545	1.77	-5.83/-3.66	-	PT1	0.70	6.35	50	2.23	[63]
r-PDI-diTh	355	1.68	-5.5/-3.8	5×10^{-4} e	P3HT	0.52	7.65	55	2.17	[64]
i-PDI-diTh	355	1.68	-5.5/-3.8	3×10^{-4} e	P3HT	0.49	6.25	51	1.55	[64]
P(TP)	-	-	-5.60/-3.80	-	Pil-2T-PS5	1.04	8.77	46	4.21	[65]
PDI-V	353 598	1.74	-5.77/-4.03	1.5×10^{-3} e	PTB7-Th	0.74	15.9	63	7.57	[67]
NDP-V	402 547	1.91	-5.94/-4.03	2.5×10^{-3} e	PTB7-Th	0.74	17.07	67	8.59	[68]

backbones. Moreover, because dibromo-NDI precursors exist as a single isomer (the 2,6-isomer), conjugated NDI polymers are obtained as regioregular rather than regiorandom structures, which may promote electron delocalization and π stacking. In contrast, dibromo-PDI precursors are obtained as a mixture of isomers (the 1,6-isomer and 1,7-isomer) that are not easily separated.

The NDI-bithiophene copolymer P(NDI2OD-T2) (widely known as N2200) exhibits a planar structure and dense packing, has electron mobility of $0.85 \text{ cm}^2 \text{ V}^{-1} \text{ s}^{-1}$ in field-effect transistors and has been well investigated in OSCs with several donors [69]. Each polymeric donor absorbs a portion of the visible-light spectrum more or less complementary to the absorption of P(NDI2OD-T2), and each is anticipated to exhibit donor–acceptor energy offsets ($\Delta G_{CS} < 0$; however, as shown in Table 3, the PCEs vary enormously. The P3HT:P

(NDI2OD-T2) system had a PCE of only 0.2 %, most likely due to ineffective exciton dissociation and rapid geminate recombination, stemming from the hierarchical phase-separation (X-ray microscopy reveals coarse phase-separation with domain sizes of 0.2–1 μm , whereas the photoluminescence of P3HT is still efficiently quenched, which indicates that P3HT:P(NDI2OD-T2) intermixing occurs within these mesoscale domains) [70]. By using a mixed solvent of *p*-xylene and chloronaphthalene, morphology was optimized and the PCE for a P3HT:P(NDI2OD-T2) blend was improved to 1.4 %.

Hou and coworkers reported that 2D-conjugated PBDBTBD-T exhibited a higher PCE (5.8 %) than its 1D-conjugated analog, PBDBTBD, with P(NDI2OD-T2) as the acceptor. This was ascribed to the higher crystallinity in PBDBTBD-T, coupled with the distinct molecular alignment relative to both the donor–acceptor interface and the

Table 3

Optoelectronic properties and OSC device parameters for Naphthalene diimide based polymeric acceptors.

Acceptor	λ_{max} (nm)	E_{op} (eV)	HOMO/LUMO (eV)	μ_e ($\text{cm}^2 \text{ V}^{-1} \text{ s}^{-1}$)	Donor	V_{OC} (V)	J_{SC} (mA cm^{-2})	Fill Factor (%)	Highest PCE (%)	Refs.
P(NDI2OD-T2)	702	1.50	-5.52/-4.02	-	P3HT	0.52	1.41	29	0.21	[70]
P(NDI2OD-T2)	-	2.12	-5.06/-2.94	-	PBDTBDD	0.82	6.20	43	2.40	[71]
P(NDI2OD-T2)	-	2.11	-5.00/-2.89	-	PBDB-T	0.87	11.70	58	5.80	[71]
P(NDI2OD-T2)	-	1.93	-5.77/-3.84	2.16×10^{-4} d	J51	0.83	14.18	70.24	8.27	[72]
P(NDI2OD-T2)	-	-	-	5.72×10^{-5} d	PTZBI	0.844	15.48	70.1	9.16	[73]
P(NDI2OD-T2)	-	1.97	-5.81/-3.84	2.88×10^{-4} d	PTZBI-Si	0.87	15.57	74	10.10	[74]
PNDI-T10	694	2.31	-6.36/-4.05	6.0×10^{-4} d	PTB7-Th	0.83	12.9	71	7.6	[75]
PNDI-T20	680	2.32	-6.37/-4.05	1.4×10^{-4} d	PTB7-Th	0.83	9.7	52	4.2	[75]
PNDI-T50	644	2.38	-6.38/-4.00	9.5×10^{-5} d	PTB7-Th	0.83	5.8	48	2.3	[75]
P(NDI2OD-T2)	698	2.20	-6.26/-4.06	2.0×10^{-4} d	PTB7-Th	0.81	9.4	49	3.7	[78]
P(NDI2OD-TF2)	704	1.9	-5.8/-3.9	5.3×10^{-3} e	PTB7-Th	0.81	13.53	62	6.71	[80]
PNDIS-HD	-	2.16	-6.00/-3.84	6.3×10^{-2} e	PTB7-Th	0.81	18.80	51	7.73	[81]
PF-NDI	513	2.32	-5.93/-3.61	-	P3HT	0.68	3.63	66	1.63	[82]
PC-NDI	530	2.03	-5.71/-3.68	-	PTB7	0.88	4.07	38	1.34	[82]
PC-NDI	530	2.03	-5.71/-3.68	1.7×10^{-4} e	TTV7	0.88	7.71	54	3.68	[83]
PNDI-TT	660	1.65	-5.59/-3.94	2.89×10^{-5} d	PTB7-Th	0.570	3.56	39.1	0.79	[83]
PNDI-TVT	720	1.58	-5.50/-3.92	4.23×10^{-5} d	PTB7-Th	0.795	7.41	49.9	2.94	[83]
PNDI-TT-TVT	660	1.46	-5.34/-3.88	3.45×10^{-5} d	PTB7-Th	0.790	12.66	48.6	4.86	[84]
P(IDT-NDI)	730	1.94	-5.78/-3.84	5.1×10^{-6} d	PTB7-Th	0.91	7.35	54	3.63	[84]
P(IDT-NDI)	730	1.94	-5.78/-3.84	1.59×10^{-5} d	J51	0.78	9.68	55	4.12	[84]
P(IDT-NDI)	730	1.94	-5.78/-3.84	3.09×10^{-5} d	J51	0.93	9.55	60	5.33	[85]
PNDIBTH	709	2.01	-5.94/-3.93	9.4×10^{-5} d	PBDTT-C-T	0.76	3.77	42	1.20	[85]
PNDIBTOC8	674	2.10	-5.82/-3.72	2.8×10^{-5} d	PBDTT-C-T	0.90	7.65	45	3.14	[86]
PBDTNDI-T	650	1.57	-5.55/-3.98	6.0×10^{-4} e	PBDTBDD-T	0.86	5.62	59	2.88	[87]
P(NDI2HD-T2)	705	-	-	6.18×10^{-5} d	PTB7-Th	0.82	13.97	53	6.11	[87]
P(NDI2OD-T2)	705	-	-	7.97×10^{-5} d	PTB7-Th	0.81	12.36	53	5.30	[87]
P(NDI2DD-T2)	705	-	-	1.21×10^{-4} d	PTB7-Th	0.82	10.48	50	4.31	[88]
P(NDIT-HD)	600	1.85	-5.64/-3.79	8.40×10^{-5} d	PTB7-Th	0.79	13.46	56	5.96	[70]

electrode interfaces, concurrently leading to more efficient charge transfer and hole transport [71]. Li and coworkers showed that all-polymer solar cells comprising a J51:P(NDI2OD-T2) blend demonstrated a high PCE of 8.27 % and a high FF of 70.24 %, along with 75 % EQE at 580 nm, benefiting from the complementary absorptions of the donor and acceptor and appropriate nanoscale-aggregated donor-acceptor interpenetrating networks [72].

Cao and coworkers demonstrated all-polymer solar cells based on PTZBI and P(NDI2OD-T2) using 2-methyl-tetrahydrofuran (2-MeTHF) as the processing solvent. The products displayed a reasonable PCE of 9.16 %, as a result of a homogeneous morphology with finely divided domains [73]. Cao et al. further boosted the efficiency to 10.1 % by using PTZBI-Si with siloxane-functionalized side chains because these improved the solubility of the donor in 2-MeTHF and enhanced the hole mobilities in donor-acceptor blends [74]. Very recently, a benchmark PCE of 11 % was achieved for the PTZBI-Si:P(NDI2OD-T2) blend and this was attributed to the enhanced absorption profile, efficient energy transfer, enhanced charge mobility, and improved morphology from cyclopentyl methyl ether (CPME) that was used as a solvent [38]. Moreover, the all-polymer solar cells processed with CPME exhibited a remarkable PCE of 9.3 %, and the active layer was approximately 350 nm thick, indicating a great promise of this green solvent for high-throughput R2R mass-production.

Wang and coworkers synthesized a series of polymeric acceptors, PNDI-T10, PNDI-T20, and PNDI-T50, by randomly incorporating a single thiophene in place of some bithiophenes in P(NDI2OD-T2). This endowed random polymers with weaker crystallinity and larger achievable molecular weights relative to P(NDI2OD-T2) [75]. PNDI-T10 (with 10 % single thiophene) displayed optimal miscibility with PTB7-Th and the highest PCE of 5.6 %, which was increased to 7.6 % by solvent annealing. Likewise, PNDI-T10 displayed superior performance to P(NDI2OD-T2) and PNDI-T in devices based on PBDTT-FTAZ or PBDTTS-FTAZ [76].

A reasonable PCE of 9.0 % was attained for the all-polymer ternary system (PTB7-Th, PNDI-T10, and PBDTTS-FTAZ), in which PBDTTS-FTAZ served as a sensitizer in the visible region, broadened film

absorption, and generated more free charges by facilitating the coexistence of charge and energy transfer [77]. Jen and coworkers adopted a fluorination strategy to produce P(NDI2OD-2 FT) from the parent P(NDI2OD-T2), which elevated LUMO energy levels, strengthened face-on orientation, and increased crystallinity. The fluorinated acceptor exhibited a PCE of 6.29 %, superior to that of the parent acceptor (5.28 %) with a PBDTT-TT-F donor, whereas a higher PCE of 6.71 % was obtained for P(NDI2DT-2 FT), which possessed longer, 2-decytetradecyl (2DT) side chains [78].

Jenekhe and coworkers reported a series of PDI-(bi)selenophene copolymers, such as PNDIS and PNDIBS [79], that exhibited greater electron mobilities and PCEs than their sulfur analogs because of their improved orbital overlap and enhanced crystallization induced by selenium atoms. PNDIS-HD demonstrated an increase of more than two-fold in PCE (7.73 %) with a PTB7-Th donor, after film-aging at room temperature, compared with that of the thermally annealed devices (3.66 %) [80]. The slower self-organization of polymer/polymer blends during the process of room temperature film-aging resulted in enhanced electron mobility and a more favorable bulk morphology, as observed by photoluminescence (PL) quenching analysis and grazing incidence wide-angle X-ray scattering (GIWAXS).

Analogous to the PDI motif, NDI has also been copolymerized with fused-ring π -linkers, including fluorene, carbazole, TT, TVT, IDT, benzothiadiazole, and BDT, in addition to the (bi)thiophene and (bi)selenophene moieties mentioned above. When blended with a P3HT donor, the fluorene-NDI alternating copolymer PF-NDI showed a PCE of 1.63 % [81], higher than that of the carbazole-conjugated polymer PC-NDI (0.44 %) [82]. A TTV7: PC-NDI blend gave a PCE of 3.68 %, presumably because TTV7 had a more low-lying HOMO level and more complementary absorption with PC-NDI than P3HT [82].

Random copolymer PNDI-TT-TVT exhibited HOMO and LUMO energy levels between those of alternating copolymers (PNDI-TT and PNDI-TVT) and a higher PCE of 4.86 % with PTB7-Th as the donor, which is ascribed to better mixing of the donor and acceptor, and more efficient charge transport [83]. The IDT-NDI alternating copolymer P(IDT-NDI) demonstrated PCEs of 3.63 %, 4.12 %, and 5.33 % when

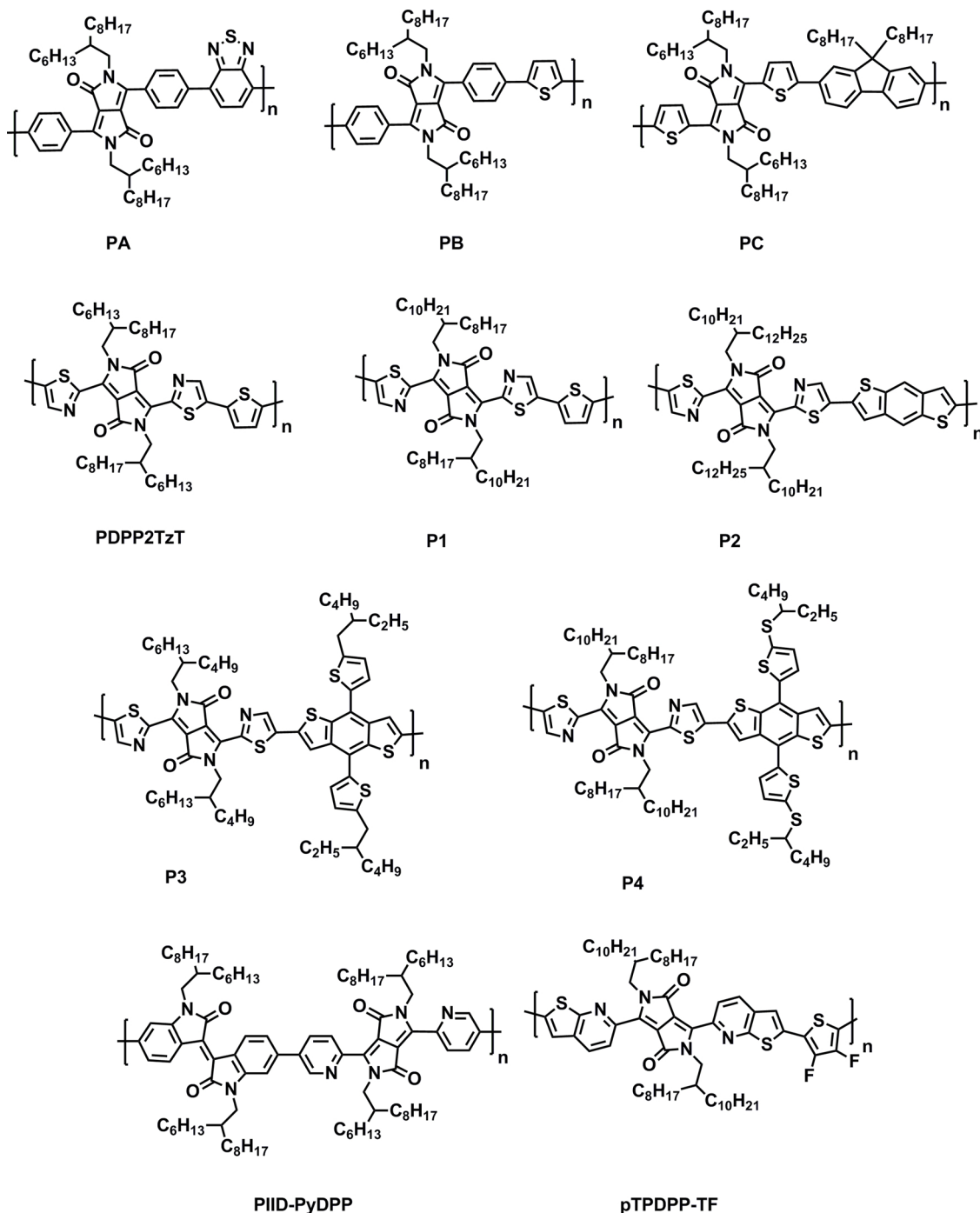


Fig. 6. Chemical structures of selected DPP-based electron-accepting polymers.

combined with the polymer donors PTB7-Th, J50, and J51, respectively [84]. The better performance for J51:P(IDT-NDI) is ascribed to the complementary absorption of donor and acceptor, the relatively low-lying HOMO of J51, and an extensively interpenetrating donor-acceptor network.

Copolymers PNDIBTH and PNDIBTOC8, based on NDI and benzothiadiazole (BT), were designed and investigated in a PBDTTT-C-T-based devices [85]. PNDIBTOC8, with octyloxy chains on the BT moiety, exhibited increased solubility and molecular weight, elevated LUMO levels of -3.72 eV, and the corresponding blend film displayed dendrite-like continuous phase separation, synergistically resulting in the PCE of 3.14 % with a V_{OC} of 0.90 eV, which was much higher than the corresponding values of PNDIBTH (PCE of 1.20 % with V_{OC}

0.76 V). The design of the novel 2D-conjugated polymer acceptor (PBDTNDI-T) was inspired by the extensive use of 2D-conjugated BDT units in donors [86]. PBDTNDI-T presented a suitable LUMO level of -3.98 eV, broad absorption spectra from 300 to 800 nm, and excellent crystalline features. The PBDTNDI-T:PBDBTBD-T blend exhibited a PCE of 2.88 %.

Side-chain engineering provides a facile and effective route to modulate intrachain conformation and interchain interactions and therefore influence the physical and electrical properties of the resulting compound, including solubility, interchain packing, light absorption, and charge mobility. As Kim and coworkers reported, in the series of NDI-2-T based copolymers, P(NDI2HD-T2), with the shortest side chains, showed the strongest crystalline behavior with highly

Table 4

Optoelectronic properties and OSC device parameters for diketopyrrolopyrrole based polymeric acceptors.

Acceptor	λ_{max} (nm)	E_{op} (eV)	HOMO/LUMO (eV)	μ_e ($\text{cm}^2 \text{ V}^{-1} \text{ s}^{-1}$)	Donor	V_{OC} (V)	J_{SC} (mA cm^{-2})	Fill Factor (%)	Highest PCE (%)	Refs.
PA	520	2.05	-5.66/-3.61	3×10^{-11} e	P3HT	0.94	0.68	22	0.14	[89]
PB	545	2.00	-5.58/-3.58	1×10^{-11} e	P3HT	0.90	0.44	27	0.11	[89]
PC	650	1.72	-5.43/-3.71	5×10^{-11} e	P3HT	0.90	1.63	25	0.37	[89]
PDPP2TzT	780	2.63	-5.63/-4.00	1.3×10^{-1} e	PDPP5T	0.81	6.9	51	2.9	[90]
P1	785	1.44	-5.70/-4.26	5.37×10^{-5} d	PTB7-Th	0.71	0.66	29	0.14	[91]
P2	745	1.53	-5.71/-4.18	7.88×10^{-6} d	PTB7-Th	0.95	3.2	36	1.1	[91]
P3	745	1.53	-5.69/-4.16	1.44×10^{-5} d	PTB7-Th	0.99	6.4	37	2.4	[91]
P4	730	1.58	-5.67/-4.09	8.59×10^{-5} d	PTB7-Th	0.94	7.5	45	3.1	[91]
PIID-PyDPP	667	2.21	-6.19/-3.98	4.4×10^{-5} d	PTB7-Th	1.02	6.1	39	2.3	[92]
PIID-PyDPP	667	2.21	-6.19/-3.98	3.7×10^{-5} d	PBDTTS-FTAZ	1.07	9.4	43	4.2	[92]
pTPDPP-TF	711	1.7	-5.8/-4.1	1.0×10^{-1}	PTB7-Th	1.04	6.57	40	2.72	[93]

ordered face-on structures in thin films, resulting in enhanced electron mobilities in OFET and SCLC devices [87]. Consequently, P(NDI2HD-T2)-containing polymers showed much higher PCEs than their counterparts, regardless of donors (PTB7-Th, PTB7, or PPDT2 FBT). This trend was also observed in PNNDIT copolymers: both the degree of crystallinity and the electron mobility were significantly improved with shortened side-chain length, producing PNNDIT-HD-based all-polymer solar cells with PCEs approaching 6 % [88]. It is important to note that the effects of side-chain variation are not generalizable. For instance, P(NDI2DT-FT2) outperformed analogs with shorter side chains in PBDTT-TT-F-based devices, by affording an optimal BHJ morphology with interconnected nanoscale phase separation, thus allowing more efficient exciton dissociation and balanced charge transport [78].

2.4. Diketopyrrolopyrrole polymers

The diketopyrrolopyrrole (DPP) moiety has high structural planarity, a small optical gap, and a high absorption coefficient. DPP-based small molecules and polymers have shown excellent performance as p-type semiconductors, with DPP polymers exhibiting impressive electron

hole mobilities ($> 1 \text{ cm}^2 \text{ V}^{-1} \text{ s}^{-1}$) in OFETs and PCEs above 8 % as donors in OSCs. These properties suggest that DPP-based polymeric acceptors have the potential of high performance and significant utility. Fig. 6 summarizes chemical structures of selected DPP based polymeric acceptors, and their optoelectronic and OPV parameters are summarized in Table 4.

Janssen and coworkers synthesized three DPP-based polymeric acceptors—PA, PB, and PC—and combined them with P3HT in OSCs [89]. These devices exhibited a V_{OC} greater than 0.9 V but extremely low J_{SC} , FF, and PCE because of the low electron mobilities and the inadequate number of long-lived free charge carriers. Janssen and coworkers also used thiophene, thiazole, and DPP moieties to construct PDPP2TzT, which displayed a low-lying HOMO and LUMO, high electron mobility, broad absorption extending to 850 nm [90], and a PCE of 2.9 % with PDPP5T as the donor.

Li and coworkers further designed polymers (P1, P2, P3, and P4) based on a DPP2Tz block with thiophene, BDT, alkylthiophene-BDT, or the alkylthiophene-BDT, respectively, as linkers [91]. Compared with P1, the large aromatic units of P2-4 gave these polymers blue-shifted absorptions and higher LUMOs. P4, with the largest linker

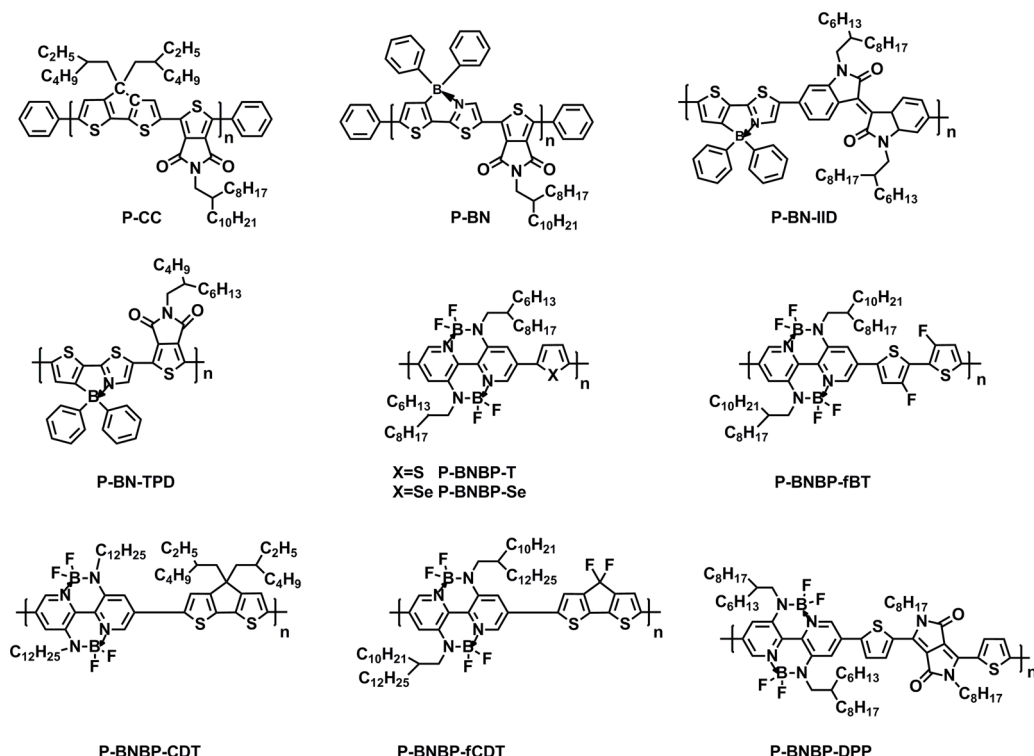


Fig. 7. Chemical structures of selected BN-based electron-accepting polymers.

Table 5

Optoelectronic properties and OSC device parameters for B←—N based polymers polymer acceptors.

Acceptor	λ_{max} (nm)	E_{op} (eV)	HOMO/LUMO (eV)	μ_e ($\text{cm}^2 \text{ V}^{-1} \text{ s}^{-1}$)	Donor	V_{OC} (V)	J_{SC} (mA cm^{-2})	Fill Factor (%)	Highest PCE (%)	Refs.
P-BNBP-T	593	2.27	-5.77/-3.50	6.9×10^{-5} e	PTB7	1.09	7.09	44	3.38	[96]
P-BNBP-T	593	2.27	-5.77/-3.50	7.16×10^{-5} e	PTB7-Th	1.12	5.24	39	2.27	[97]
P-BNBP-Se	600	2.18	-5.84/-3.66	2.07×10^{-4} e	PTB7-Th	1.03	10.02	42	4.26	[97]
P-BNBP-fBT	622	2.25	-5.87/-3.62	2.40×10^{-4} e	PTB7-Th	1.07	12.69	47	6.26	[98]
P-BNBP-CDT	628	2.19	-5.64/-3.45	8.89×10^{-6} d	P3HT	1.01	4.98	35	1.76	[99]
P-BNBP-fCDT	645	2.29	-5.89/-3.60	3.46×10^{-4} e	PTB7-Th	0.99	8.78	44	3.83	[100]
P-BNBP-DPP	761	1.75	-5.32/-3.57	2.14×10^{-4} e	PTB7	0.88	7.54	41	2.69	[101]

(alkylthiophene-BDT) showed the smallest LUMO offset, the lowest energy loss, and the highest PCE (3.1 %) among these acceptors when blended with a PTB7-Th donor.

Wang and coworkers designed PIID-PyDPP, composed of pyridine-flanked DPP and isoindigo units, and blended it with donor PTB7-Th or PBDTS-FTAZ. PBDTS-FTAZ showed a higher PCE of 4.20 % and a higher V_{OC} of 1.07 V because it had a lower HOMO and its absorption spectra were more complementary with that of the acceptor [92]. A planar polymer pTPDPP-TF based on thienopyridine diketopyrrolo-pyrrole and difluorothiophene units, reported by McCulloch and coworkers, displayed a promising n-type charge carrier mobility of $0.1 \text{ cm}^2 \text{ V}^{-1} \text{ s}^{-1}$ in OFETs and a PCE of 2.72 % when blended with the PTB7-Th donor [93].

2.5. B←—N based polymers

The B←—N unit, isoelectronic and isosteric to the C – C unit, is a strong electron-withdrawing unit that has been used to develop electron-transporting materials with low-lying LUMO levels for organic light-emitting diodes (OLEDs). Fig. 7 summarizes chemical structures of selected BN based polymeric acceptors, and their optoelectronic and PV properties are summarized in Table 5. Liu and coworkers observed that replacing a C-C unit with a B←—N unit in conjugated polymers can effectively lower both the LUMO and HOMO energies and disclosed this as a novel strategy to develop polymeric acceptors from typical polymer electron donors. The LUMO and HOMO of polymers that contain the B←—N unit (P-BNs) are lowered by 0.53 and 0.65 eV compared to the

LUMO and HOMO of polymers that contain the C – C unit, thus converting P-BNs from donors to acceptors. A PCE of 0.14 % was displayed by P3HT:P-BN blend films, wherein both fluorescence of P3HT and P-BN was quenched effectively [94].

Compared with P-BN-TPD, P-BN-IID exhibited better π - π stacking, enhanced electron mobility, and improved performance in devices based on PTB7 and PTB7-Th, because the longer IID repeating units alleviated the effect of steric hindrance generated by pendant phenyl groups [95].

B←—N bridged bipyridyl (BNBP) was later revealed as a new class of electron-deficient building block with a fixed planar configuration and low LUMO/HOMO energy levels. P-BNBP-T exhibited high electron mobility, low-lying LUMO and HOMO, and strong absorbance in the visible range and displayed a PCE of 3.38 % with PTB7 [96]. A PTB7-Th:P-BNBP-Se blend showed a higher PCE of 4.26 % than its counterpart with P-BNBP-T (2.27 %), which was presumably attributable to the lower LUMO and higher electron mobility of P-BNBP-Se [97]. The fBT unit was further copolymerized with BNBP to form P-BNBP-fBT because fBT had a planar conformation controlled by the F-S interaction and induced a pseudo-straight polymer backbone configuration. The PTB7-Th:P-BNBP-fBT blend had a PCE of 6.26 % and an energy loss (E_{loss}) of only 0.51 eV [98]. P-BNBP-CDT, composed of alternating BNBP and cyclopentadithiophene, had red-shifted absorption and a high-lying LUMO, in relative to P-BNBP-T, P-BNBP-fBT, and P-BNBP-Se [99]. P3HT:P-BNBP-CDT displayed a PCE of 1.76 %.

Fluorination of P-BNBP-CDT decreased the LUMO energy level, reduced steric hindrance, and improved intermolecular interaction. A

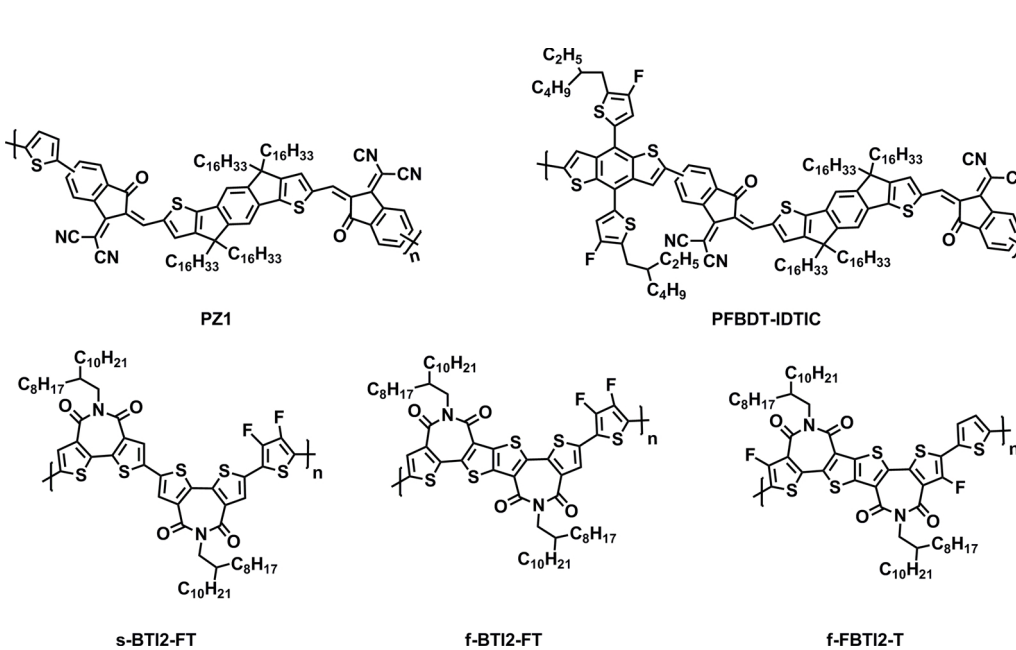


Fig. 8. Chemical structures of other polymeric acceptors featuring new electron-deficient building blocks.

Table 6

Optoelectronic properties and OSC device parameters for other polymeric acceptors.

Acceptor	λ_{max} (nm)	E_{op} (eV)	HOMO/LUMO (eV)	μ_e ($\text{cm}^2 \text{ V}^{-1} \text{ s}^{-1}$)	Donor	V_{OC} (V)	J_{SC} (mA cm^{-2})	Fill Factor (%)	Highest PCE (%)	Refs.
PZ1	705	1.88	-5.74/-3.86	7.02×10^{-5} d	PBDB-T	0.83	16.5	68.99	9.19	[102]
PFBDT-IDTIC	704	1.93	-5.78/-3.85	1.6×10^{-3} e	PM6	0.97	15.39	69	10.3	[103]
s-BTI2-FT	630	1.98	-5.28/-3.30	1.30×10^{-4} d	PTB7-Th	0.971	0.09	35.30	0.03	[106]
f-BTI2-FT	595	1.84	-5.27/-3.43	4.88×10^{-5} d	PTB7-Th	1.04	11.55	57.04	6.85	[106]
f-FBTI2-T	650	2.48	-5.94/-3.46	1.6×10^{-5} d	PTB7-Th	1.05	13.60	56.5	8.1	[107]

PTB7-Th:P-BNBP-fCDT blend had a PCE of 3.83 % [100]. With a small-bandgap DPP moiety in the backbone, P-BNBP-DPP exhibited a broad absorption from 500 to 800 nm, with an optical bandgap of 1.56 eV (much narrower than that of typical BNBP-based polymers), and a PTB7:P-BNBP-DPP blend had a PCE of 2.69 % [101].

2.6. Other polymers

The invention of new electron-deficient building blocks, with excellent solubility, optimized geometry, and electronic properties, offers a new paradigm for the development of polymeric acceptors. Fig. 8 summarizes chemical structures of other polymeric acceptors featuring new electron-deficient building blocks, and their optoelectronic and PV properties are summarized in Table 6.

Inspired by the success of fused-ring electron acceptors, Li and coworkers demonstrated a new strategy to synthesize a indacenodithiophene based polymer acceptor denoted PZ1, by embedding a fused-ring electron acceptor (IDIC-C16) into the main polymeric chain [102]. This new copolymerization strategy meant that PZ1 possessed extended π -conjugation, red-shifted light absorption, and improved thermal stability. All-polymer solar cells based on a PBDBT:PZ1 blend displayed a high PCE of 9.19 %, significantly exceeding that of the IDIC-C16-based device (PCE of 3.96 %). Yan and coworkers designed PFBDT-IDTIC by replacing the thiophene bridge in PZ1 with a 2D-conjugated BDT moiety. PFBDT-IDTIC afforded a high PCE of 10.3 % when blended with PM6, which was attributed to the efficient

absorption (absorption coefficient: $2.74 \times 10^5 \text{ cm}^{-1}$) and high electron mobility of PFBDT-IDTIC [103]. The choice of donor polymer also affected the performance of the resulting PV. By replacing PBDBT with its fluorinated counterpart (PM6), the V_{OC} , J_{SC} , and FF were all improved, with this attributed to the higher HOMO, stronger crystallinity, and higher domain purity of PM6:PFBDT-IDTIC blends.

Bithiophene imide (BTI) is a versatile acceptor unit for high-performance polymers with tunable charge-carrier polarity [104], with the open β -positions of thiophenes in BTI enabling backbone expansion and core modification. When incorporated into organic thin-film transistors (OTFTs), the BTI homopolymer displayed an impressive electron mobility of $0.2 \text{ cm}^2 \text{ V}^{-1} \text{ s}^{-1}$ [105].

Guo and coworkers designed two BTI-based n-type polymers, s-BTI2-FT and f-BTI2-FT, which differed in the linkage between two BTI units. f-BTI2-FT, with a fused BTI dimer, showed a smaller band gap, a lower LUMO, and higher crystallinity than its unfused counterpart [106]. A PTB7-Th:f-BTI2-FT blend had a PCE of 6.85 %, whereas s-BTI2-FT all-PSCs showed very little PV effect. Very recently, the same researchers fluorinated the highly electron-deficient fused BTI dimer and synthesized the resulting polymer f-FBTI2-T [107]. This polymer presented an extended π conjugation, lower-lying LUMO energy level, and a narrower optical bandgap than its desfluoro analog or analog having a fluorinated electron-rich Th donor moiety. Together with a PTB7-Th donor, f-FBTI2-T exhibited a reasonable PCE of 8.1 % and a small E_{loss} of 0.53 eV.

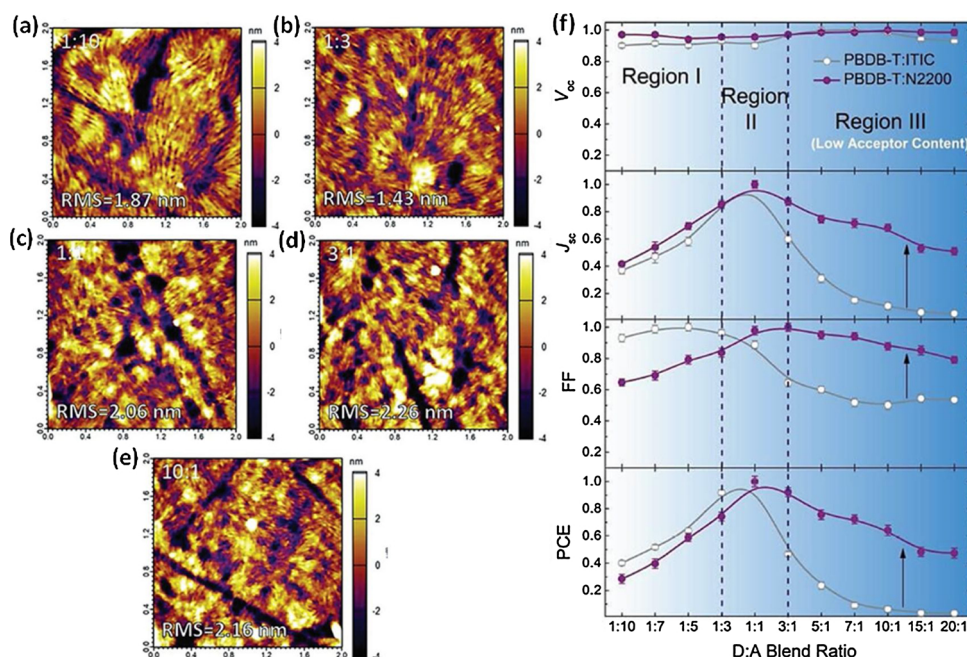


Fig. 9. AFM topography images for PBDB-T:N2200 at D:A blend ratio of (a) 1:10, (b) 1:3, (c) 1:1, (d) 3:1, (e) 10:1 and (f) summary plots of PBDB-T:N2200 (purple) and PBDB-T:ITIC (gray) solar cells performance at different D:A blend ratios.

Reprinted with permission from Ref. [109]. Copyright 2018 Wiley-VCH.

3. Morphology control of all-polymer blend films

It is well known that the PV performance of OSCs strongly depends on the blend morphology of the thin films from which they are fabricated, such as the domain size of the phase-separated structure, degree of crystallinity, and orientation of polymer chains. For solution-processed all-polymer solar cells, the undesired morphologies are those with problematic features such as inhomogeneous internal phase compositions and reduced ordering of the polymer chains in the blend films. In addition, over-sized phase separation always leads to a device with poor PV performance. Therefore, in addition to developing new polymer molecules, control of the morphology of polymer donor(s)/polymer acceptor(s) blend films is critical to enhancement of device performance.

Extensive efforts have been made in the optimization of the active layer morphology in a blend, such as by exploring the effects of donor:acceptor ratios, molecular mass-tuning of donor polymers/acceptor polymers, engineering active-layer processing (e.g., optimizing solvent (s) engineering, addition of solvent additives, coating methods) on improving the performance of devices.

3.1. Polymer Donor/Polymer acceptor blend ratio

Many studies have reported that the donor:acceptor (D:A) relationship plays a critical role in the morphology and PV performance of devices that incorporate fullerene-based OSCs. These findings are also applicable to polymer donor/polymer acceptor solar cells. Ito and coworkers have studied the influence of the D:A ratio on the performance of all-polymer solar cells based on PTQ1/P(NDI2OD-T2) [108]. The one-sun illuminated *J-V* curves of PTQ1/P(NDI2OD-T2) blend all-polymer solar cells confirmed that the PV performance of PTQ1/P(NDI2OD-T2) solar cells strongly depends on the D:A ratio of the blend film. It has been observed that both J_{SC} and FF increased significantly as the donor polymer content increased. When the D:A ratio reached 70:30, an optimized PCE of 4.1 % was achieved. This D:A ratio-dependent PCE of all-polymer solar cells indicates that obtaining the correct D:A ratio is crucial to optimal PV performance in all-polymer solar cells.

Ma and coworkers comprehensively investigated the influence of the D:A blend ratio on the performance of PBDB-T:N2200 all-polymer solar cells and PBDBT:IT-IC polymer-SM solar cells [109]. These researchers systematically changed the D:A ratios from 1:10 to 20:1 to investigate the effect of such a vast change on the device morphology and the consequent performance of devices. Based on the results, they defined three regions of the D:A ratio: Region I (high acceptor content): 1:10 to 1:3; Region II (optimal content): 1:3 to 3:1; and Region III (low acceptor content): 3:1 to 20:1. Impressively, in Region III the PBDB-T:N2200 cell can maintain more than 40 % of the PCE value for a D:A ratio of 20:1, whereas the PCE of a polymer-small molecule (PBDBT:ITIC) cell decreases to almost 0 % at a D:A ratio of approximately 10:1, which is similar to the reported results in polymer-fullerene solar cells [42]. Furthermore, in-depth morphology characterization based on atomic force microscopy (AFM) and 2D grazing-incidence wide-angle X-ray scattering (GIWAXS) have explored the microstructure evolution of blend films as a function of blend ratio.

The AFM images of PBDB-T:N2200 blend films are shown in Fig. 9 to demonstrate the evolution of the surface morphology of blend films as a function of D:A ratio. Given that N2200 is generally found to be a highly crystalline polymer [110,111], the PBDB-T:N2200 blend film with a D:A ratio of 1:10 forms relatively large fibril aggregations with ordered structures. The ordered structure is less distinct but still visible as the proportion of N2200 in the blend decreases, indicating the existence of a well-maintained N2200 network inside the PBDB-T matrix, even with an extremely low acceptor content.

They carried out 2D GIWAXS measurements for PBDB-T: N2200 blends exhibit similar trends in comparison with polymer:SM (PBDB-T:

ITIC) blends. With low donor (1:10) (Region I) or acceptor (10:1) (Region III) content, the diffraction peaks are mainly dominated by the major materials. At more balanced D:A blend ratios (Region II), the (010) peak of the acceptor is less prominent. However, both D and A phases can still show their distinct diffraction peak, indicating appropriate aggregation and fine phase-separation, consistent with the optimal charge transport and PV performance at these ratios. The evolution of scattering patterns as a function of D: A blend ratios is similar in Regions I, II, and III, but the SC performance of PBDB-T:N2200 and PBDB-T:ITIC, although similar in Regions I and II, is distinctly different in Region III as shown in Fig. 9f. This can be understood as showing that the interconnectivity of the SMs is not as good as that of the polymers at low acceptor-content regimes, resulting in limited carrier transport. In short, the effect of D:A blend ratios on device charge-generation and transport is also linked to the surface morphology of blend films.

3.2. Molecular weight tuning

As mentioned above, the morphology of mixed donor/acceptor polymers has a major impact on two of the most important parameters that determine the PV performance of devices: the active layer charge-carrier mobility and the probability of photogenerated charge recombination before collection at the electrodes [112].

It is well known that molecular weight of polymers can significantly affect the blend thin-film morphology, including its aggregation tendencies, phase separation, and backbone orientation [113,114]. We summarize the literature on this aspect, including its effect on the PV performance of all-polymer solar cells.

3.2.1. Molecular weight of polymer donor

Kim et al. used atomic force microscopy (AFM) and resonance soft X-ray scattering (RSoXS) to systematically investigate the effects of the molecular weight of polymer donors on the morphology of the active layer [115]. They synthesized a series of PPDT2 FBT polymer donors with various molecular weights: 12 kDa (PPDT2 FBT_L), 24 kDa (PPDT2 FBT_M), and 40 kDa (PPDT2 FBT_H), with P(NDI2OD-T2) fixed as polymeric acceptor.

It was clearly observed that phase separation in the PPDT2 FBT: P(NDI2OD-T2) blend films depends significantly on the molecular weight of the polymer donor (PPDT2 FBT). The RSoXS results suggest that the domain size of the PPDT2 FBT: P-(NDI2OD-T2) blend films was significantly reduced from 225 nm (PPDT2 FBT_L: P(NDI2OD-T2)) to 115 nm (PPDT2 FBT_H: P(NDI2OD-T2)), which was confirmed by the AFM results (Fig. 10). Clearly, the high-molecular-weight blend film (PPDT2 FBT_H: P(NDI2OD-T2)) had better performance due to its better intermixing, whereas less efficient intermixing led to over-sized aggregated domains and poorer performance in the low-molecular-weight blend film (PPDT2 FBT_L: P(NDI2OD-T2)).

The researchers fabricated the devices by spin-coating from a chloroform solution and correlated the morphology with PV performance of the final all-polymer solar cells. In the high-molecular-weight blend film (PPDT2 FBT_H: P(NDI2OD-T2)), the improved intermixing of PPDT2 FBT_H molecules and P(NDI2OD-T2) molecules led to a reduced domain size and thus an improvement in PV performance of devices. This ranged from a PCE of 3.88 % for the low-molecular-weight blend film (PPDT2 FBT_L: P(NDI2OD-T2)) to a PCE of 5.10 % for the high-molecular-weight blend film (PPDT2 FBT_H: P(NDI2OD-T2)) with *J-V* characteristics shown in Fig. 10e and the corresponding EQE curves shown in Fig. 10f. Concomitant with this was an improvement in J_{SC} and FF values, due to enhancement of exciton dissociation and charge transport abilities.

3.2.2. Molecular weight of polymer acceptor

Veenstra and coworkers used zero-loss energy-filtered TEM (EF-TEM) to investigate the morphology of MDMO-PPV:PCNEPV blend films with various molecular weight (MW) of PCNEPV, namely: low M_w

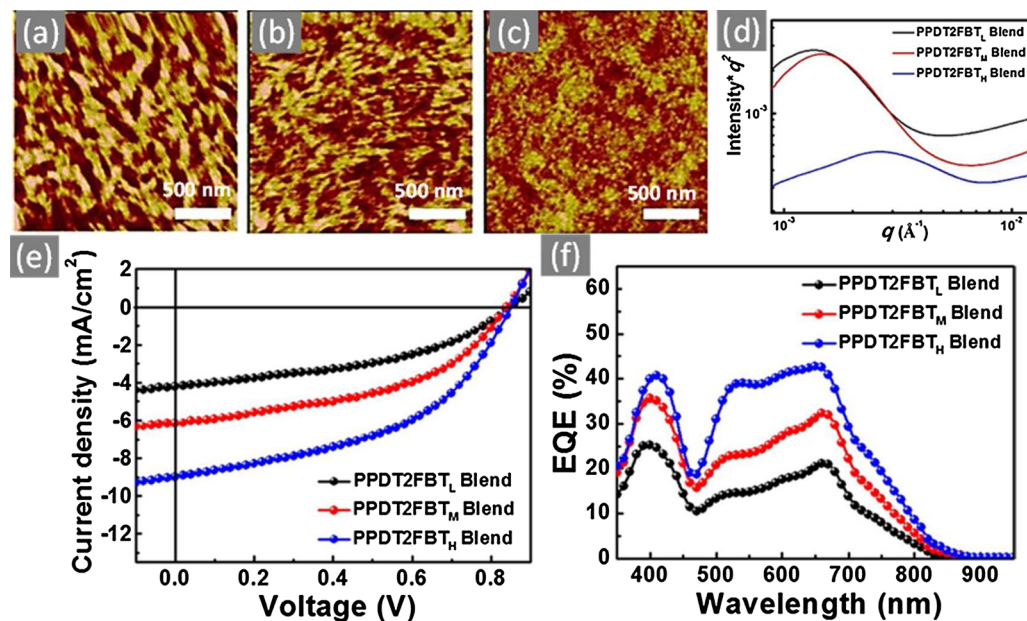


Fig. 10. AFM height images of PPDT2FBT/P(NDI2OD-T2) blend films with (a) low M_w PPDT2FBT, (b) medium M_w PPDT2FBT and (c) high M_w PPDT2FBT. (d) RSoXS profiles of PPDT2FBT: P(NDI2OD-T2) blends as a function of Mn of PPDT2FBT. (e) The J - V characteristics of PPDT2FBT/P(NDI2OD-T2) devices with different M_w of PPDT2FBT and (f) EQE curves of corresponding devices.

Reprinted with permission from Ref. [115]. Copyright 2015 American Chemistry society.

(3.5 kDa), medium M_w (48 kDa), and high M_w (113 kDa), as shown in Fig. 11 [116]. From the nitrogen elemental maps, these workers confirmed that the features shown in Fig. 3 were due to chemical contrast with the dark regions ascribed to PCNEPV-rich domains. It has been noted that for the medium- M_w (48 kDa) case, small (about 20–50 nm) and homogeneously distributed PCNEPV domains were clearly observed in the MDMO-PPV matrix, whereas for the low- M_w (3.5 kDa) case, a homogeneous blend film without distinct phase separation is observed. In contrast, a large-scale phase separation with relatively large PCNEPV domains (domain diameter ca. 200 nm) can be clearly observed in the high- M_w case, as shown in Fig. 11(c). The over-sized domain results in

lower short circuit current evidenced by the IPCE curve as shown in Fig. 11d.

All MDMO-PPV: PCNEPV blend active layers were fabricated with a fixed D:A ratio of 1:1 by weight. However, the PCNEPV domains did not fill 50 % of the images in Fig. 11b, proving the existence of phase-intermixing, and this was confirmed by fluorescence-quenching measurements. Interestingly, the PV performance of devices with blend films with intermixed-phase structures is very similar, which indicates that the PV performance of all-polymer devices is more sensitive to finer-scale intermixing than the effects of over-sized morphological features seen in these EF-TEM images. The IPCE of the corresponding

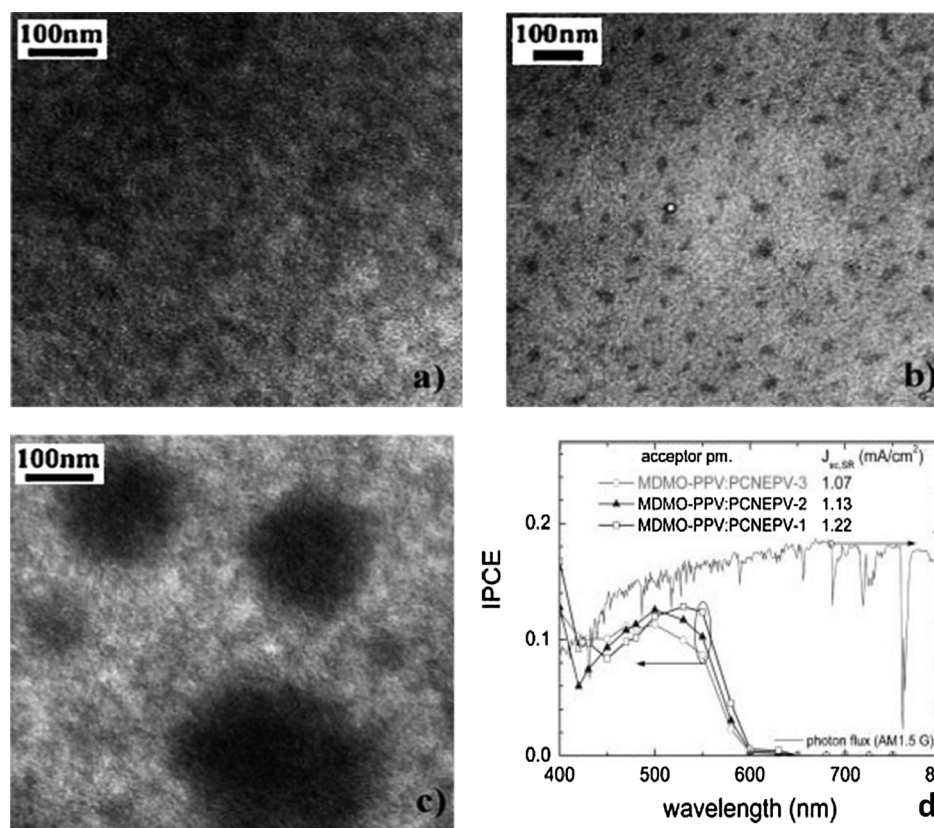


Fig. 11. Zero-loss energy-filtered transmission electron microscopy images of MDMO-PPV: PCNEPV blends: (a) with low M_w PCNEPV, (b) with medium M_w PCNEPV, and (c) with high M_w PCNEPV. (d) EQE spectra of all-polymer blend based photovoltaic devices differing in the molecular weight of the acceptor polymer. The black line with the open squares represents the EQE values obtained on a device with a blend containing the low M_w PCNEPV (PCNEPV-1), dark gray, closed triangles represent the data recorded on a device with the medium M_w PCNEPV (PCNEPV-2), and gray, open circles the EQE obtained with a device prepared with the high M_w PCNEPV (PCNEPV-3). Reprinted with permission from ref [116]. Copyright 2007 Wiley-VCH.

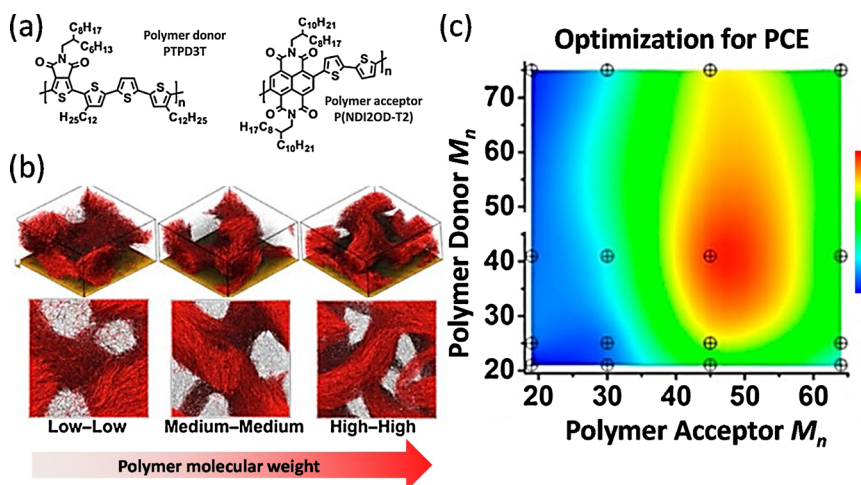


Fig. 12. The effect of molecular weight control for both polymer donor and polymer acceptor in all polymer solar cells. (a) Chemical structures of the polymer donor (PTPD3T) and polymer acceptor (P(NDI2OD-T2)) separately. (b) Coarse-grain modeling of the phase separation process as a function of the component molecular weight. (c) Photovoltaic performance of PTPD3T: P(NDI2OD-T2) polymer solar cells as a function of each component molecular weight.

Reprinted from Ref. [117] with permission. Copyright American Chemical society.

devices are shown in Fig. 11d.

3.2.3. Molecular weight of polymer donor and acceptor

Marks and coworkers studied the influence of M_w on morphological and PV properties by varying the M_w of both polymer donor (PTPD3T) and polymer acceptor (P(NDI2OD-T2)) [117], the chemical structures of which are shown in Fig. 12(a). These workers found that increasing the M_w of both polymer donor and polymer acceptor can gradually transform the morphology of PTPD3T: P(NDI2OD-T2) blend films from being phase-separated to having reduced domain sizes of a more disordered, amorphous nature. With the help of the extended Carothers equations, they offered a straightforward and generalizable method to access the required in-chain donor and acceptor polymers with controllable/predictable M_w . Based on experimental and coarse-grain modeling results, this work revealed that systematic M_w variation significantly influences both intra-chain and inter-chain interactions and consequently the extent of phase separation, the evolution of morphology [Fig. 12(b)], and the PV performance of the devices [Fig. 12(c)].

In accordance with the modeling results, the PCE values were optimized when both PTPD3T and P(NDI2OD-T2) were of an intermediate M_w , which again confirms the importance of M_w in controlling the BHJ morphology and optimizing the PV performance of all-polymer solar cells.

3.3. Active layer processing and engineering

Simple spin-casting of the polymer donor and polymer acceptor blend solution in a single solvent usually yields polymer having poor morphology with undesirable features, such as oversize phase separation, reduced ordering of polymer chains, and decreased phase purity. This directly leads to poor PV performance in all-polymer solar cells. Fortunately, there are several approaches for optimizing the morphology of all-polymer blend films during active layer processing, including solvent(s) engineering, addition of solvent additives, coating methods and post-treatment.

3.3.1. Solvent and additive engineering

For solution-processed all-polymer solar cells, the various boiling points of different solvents can be used to control the solution-drying kinetics and achieve the desired finer phase-separated morphology. Initial studies of all-polymer solar cells demonstrated the importance of solvent selection on the blend film morphology and on device performance. For instance, in 2011, Loi [118] and Sirringhaus [70] independently found that generating P3HT:P(NDI2OD-T2) polymer blends from a single solvent, such as chlorobenzene (CB), dichlorobenzene (DCB), chloroform (CF), or xylene gave products with

PCEs of 0.16 % to 0.18 % due to a hierarchy of phase separation, affording with lateral, impure domains as large as 1 μm. However, when the same P3HT:P(NDI2OD-T2) blend system was processed from a mixed solvent of *p*-xylene and chloronaphthalene, it displayed a remarkably improved PCE of 1.31 %. This was mainly attributed to the enhanced J_{SC} (4.18 mA cm⁻²) resulting from the suppressed self-aggregation of P(NDI2OD-T2) and reduced extent of phase segregation [119].

Ito and coworkers systematically investigated the influence of three processing solvents with different boiling points (b.p.) on the morphology of blend thin films and consequent device performance, using a semicrystalline donor P3HT and an amorphous polymer acceptor PF12TBT [52]. The AFM results revealed remarkable differences in the surface morphology among the three P3HT/PF12TBT blend films, depending on the b.p. of the solvent from which they were processed (Fig. 13).

In some films processed from a high b.p. solvent (DCB, 181 °C), phase-separated structures with oversized domains (a few micrometers) were clearly visible, and other films had phase-separated structures with a reduced lateral dimension size of a few hundred nanometers. In both cases, the size of phase-separated domains was much larger than the L_D value (a few tens of nanometers) of typical conjugated polymers. In contrast, a well-mixed, homogeneous P3HT/PF12TBT blend film was obtained with no distinct phase-separated structure when fabricated from low b.p. solvent (CF, 61 °C), and this blend possessed the highest J_{SC} value of the three samples, as shown in Fig. 13d. These findings demonstrate that minimizing phase separation during the casting step is an effective means by which polymer film morphology can be optimized, to afford a final product with an enhanced J_{SC} for use in all-polymer solar cells.

Processing strategies that use solvent additives are also known to be beneficial for optimizing the formation of blend nanostructures correlated with improved PV performance for polymer/fullerene blend solar cells [121], and this positive effect of solvent additives on the device performance has also been discovered to apply in the fabrication of polymer blends for all-polymer solar cells. Friend and coworkers systematically examined the effect of additives on the efficiency of polymer/polymer blend solar cells based on P3HT donor polymers and a range of acceptor polymers and demonstrated that 4-bromoanisole (BrAni) is an effective solvent additive for the promotion of P3HT crystallization and increased hole mobility in P3HT-containing blends [122]. The addition of BrAni (2–14 vol%) increased the EQE to more than 10 % for both P3HT/F8TBT and P3HT/PCDTBT blend solar cells prepared from CB solution. These researchers further revealed that a combination of a solvent additive and post-thermal annealing yields greater improvement in the EQE and J_{SC} than additive processing alone.

Neher and coworkers investigated the influence of

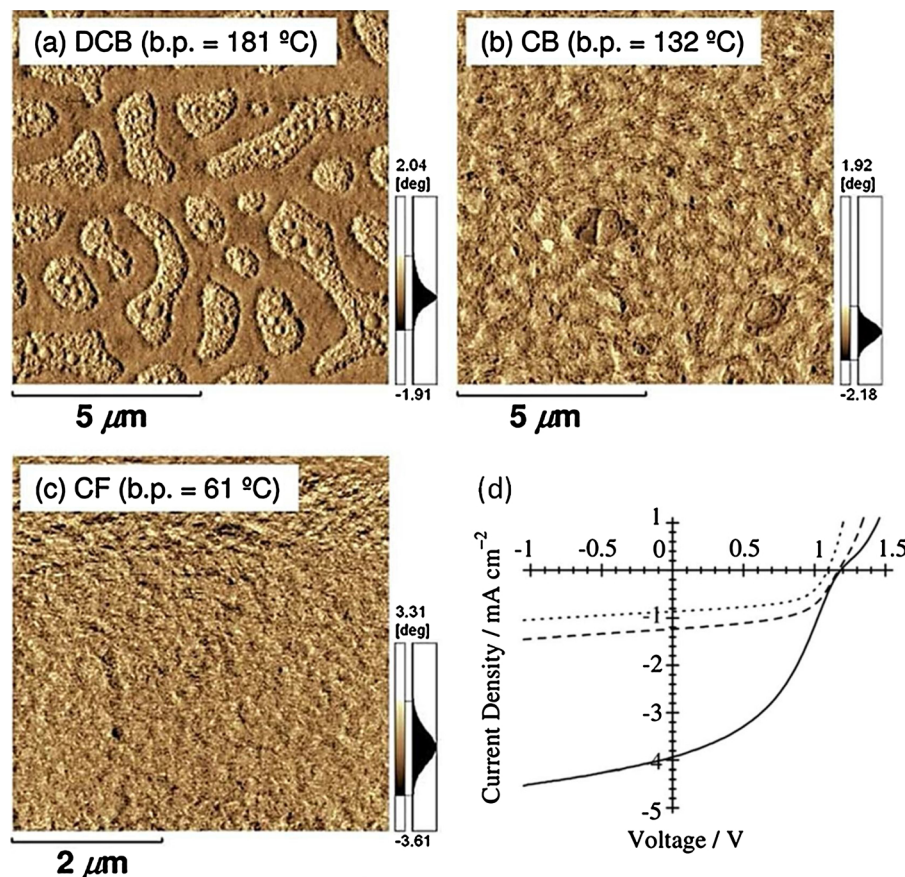


Fig. 13. AFM phase images of P3HT/PF12TBT (1:1 by weight) blend films fabricated by spin coating from (a) DCB (b) CB, and (c) CF solution on glass substrates and annealed at 140 °C for 10 min. *J–V* characteristics of corresponding P3HT/PF12TBT solar cells under AM 1.5 G 100 mW/cm² illuminations (DCB: dotted line, CB: dashed line, and CF: solid line).

Reprinted from Ref. [120] with permission. Copyright Royal Chemical society.

chloronaphthalene (CN) as a solvent additive on the nanomorphology of all-polymer blend films. Scanning near-field optical microscopy (SNOM) measurements have been performed to study the nanomorphology change concomitant with the addition of solvent additives. This demonstrated that the addition of CN to a *p*-xylene solution suppressed the pre-aggregation of P(NDI2OD-T2) in the solution and that P3HT/P(NDI2OD-T2) blend solar cells prepared from a *p*-xylene:CN (50:50) mixed solvent exhibited a large increase in J_{SC} and PCE as shown in Fig. 14b. This was due to the finer mixing of polymer molecules with a less phase-separated structure in the blend film (Fig. 14), compared with reference devices obtained from pure *p*-xylene.

3.3.2. Coating engineering

Many efforts have been made to improve polymer crystallinity and thus device performance. Paradoxically, increasing the polymer crystallinity can sometimes decrease device performance if the domain size of phase-separated structures increases at the same time. In particular, for all-polymer solar cells, it is undesirable for the domain size to increase much beyond the exciton diffusion length because it leads to a higher recombination rate.

In contrast to the traditional blade-coating of all-polymer solar cells [123,124], Bao and coworkers introduced a novel method to direct micro-phase separation, especially of polymer molecule-crystallization, by using micro-structured printing blades to manipulate the fluid flow during active-layer solution printing [Fig. 15(a)] [125]. This approach (FLUENCE) enables them to enhance the polymer crystallinity without increasing the domain size by a mechanism involving flow-induced nucleation.

Bao et al. found that the domain size was characterized by resonant soft X-ray scattering (RSoXS), with the domain size of the FLUENCE-printed blend films and the reference films examined, to confirm how the flow design influences the phase separation behavior. In addition,

polarized light was used for a local molecular orientation study [Fig. 15(c)]. At low printing speeds, the application of FLUENCE significantly enhanced the scattering anisotropy when comparing the scattering profiles perpendicular and parallel to the beam polarization direction [Fig. 15(d)]. Such anisotropy is insensitive to the rotation of in-plane direction, which indicates that the polymer chains have local correlation in their orientation alignment (over tens of nanometers) but are globally isotropic.

In the reference films, two characteristic length scales can be noticed: one isotropic (at low q) and the other anisotropic (at high q). In contrast, the FLUENCE-printed samples exhibited one dominant length scale, with a broader distribution and anisotropic scattering profile over the investigated q range. Meanwhile, the dominant scattering feature shifted to higher q . At high printing speeds, the isotropic-scattering features decreased in the reference films, and the impact of FLUENCE became less obvious, other than modestly shifting the scattering feature to higher q [Fig. 15(e)]. To better illustrate this, Fig. 15(f) shows a simplified schematic illustrating the possible in-plane morphologies. The red domain is electron donor PII-tT-PS5, forming amorphous (shown without red bars) and semicrystalline domains (with red bars). The blue domain represents the amorphous electron-acceptor polymer P(TP). The semicrystalline domains are not crystallites but are likely aggregates of crystallites, possibly separated by small amorphous regions.

This coating approach combines the advantages of meniscus-guided coating techniques with the unique characteristics of flow and is therefore a distinct film-casting method for morphology control in the fabrication of all-polymer solar cells.

3.3.3. Post-treatment

3.3.3.1. Thermal annealing. As a well-known post-treatment, thermal annealing has also been successfully applied for all-polymer solar cells.

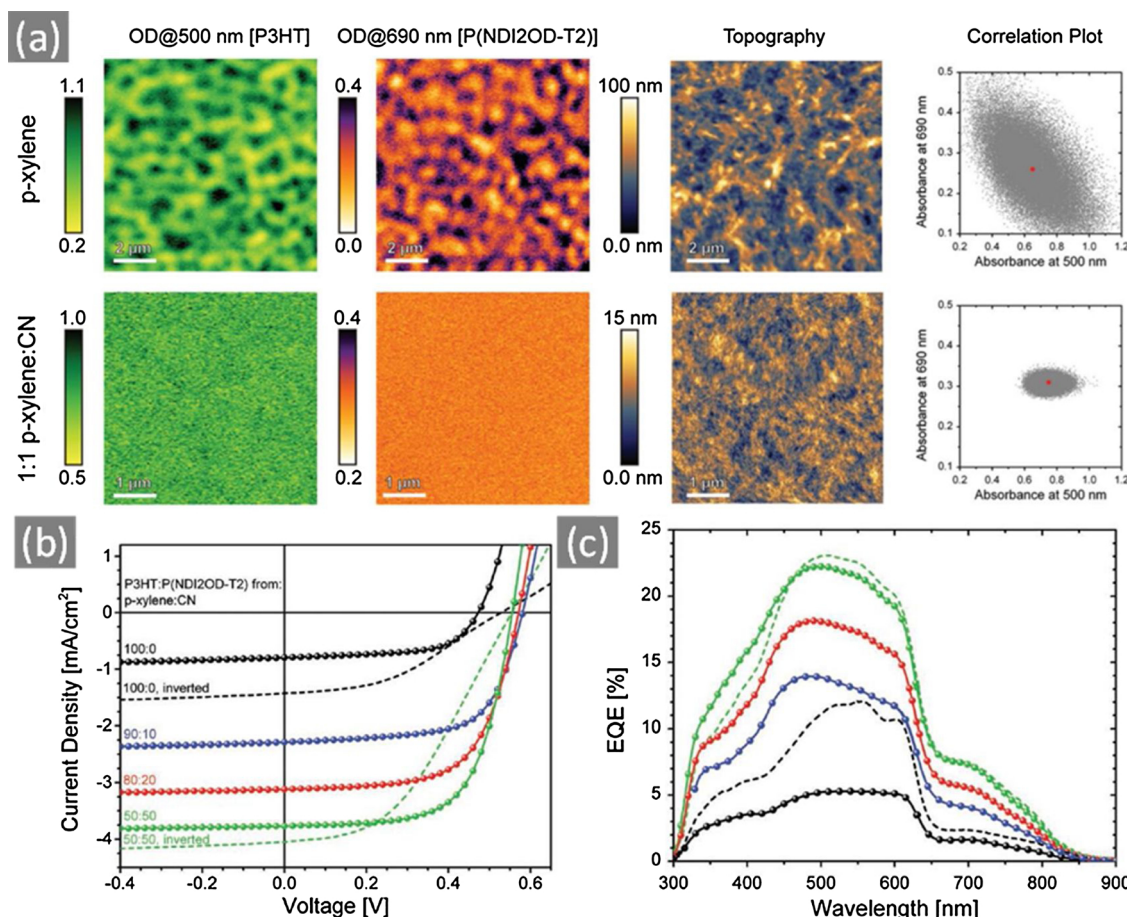


Fig. 14. (a) SNOM images of the blends of the solar cells from Fig. 5 fabricated from *p*-xylene (top) and 1:1 *p*-xylene:CN (bottom), taken at 500 and 690 nm. The scale bar is expressed in optical density OD, defined as $OD = -\log_{10}(I/I_0)$, where I_0 is the incident and I the transmitted photon flux. AFM height images are obtained by independent measurements with a Si-cantilever. Red dots in the correlation plots represent average OD values at the respective wavelength obtained by averaging over the whole SNOM image. (b) J - V characteristics under simulated AM 1.5 illumination and (c) EQE spectra of P3HT: P(NDI2OD-T2) (1:0.75) BHJ solar cells spin-coated from solvent mixtures of *p*-xylene and CN. The mixing ratios of *p*-xylene: CN are 100:0 (black), 90:10 (blue), 80:20 (red), and 50:50 (green); and the active layer thickness is 200 nm, 300 nm, 310 nm, and 275 nm, respectively.

Reprinted from Ref. [122] with permission. Copyright Royal Chemical society.

Moore and coworkers have used scanning transmission X-ray microscopy (STXM) to investigate the effect of thermal annealing on P3HT:P(NDI2OD-T2) blend film morphology [70]. (Fig. 16). In contrast to the traditional tools for polymer blend film-morphology characterization, such as AFM and TEM, STXM is particularly well-suited to characterize the morphology of polymer/polymer blends films due to the strong chemical contrast afforded by soft X-rays [126].

The X-ray absorption spectrum of pure P3HT differs significantly from that of neat P(NDI2ODT2), with a distinct absorption at around 285 eV, corresponding to the $1s$ to π^* transition. Based on the X-ray absorption spectra of the two neat films, optimal contrast is provided by imaging at the energy of 285 eV, where absorption is strongly dominated by P3HT molecules. The scale bar is expressed in X-ray optical density, which is defined as $OD = \log(I_0/I)$, where I_0 is the incident and I is the transmitted photon flux. Bright regions in these images correspond to regions rich in P3HT. Because these images are acquired in transmission mode, the domains represent an average throughout the film thickness, which is different from the surface topography of the films as characterized by AFM, and has confirmed the suitability of STXM for revealing information about bulk phase-separation of polymer-polymer blends.

Fig. 16 presents STXM images of the P3HT: P(NDI2OD-T2) system for 1:1 (by weight) blends prepared from different solvents (CF, xylene, DB), before and after annealing. Domains can be clearly observed via STXM for all casting solvents. CF-processed blends were found to have

the highest J_{SC} (Fig. 16g) and best PCE (Fig. 16h) and to exhibit the finest domain structure, with characteristic domain size of around 200 nm, as characterized by STXM. A much coarser domain structure is observed in the DB- and xylene-processed blends, with domains of 500–1000 nm. After post-treatment thermal annealing (130 °C for 10 min), subtly refined morphology can be observed in all three samples. The enhanced kinetics for each component in the blend films facilitate the packing of corresponding domains, yielding an improved contrast in STXM images, corresponding with slightly refined morphology.

3.3.3.2. Solvent vapor annealing. Solvent vapor annealing (SVA), a widely used post-treatment method, was initiated by Gang Li and coworkers [127]. SVA can effectively improve the packing of polymer chains in fullerene-based OSCs and has now been successfully used in all-polymer solar cell fabrication. Using a PTB7-Th/PNDI-T10 system, Li and coworkers demonstrated the effects of SVA on the morphology and thus the PV performance of devices [128]. The AFM data show that the as-cast PTB7-Th:PNDI-T10 blend film presents a relative finer microstructure and continuous phase-segregated morphology, with a low roughness of 1.01 nm. After SVA, the PTB7-Th:PNDI-T10 blend film has a minimal roughness of 0.76 nm, directly indicating SVA does change the surface of the blend. From the GIWAS patterns, it has been noticed that only weak (001) and (200) peaks can be observed in the PTB7-Th:PNDI-T10 blend film due to the suppressed crystallization for

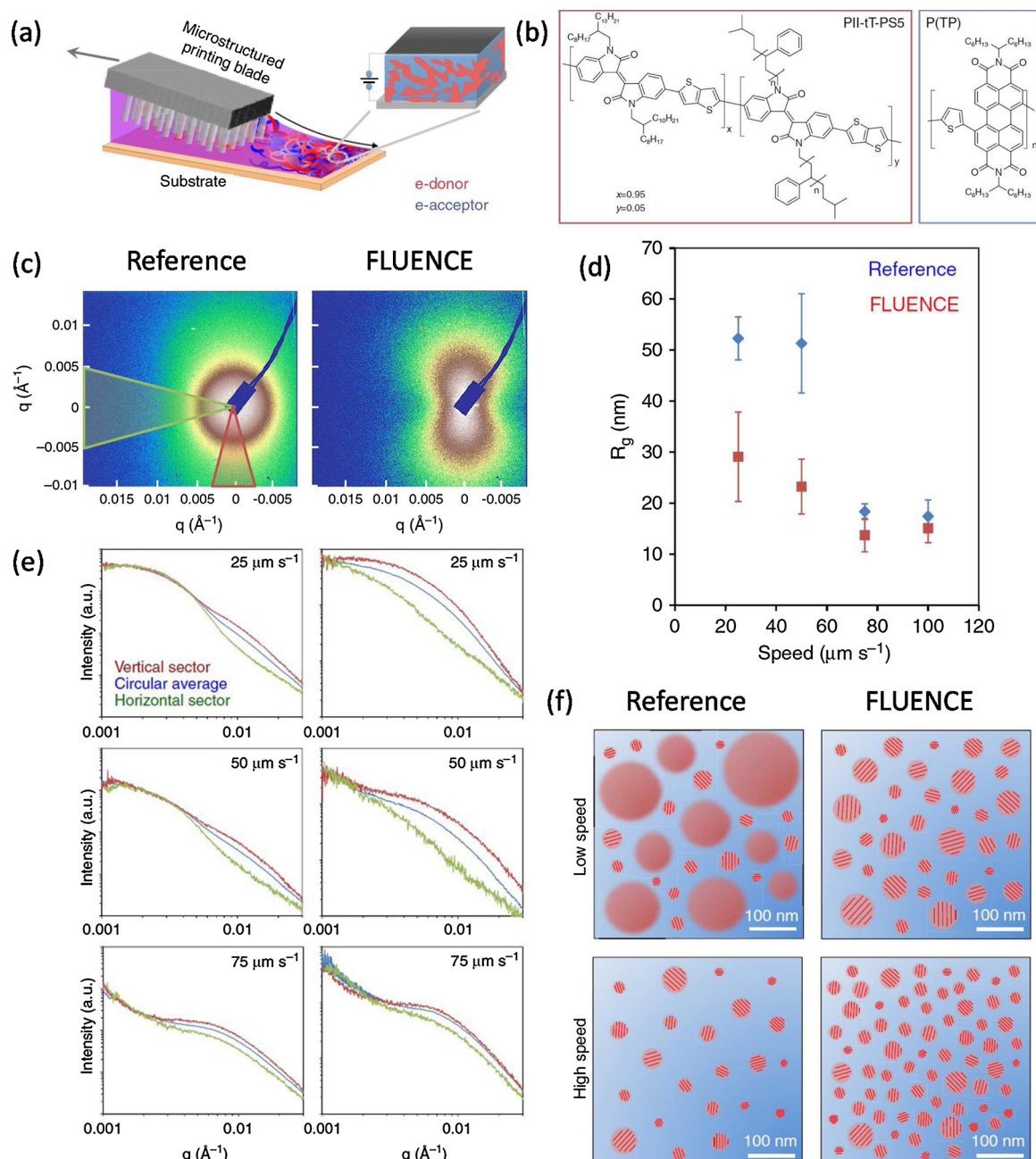


Fig. 15. (a) Schematic of the FLUENCE method implemented on the solution shearing platform. (b) Chemical structure of electron-donor polymer (PII-tT-PS5) and electron-acceptor polymer (P(TP)) used in the work. (c) Two-dimensional scattering images of reference versus FLUENCE films prepared at the speed of 25 mm/s. (d) Radius of gyration (R_g) from Guinier analysis assuming spherical domains. R_g is calculated by fitting the scattering data with $I(q) = I_0 \exp(-q^2 R_g^2 / 3)$. (e) Integrated intensity profiles of reference versus FLUENCE films prepared at different printing speeds. (f) Simplified schematic illustrating the possible in-plane morphology. Reprinted with permission from Ref. [125]. Copyright 2015 Nature publishing.

each component in the blend film caused by increased backbone disorder. SVA has the opposite effect and thus enhances crystallization.

To quantitatively compare the $\pi-\pi$ stacking characteristics after SVA treatment, the (010) coherence length (CL) was calculated using the Scherrer equation, based on the (010) scattering peak measured by GIWAXS. The calculated results demonstrated that solvent annealing has increased the CL value from 1.90 to 2.05 nm in the PTB7-Th: PNDI-T10 blends and that these changes in (010) CL are in a good agreement with the mobility results by observed by SCLC. The improved charge-carrier transport in the blend film further suppresses the bimolecular recombination, leading to a high PCE of 7.6 % for PTB7-Th: PNDI-T10 all-polymer solar cells.

4. Electron transport properties in all-polymer solar cells

In this section, the electron transport properties of BHJ films are reviewed with a focus on the all-polymer BHJs. Studies of hole transport are abundant and can be found in the literatures [129,130]. In BHJ films, acceptor materials usually transport electrons. The electron mobility μ , which is defined by the equation $v_d = \mu F$, where F is the external electric field applied to BHJs, and v_d is the electron drift velocity caused by the electric field, is a widely-used parameter to describe the ability of electron transport in solid-state films. Fig. 17 summarizes the zero-field electron mobilities and efficiencies of all-polymer solar cells with the n-type polymeric acceptors BT, PDI, NDI, DPP and BN discussed in Section 2. Besides having desirable electron mobility values in

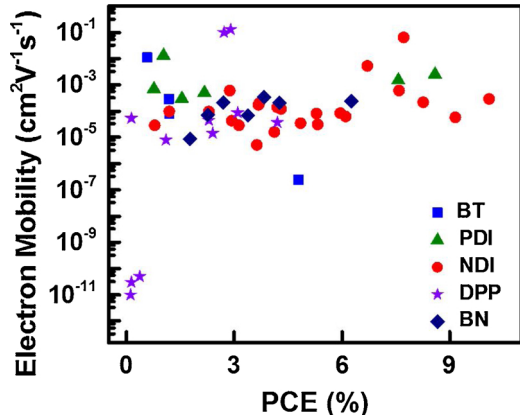
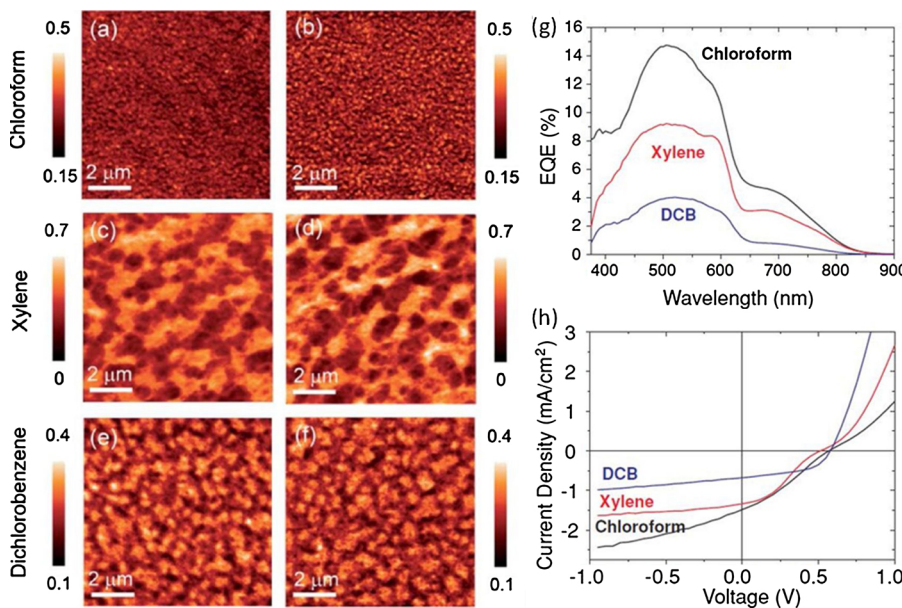


Fig. 17. Electron mobilities and PCEs of selected all-polymer BHJ solar cells involving BT, PDI, NDI, DPP, and BN based polymeric acceptors.

the range of 10^{-5} – 10^{-3} $\text{cm}^2 \text{V}^{-1} \text{s}^{-1}$, all-polymer BHJs enjoy several strengths over other fullerene or small molecular acceptor-based BHJs. The features include:

- (1) less dependence of mobilities on temperature (smaller energetic disorder) and electric field (suppressed Poole-Frenkel effect);
- (2) composition tolerance;
- (3) better immunity to moisture and external tempering;
- (4) compatibility for printing technologies and thick film fabrication.

All these factors converge to improve the overall stability and device reproducibility of all-polymer OPV cells. Below, we will examine how (1)–(4) arise by considering (i) factors affecting electron mobilities and defect states, and (ii) the interaction between donor materials / polymeric electron acceptors and the electron percolation pathways in BHJs.

4.1. Electron transport in polymeric acceptors

From the perspective of the electron-accepting moiety topology, three different classes of acceptors are widely used in the BHJ solar cells: (1) fullerene-based acceptors, such as PCBM, PC_{71}BM , and ICBA; (2) non-fullerene (NF) SMAs such as ITIC, IT-4 F, and PDI-based SMAs;

(3) polymer acceptors such as N2200 [131–139]. These three classes of acceptors possess acceptor moieties with different shapes. Fig. 18 shows selected examples of these acceptors. For the fullerenes, they resemble nano-spheres. The SMAs are much more complicated but their acceptor moieties tend to have flat plates-like geometries. For the polymeric acceptors (e.g. N2200), they can be treated as long conducting wires. Electrons can transport across various D:A-blended BHJ films by different mechanisms, and OPV devices that incorporate these films exhibit different electron transport properties [140–143]. For fullerene-based acceptors, they are known to possess high electron mobilities. As a result, they are widely in BHJ cells despite drawbacks in environmental stability (e.g. heat/oxygen/moisture) and device lifetime [144–147]. Electron mobilities in fullerene-based BHJs are usually in the range of 10^{-4} – 10^{-3} $\text{cm}^2 \text{V}^{-1} \text{s}^{-1}$, which is significantly larger than those in NF SMA-based films [148]. Usually, fullerene-based BHJ solar cells have highly electric field-dependent electron mobilities, which is unfavorable for the fabrication of high-performance thick-film devices [149,150]. In fullerene BHJs, alkyl groups are usually linked to the sterically hindered D units of the polymer molecules. This means that the electron-accepting A units must have sterically unhindered regions to be able to contact the fullerene-based acceptors [151]. Graham et al. demonstrated how donor polymer molecules interact with fullerene-based acceptors [152], using the solid-state two-dimensional ^{13}C heteronuclear correlation nuclear magnetic resonance (NMR) technique to give direct evidence for the acceptor moiety – fullerene connecting model of the donor polymer PBTTTPD and the fullerene-acceptor PCBM. Currently, ITIC derivatives, and acceptors with NDI or PDI moieties are the most widely-used NF SMAs [153–156]. The push-pull effect is the leading cause for the electron transport in ITIC derivatives [157,158]. As the electron-pushing center is shielded by the bulky side chains, bi-molecular packing occurs between the electron-pulling units. Polymer:ITIC-derivative BHJs thus usually exhibit relatively low electron mobilities compared to those seen in fullerene-based acceptors in the range of 10^{-4} – 10^{-3} $\text{cm}^2 \text{V}^{-2} \text{s}^{-1}$.

Researchers have yet developed a widely accepted and applicable transport model to describe the dynamics of electron carriers in n-type organic semiconductors. The consensus is that the electron transport mechanism in n-type polymeric acceptors involves the mobilization of electrons mainly by thermally assisted tunneling via highly localized states [159,160]. Electron transport properties can be affected by many factors, such as the carrier density n , temperature T , and applied electric field F [161,162]. Compared with their SMA-based counterparts,

Acceptor Type	Polymer Acceptors	NF Small Molecules	Fullerene-based Acceptors
Geometry	Prolates	Oblate Spheroids	Spheres
Modeling Equation	$\sigma \cong \sigma_0 \exp \left[-\frac{2D}{\xi} \frac{\gamma(b/a)^2}{\phi} \right]$	$\sigma \cong \sigma_0 \exp \left[-\frac{2D}{\xi} \left[\frac{0.15(a/b)}{\phi} \right]^{4/3} \right]$	$\sigma \cong \sigma_0 \exp \left[-\frac{2D}{\xi} \frac{1.65(a/b)^3}{12\phi(2-\phi)} \right]$
Chemical Structure	<p>N2200 <chem>*C1=C(C=C2=C1C(=O)N(C(*)C(*)*)C(=O)N2C(*)C(*)*)C=C3=C2S=C1=C3</chem></p> <p>PDI-2T <chem>*C1=C(C=C2=C1C(=O)N(C(*)C(*)*)C(=O)N2C(*)C(*)*)C=C3=C2S=C1=C3</chem></p>	<p>ITIC <chem>*C1=C(C=C2=C1C(=O)N(C(*)C(*)*)C(=O)N2C(*)C(*)*)C=C3=C2S=C1=C3</chem></p> <p>IT-M <chem>*C1=C(C=C2=C1C(F)(F)C(=O)N(C(*)C(*)*)C(=O)N2C(*)C(*)*)C=C3=C2S=C1=C3</chem></p> <p>ITIC-Th <chem>*C1=C(C=C2=C1C(F)(F)C(=O)N(C(*)C(*)*)C(=O)N2C(*)C(*)*)C=C3=C2S=C1=C3</chem></p> <p>IEICO-4F <chem>*C1=C(C=C2=C1C(F)(F)C(=O)N(C(*)C(*)*)C(=O)N2C(*)C(*)*)C=C3=C2S=C1=C3</chem></p>	<p>PC₇₁BM <chem>*C1=C(C=C2=C1C(F)(F)C(=O)N(C(*)C(*)*)C(=O)N2C(*)C(*)*)C=C3=C2S=C1=C3</chem></p> <p>PCBM <chem>*C1=C(C=C2=C1C(F)(F)C(=O)N(C(*)C(*)*)C(=O)N2C(*)C(*)*)C=C3=C2S=C1=C3</chem></p> <p>ICBA <chem>*C1=C(C=C2=C1C(F)(F)C(=O)N(C(*)C(*)*)C(=O)N2C(*)C(*)*)C=C3=C2S=C1=C3</chem></p>

Fig. 18. Selected examples of electron acceptors possessing acceptor moieties with different shapes, involving polymers (prolates) N2200 and PDI-2T; non-fullerene small molecules (oblate spheroids) ITIC, ITIC-Th, IT-M and IEICO-4F; and fullerene-based (spheres) PC₇₁BM, PCBM, and ICBA. Three model equations describing percolation conditions of conductive/insulating phases are adapted from Eq. (7).

all-polymer BHJs have unique and excellent electron transport properties, involving less temperature-dependent mobilities, a suppressed Poole-Frenkel effect, and polymer acceptors also tend to dominate the electron transport in bi-acceptor ternary BHJs. Meanwhile, steric hindrance and solubility are also important factors that affect the efficiency of electron transport in all-polymer BHJs.

In organic semiconducting polymers, the electron transport are usually inferior to the hole transport, due to the subgap electron trap states introduced by extrinsic defect sites [163]. Nicolai et al. evaluated the electron transport properties of a series of semiconducting polymers (Fig. 19) Their results indicate that the electron transport is limited by energetic traps located in the bandgap which show a Gaussian energy distribution, with a typical distribution width of ~0.1 eV. The hydrated oxygen complexes are the most suspected of the electron traps. The OC₁C₁₀-PPV device exhibits a double logarithmic *J-V* slope of ~6.5, whereas the PCPDTBT device shows a slope close to 3. It is generally accepted that such slopes are related to the trap positions and distributions in the bandgap. Polymers with deeper LUMO levels show

weaker voltage dependence of the electron currents.

Blakesley et al. simplified the charge transporting model in conjugated polymers with the electron energetic disorder, which is expressed as [164]

$$\mu(T, F, n) = \mu_0(T) g_1(F, T) g_2(n, T) \quad (1)$$

where $\mu_0(T)$ is defined as the low-field/low-carrier-density mobility at a certain temperature, g_1 and g_2 are the dimensionless mobility enhancement factors for F and n , respectively. Fig. 20 plots the best-fit curves of the poly(9,9-diptylfluorene-co-benzothiadiazole) (F8BT) devices of various film thicknesses. At room temperature, the effect of F (factor g_1) is more significant than the effect of n (factor g_2).

In all-polymer BHJs, a special property of carrier transport is that electrons may migrate in the intrachain pathway within an n-type polymer, in contrast to the well-established inter-molecular hopping model for electron transport in fullerene-based and NF SMA-based BHJs. On the other hand, hole-carriers have previously been studied mainly in conjugated polymeric molecules [165,166]. Grévin and

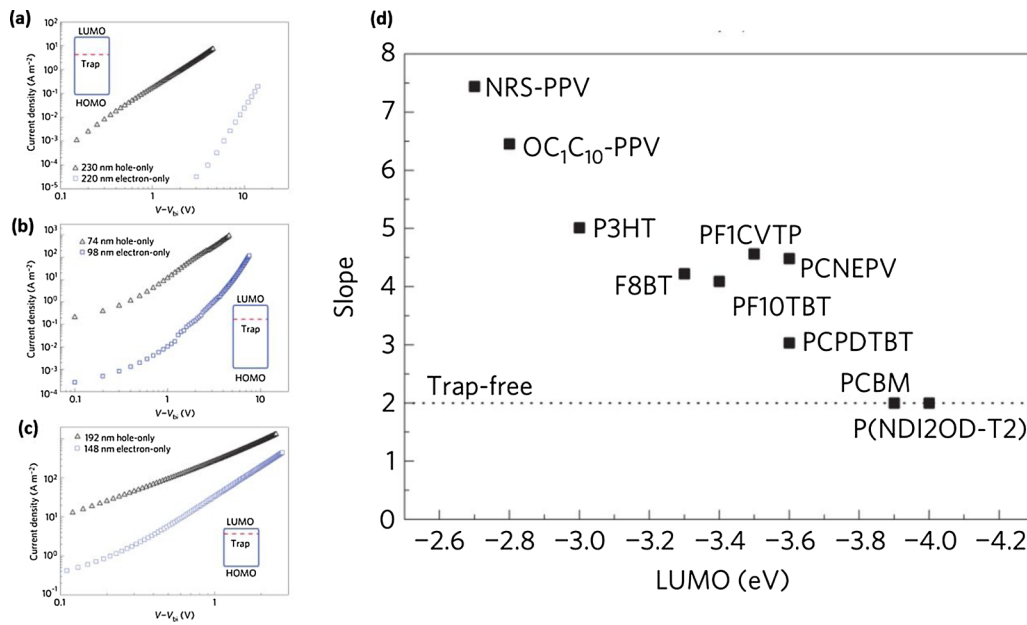


Fig. 19. Comparison of electron and hole current of (a) OC₁C₁₀-PPV; (b) F8BT, and (c) PCPDTBT; Electron transport in different polymers; and (d) the slope of the electron-only *J-V* curves on a double-logarithmic scale. The value of the slope was determined by fitting the experimental *J-V* curve with a power law. The dotted lines are fits to a power law. The dotted line indicates a slope of 2 as observed for trap-free space-charge-limited currents. Reprinted with permission from Ref. [163]. Copyright 2012 Nature Publishing Group.

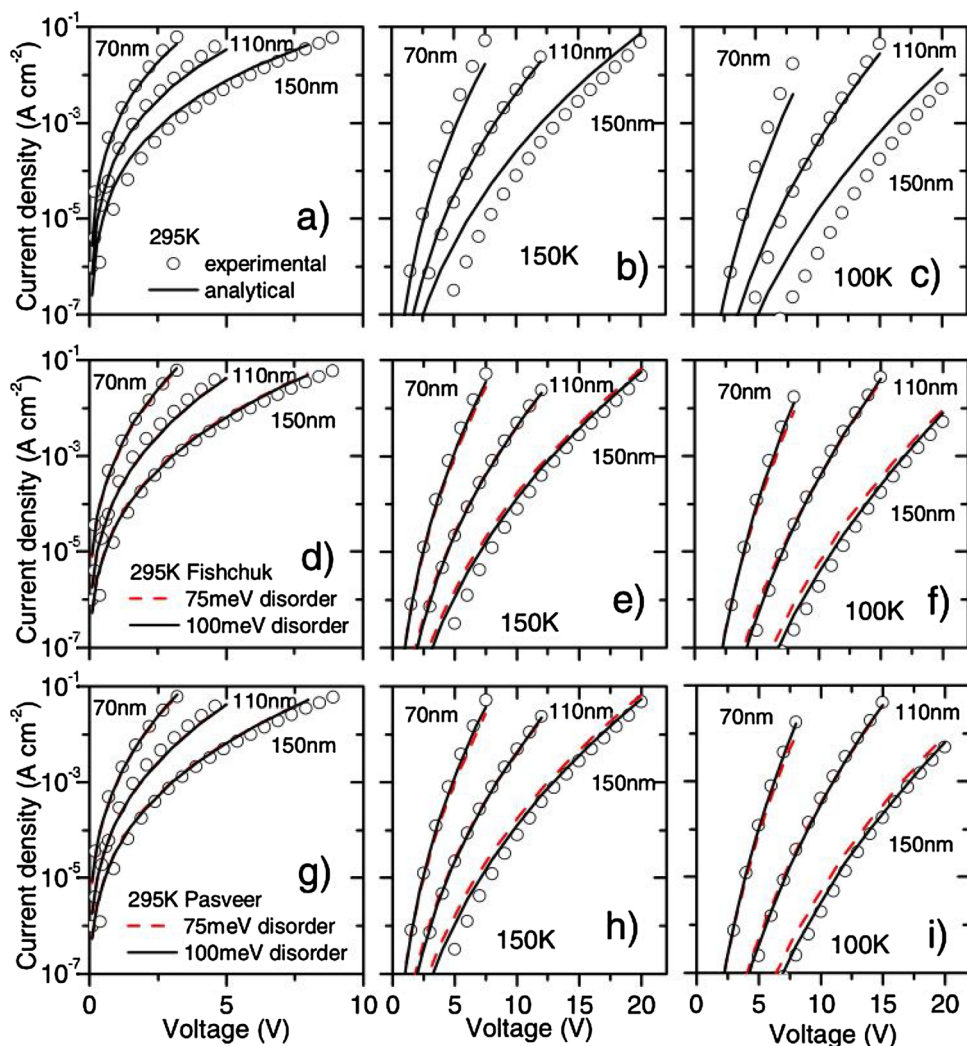


Fig. 20. Best-fit curves of P8BT devices with different film thicknesses. (a–c) fitted with analytical model; (d–f) fitted by numerical simulation using Fishchuk concentration-dependent mobility; and (g–i) numerical simulation with Pasveer concentration dependence. (a), (d), and (g) at 295 K, (b), (e), and (h) at 150 K, and (c), (f), and (i) at 100 K.

Reprinted with permission from Ref. [164]. Copyright 2010 American Physical Society.

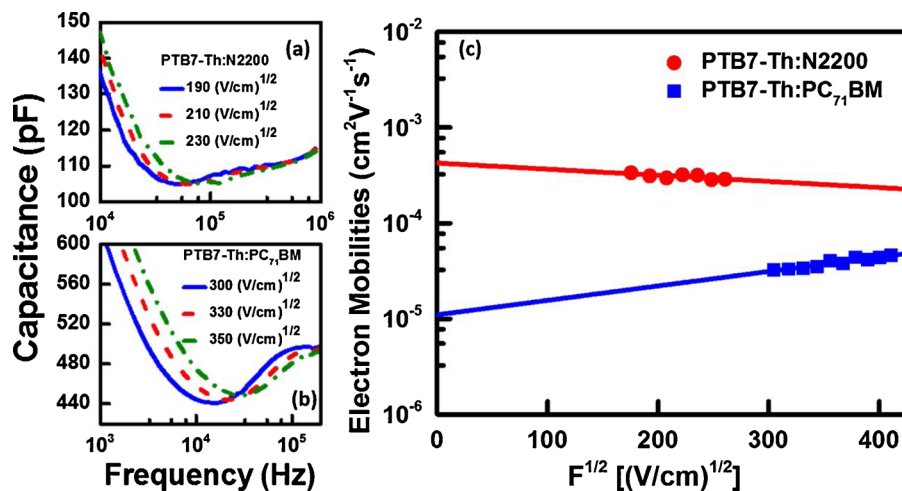


Fig. 21. Capacitance of (a) PTB7-Th:PC₇₁BM and (b) PTB7-Th:N2200 electron-only devices as a function of voltage perturbation frequency at room temperature; and (c) electron mobilities of BHJ films in (a) and (b) as a function of applied electric field.

Noriega et al. investigated the microstructure of neat P3HT films [167], and found that, in such a case, the film comprises three separate but coexisting phases: (i) semi-ordered quasi-crystallized regions, (ii) amorphous regions, and (iii) long-chain polymeric molecule-linking, or (i) and (ii) together. In polymer:acceptor-disordered organic BHJs, hole carriers are mainly transported in ordered regions (i, iii), because significant energy barriers exist between ordered and amorphous regions. In another work, Salleo et al. investigated the microstructure of poly-thiophenes and found that hole carriers are usually transported rapidly in the conjugation direction in crystalline regions [168].

In SMA-based BHJs, the inter-molecular hopping is a well-established model to describe the electron transport, and therefore, such BHJ solar cells have highly electric field-dependent electron mobilities [149,150]. However, the electron transport process is not entirely identical with that in SMA-based BHJs. It is generally accepted that there are two electron pathways in all-polymer BHJs: (i) the inter-molecular hopping along the direction of $\pi-\pi$ stacking; and (ii) the

intramolecular transport along the backbone of the polymeric molecules [31]. Currently, N2200 is widely used as the polymeric acceptor in all-polymer solar cells. Taking N2200-based BHJs as examples, as the detour of electron carriers can happen in (ii), the noticeable characteristic of the electron transport in all-polymer BHJs is that the mobilities show suppressed Poole-Frenkel effect. The Poole-Frenkel slope β can be extracted from the mobility curves by the model equation $\mu(E) = \mu_0 \exp(\beta\sqrt{F})$ [169–177]. A small (or negative) β indicates the negligible energetic barrier exists in the forward direction, which is favorable for the electron transport. In contrast, a large positive β indicates on average a large energetic barrier for a charge carrier to exercise a forward hop, and is unfavorable. Admittance spectroscopy (AS) measurement is a powerful technique to evaluate such field-dependent properties of the charge carrier transport in organic semiconductors, and the principle of AS measurement has been well documented elsewhere [171]. In brief, the organic semiconductor to be investigated is sandwiched in between two electrodes. One of the electrode should

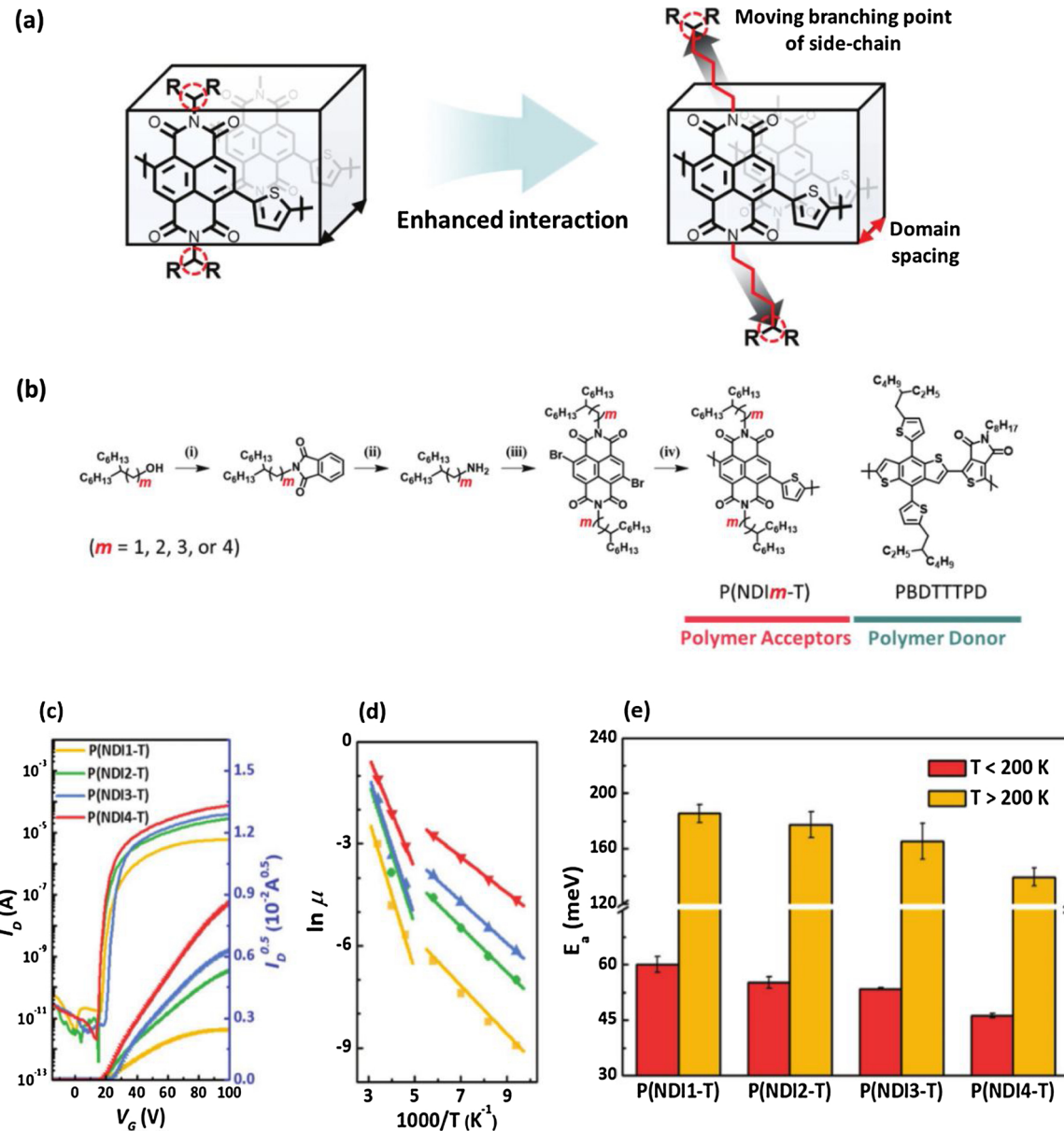


Fig. 22. (a) Schematic illustration of the design of P(NDIm-T) polymer with different branching points; (b) synthetic routes and chemical structure of NDI monomers, P(NDIm-T) polymers, and PBDDTTTPD; (c) transfer characteristics of n-channel OFETs based on thermally-annealed films; (d) Arrhenius plot of temperature dependent mobility; and (e) activation energy for charge-transport for different P(NDIm-T) polymers.

Reprinted with permission from Ref. [180]. Copyright 2018 Wiley-VCH.

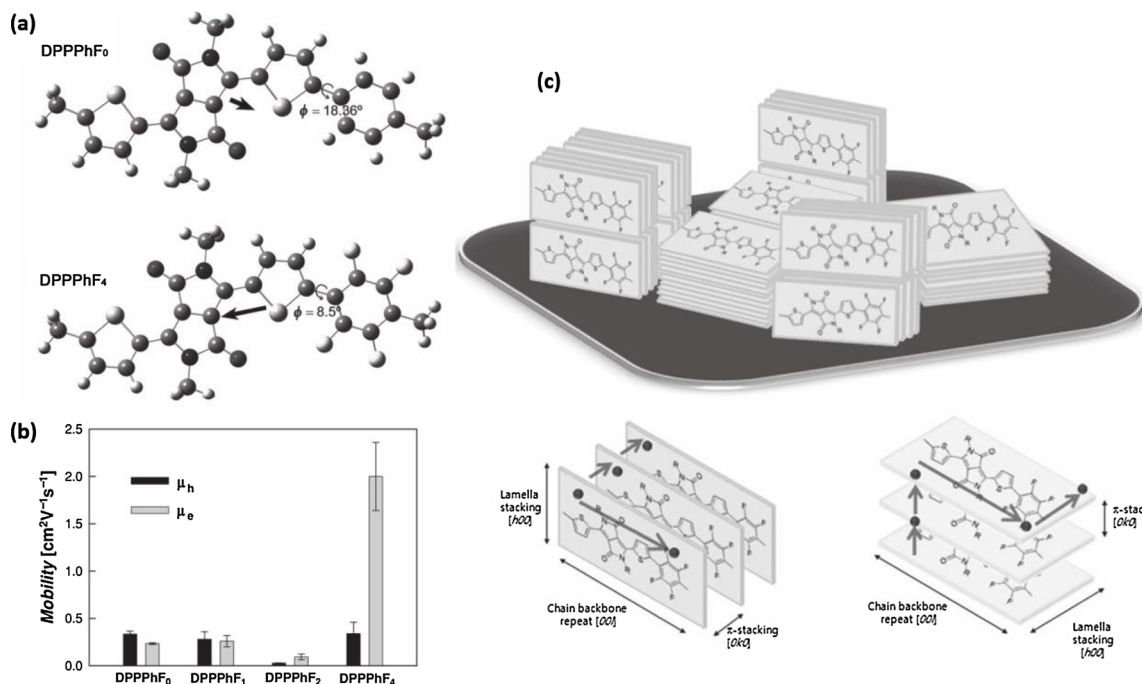


Fig. 23. (a) Calculated dipole moments and torsional angles in DPPPPhF₀ and DPPPPhF₄. The thick arrows denote the magnitude and direction of the dipole moment of the polymers; (b) comparison of hole and electron mobilities of four polymers with different fluorine substitutions. The values were averaged from at least 8 measurements for each device; and (c) schematic representation of charge-carrier transport of DPPPPhF₄ through edge-on and face-on orientation.

Reprinted with permission from Ref. [181]. Copyright 2013 Wiley-VCH.

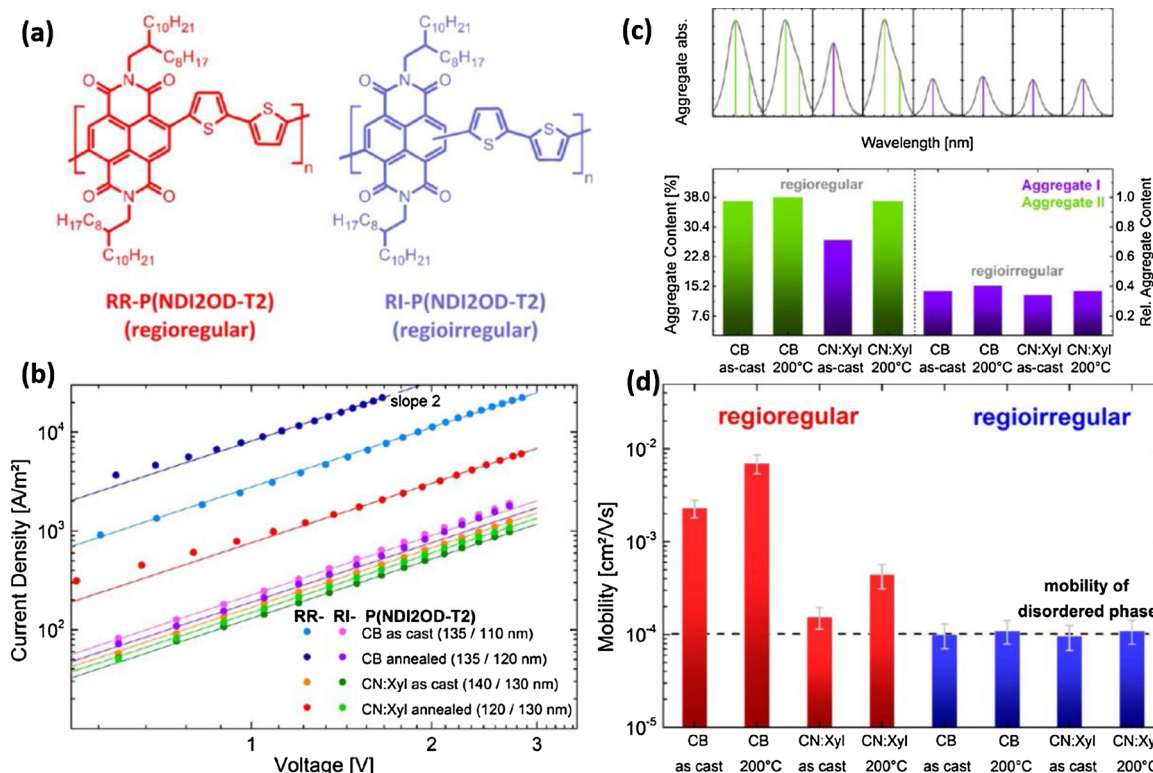


Fig. 24. (a) Chemical structures of RR-P(NDI2OD-T2) and RI-P(NDI2OD-T2); (b) $J-V$ characteristics of electron-only devices with different solvent and annealing treatments; (c) deconvolution of the amorphous and aggregate absorption features, showing the absorption of the aggregate species for the different films and aggregate content and type for each of the analyzed films, obtained from the ratio of the amorphous and aggregate absorption intensities; and (d) electron mobilities extracted from (b).

Reprinted with permission from Ref. [138]. Copyright 2010 Wiley-VCH.

form an Ohmic contact with the organic semiconductor. The device is then subjected to a dc voltage superimposed with a small ac voltage. The resulting ac current is then recorded from which the small signal capacitance (C) of the device can be extracted. Fig. 21 shows the capacitance signals of the electron-only all-polymer PTB7-Th:N2200 device and its counterpart, a fullerene-based PTB7-Th:PC₇₁BM device as a function of the ac frequency (f) at different dc applied electric field F [171]. Such a plot can be used to extract the electron or hole mobility when the device is configured as an electron-only or hole-only device, respectively. For PTB7-Th:PC₇₁BM BHJs configured as an electron-only device, the response frequency is sensitive to the electric field. The maximum negative differential susceptance ($-\Delta B$) can be extracted from the plot of $-\Delta B$ versus frequency (f), and defines the characteristic frequency f_r which can be used to compute the carrier transit time using the relationship $\tau_t = 0.56f_r^{-1}$. f_r significantly shifts toward the high-frequency region when the electric field increases in PTB7-Th:PC₇₁BM BHJs. In contrast, the f_r shift is less rapid for the all-polymer PTB7-Th:N2200 device. Using f_r , the field dependent electron mobility can be extracted and summarized in Fig. 21(c). The mobilities for the all-polymer BHJ show a slightly negative field dependent electron mobility. On the other hand, the electron mobilities for the PTB7-Th:PC₇₁BM BHJ exhibit a positive field dependence, and with a larger Poole-Frenkel slope. Fig. 21(c) also shows that all-polymer BHJs enjoy higher zero-field electron mobilities (10^{-4} to $10^{-3} \text{ cm}^2 \text{ V}^{-1} \text{ s}^{-1}$) than PTB7-Th:PC₇₁BM BHJ ($\sim 10^{-5} \text{ cm}^2 \text{ V}^{-1} \text{ s}^{-1}$).

In all-polymer BHJs, steric hindrance can significantly affect electron transport [178,179]. You et al. studied how the branching point of side-chain in a series of NDI-based n-type polymers affects the structure, carrier transport, and optical properties of a range of all-polymer BHJs [180]. Fig. 22 depicts the design strategy and chemical structures of four n-type polymeric acceptors P(NDIm-T) with different branching points. The results indicate the steric hindrance around the backbone is minimized when the branching point is located close to the backbone, and more efficient electron transport properties thus occur in such films.

When blended with the donor polymer PBDTTTPD, P(NDI3-T) and P(NDI4-T) BHJs with branching points remote from the conjugated backbone possess improved electron mobilities and balanced hole/electron mobility ratios, as shown by SCLC measurements. An active layer composed of P(NDI4-T) also exhibits satisfactory OFET performance. As summarized in Fig. 22(d), the P(NDI4-T) film shows a highest average electron mobility value of $(1.18 \pm 0.31 \times 10^{-1} \text{ cm}^2 \text{ V}^{-1} \text{ s}^{-1}$, reduced electron energetic disorder, and low activation energies for charge transport at different temperatures.

Park et al. synthesized a series of DPP-based semiconducting n-type polymers DPPPhF₀-DPPPhF₄, and evaluated their electron transport properties by the organic field-effect transistor characteristics [181]. In these polymers, fluorinated phenylene units are used as the building blocks to tune the torsional angles. As shown in Fig. 23, the DPPPhF₄ exhibits a smaller torsional angle of 8.5° , and correspondingly the highest electron mobility of $\sim 2 \text{ cm}^2 \text{ V}^{-1} \text{ s}^{-1}$, among the four DPP-based n-type polymers. Fig. 23(c) compares the carrier transport in DPPPhF₄ molecules through the edge-on and face-on orientations. Along the edge-on direction, charge carriers hop to subsequent layers and travels along the polymer backbone coupled by π -stacking, whereas in the face-on orientation, carriers can hop through the lamella-stacking direction or move through the chain axis.

Steyrleuthner et al. demonstrated how the structural regularity of the polymer backbone effects the electron transport properties [138]. Two n-type polymers were under investigated, involving the regioregular RR-P(NDI2OD-T2) and the regioirregular RI-P(NDI2OD-T2) shown in Fig. 24. The RR-P(NDI2OD-T2) films exhibit higher absorbances from the aggregation species, and larger aggregate contents than the RI-P(NDI2OD-T2) film by different solvent and thermal annealing

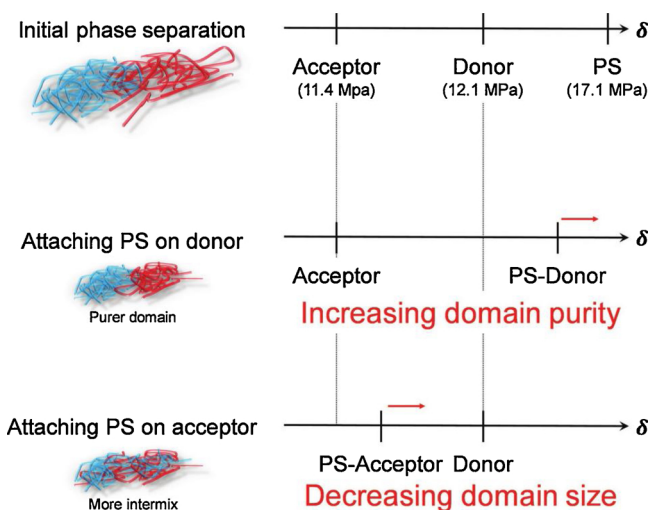


Fig. 25. Schematic illustration of the phase separation behavior in the blend film of D-PS_x/A-PS_x and the hypothetical order of solubility parameter of each polymer.

Reprinted with permission from Ref. [182]. Copyright 2018 Wiley-VCH.

conditions. Furthermore, electron mobilities are higher in RR-P(NDI2OD-T2) films. The RR film with the CB-coated treatment has ~ 10 times higher electron mobilities than the annealed CN:Xy-cast electron-only devices with an edge-on morphology, and this result indicates that the coherent π -stacking along the direction of charge transport is important for reaching high electron mobilities in such n-type polymer films.

Kurosawa et al. demonstrated how the oligomeric polystyrene side chains affected the solubility of conjugated polymers, and therefore the electronic characteristics in BHJ films [182]. According to the regular solution theory, the solubility parameter (δ) can be expressed as

$$\chi_{S-P} = \frac{V_S}{RT} (\delta_S - \delta_P)^2 + 0.34 \quad (2)$$

where χ_{S-P} is the Flory-Huggins solvent-polymer interaction parameter, V_S is the molar volume of solvent, R is the gas constant, δ_S is the solubility parameter of the solvent, and δ_P is the solubility parameter of the polymer. Various fractions of PS side chains ($X = 0, 5, 10 \text{ mol\%}$) in the repeating unit affects δ_P in the all-polymer solutions, and generate different phase separation conditions of their corresponding BHJ films. As shown in Fig. 25, by attaching PS side chains to the donor polymers, the solubility parameter difference between the donor polymers (D-PS₅ and D-PS₁₀) and acceptor polymer increases, compared to that between D-PS₀ and A-PS₀, leading to a higher tendency for phase separation to occur.

In BHJs with more than one acceptor, the mobility variation trends are highly dependent on the acceptor topology [183,184]. If one of the acceptors is a polymeric acceptor, it may dominate the electron transport in the resulting ternary BHJs. Yin et al. compares the electron transport parameters of ternary PBDB-T:ITIC-M:N2200 BHJs with different N2200 weight fractions, in which the two acceptors in their BHJs represent typical topologies discussed at the beginning of this section. A 10 wt% N2200 can remarkably improve the electron mobility in such a ternary BHJ with reduced energetic disorder and electron-hopping distance. Fig. 26 shows the electron mobilities of ITIC-M/PC₇₁BM and ITIC-M/N2200 films [185]. The electron mobility in the neat ITIC-M is lower than those in PC₇₁BM and N2200 films. A much lower N2200 fraction rapidly increases electron mobilities.

4.2. Donor:Acceptor weight fraction and Electron percolation

Donor:acceptor composition is an important parameter that affects

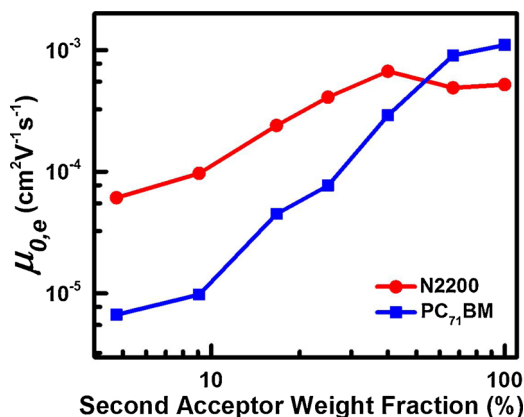


Fig. 26. Zero-field electron mobilities $\mu_{0,e}$ of ITIC-M/PC₇₁BM and ITIC-M/N2200 films with various PC₇₁BM/N2200 weight fractions.

Reprinted with permission from Ref. [185]. Copyright 2019 Wiley-VCH.

the properties and performance of OPV devices. Despite the importance, the optimization of BHJ composition is still performed primarily in a trial-and-error manner. Many groups reported the excellent tolerance of different D:A compositions in all-polymer solar cells [186,187]. Generally speaking, all-polymer solar cells have high composition tolerance, and better immunity to moisture and external tempering. Zhang et al. and Liu et al. both observed relatively high FFs in the donor-rich D:A regions of the PBDB-T:N2200 BHJ solar cells [109]. In a more recent report, Yin et. al. systematically correlated device performance to electron conduction in BHJs bearing fullerene, non-fullerene, and polymeric acceptors [188]. Fig. 27 summarizes their results. It shows the logarithm of electron mobility of (a) fullerene-based PTB7:PC₇₁BM; (b) NF SMA-

based PTB7-Th:ITIC; and (c) all-polymer PTB7-Th:N2200 BHJ films with different weight fractions of acceptor [189]. In each case, the electron mobility increases with the increase in the weight fraction of the acceptor. However, all-polymer BHJs are less sensitive to changes in D:A weight fractions than SMA-based BHJs, and this result is consistent with the FF variation shown in g-i.

From Fig. 27 (a)-(c), we observe that as the acceptor content increases, the electron mobility takes on two stages of evolution: first, a rapidly rising region corresponding to percolating electron domains as weight fraction of the acceptor initially increases, and second, a slowly rising region at higher acceptor weight fractions. Previously, the theory of percolation has been used to describe electrical conduction for conducting fillers dispersed in an insulating medium [189–191]. For the study of electron percolation in a BHJ, we can consider a BHJ as a medium with conductive fillers (acceptors) which are embedded in insulating materials (donors). In the vicinity of the percolating region, the overall conductivity of a film can be expressed as

$$\sigma \propto (\phi - \phi_c)^t \quad (3)$$

where t is a critical exponent, and ϕ_c is the critical volume fraction [192]. Eq. (3) describes the sharp increase in σ in the vicinity of ϕ_c , and it also assumes that the conducting components have physical contacts. In 2010, Ambrosetti *et. al.* introduced a new model which relaxes the requirement for physical contact. In Ambrosetti's model, charges are allowed to tunnel from one conducting filler to another nearby filler [193]. This tunneling-percolation model has two key components. First, the tunneling-conductance between two nearby fillers, i and j , with a minimal separation δ_{ij} , can be written as

$$g_{ij} = g_0 \exp\left(\frac{-2\delta_{ij}}{\xi}\right) \quad (4)$$

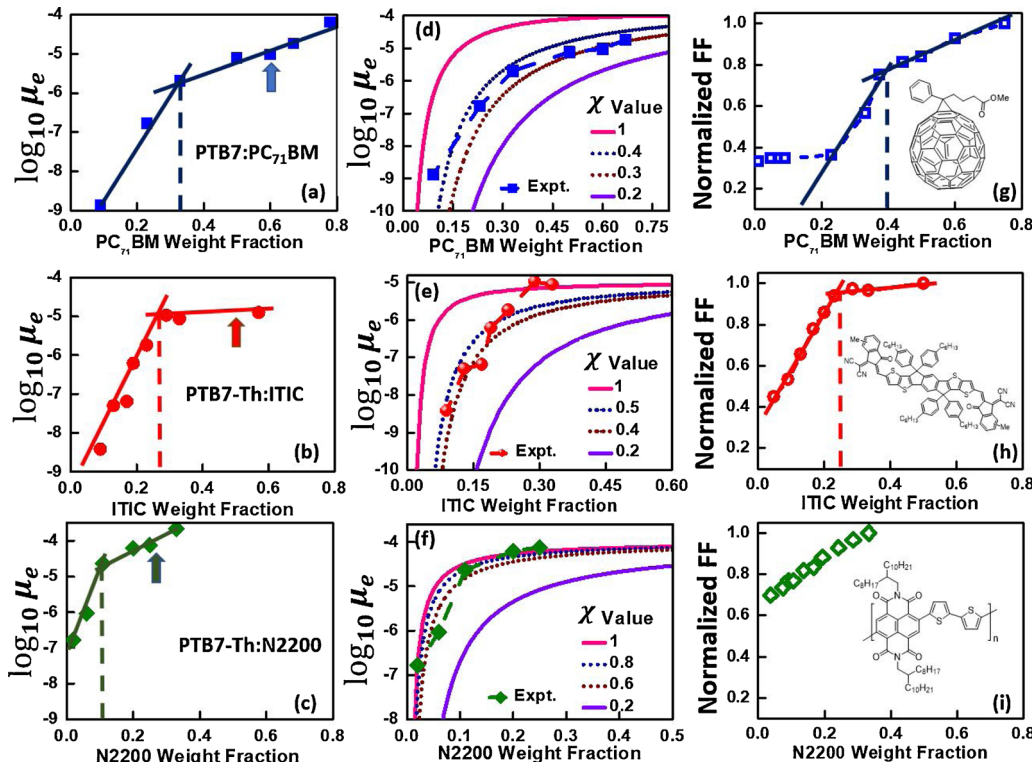


Fig. 27. (a–c) Logarithm of electron mobilities as a function of acceptor weight fraction for fullerene-based PTB7:PC₇₁BM (blue squares), small-molecule-based PTB7-Th:ITIC (red circles), and all-polymer PTB7-Th:N2200 (green diamonds) BHJs. The unit of μ_e is cm²V⁻¹s⁻¹. The arrows indicate the optimized compositions for the BHJs, and the vertical dashed lines indicate the compositions at which electron percolations complete; (d–f) transport data and fitting curves with various χ values; (g–i) normalized FFs of PTB7:PC₇₁BM, PTB7-Th:M, and PTB7-Th:N2200 BHJ solar cells vs D:A compositions.

Reprinted with permission from Ref. [188]. Copyright 2019 Elsevier.

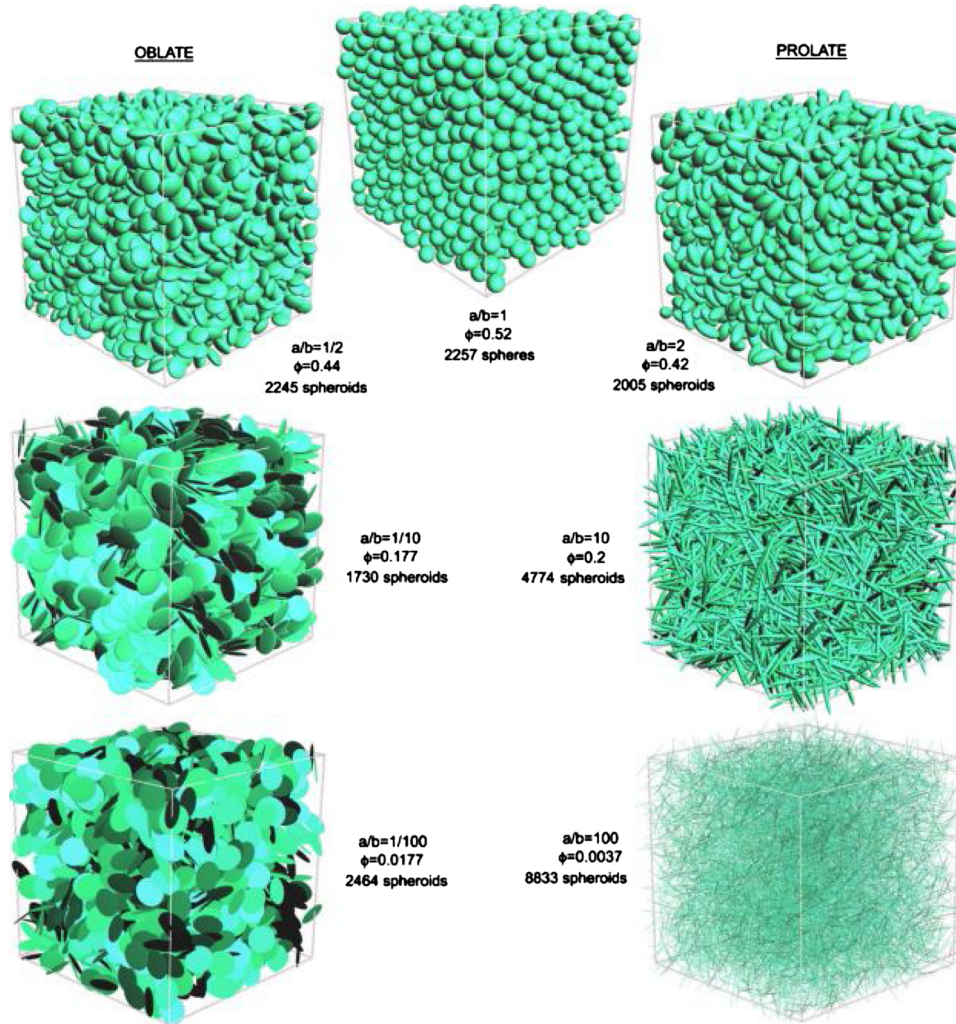


Fig. 28. Examples of distributions of impenetrable spheres and spheroids of different aspect ratios a/b and volume fraction ϕ generated by the algorithms used in the present work.

Reprinted with permission from Ref. [193]. Copyright 2010 American Physical Society.

where g_0 is a constant and ξ is the characteristic tunneling length. Second, the model further allows the conducting fillers to take on different shapes by assuming them as impenetrable ellipsoids with different aspect ratios a/b . When $a/b > 1$, the fillers are needle-like (prolates). When $a/b < 1$, the fillers take on a disc shape (oblates). If $a/b = 1$, then the fillers are spheres. Since $a \neq b$ in the general case, δ_c depends also on the relative orientations of the neighboring fillers.

Applying the global theory (GT) network technique, Ambrosetti simulated the overall conductivity. Up to 8000 spheroids were used in the simulations. Fig. 28 show examples of how such ensembles of conducting fillers distribute for fillers with different shapes. The conductivities of these ensembles of fillers were further computed and the results reproduced the dependence of σ on ϕ , similar to the behavior predicted by Eq. (3).

To check the reliability of the simulations, they also used the method of critical path (CP) to calculate the dependence of σ on ϕ . With the CP method, the conductance σ can be approximated by

$$\sigma \approx \sigma_0 \exp \left[-\frac{2\delta_c(\phi, a, b)}{\xi} \right] \quad (5)$$

where $\sigma_0 \propto g_0$, and δ_c is a function of the conductor filler fraction and their aspect ratio is a/b . For the special cases of $a/b \gg 1$, $a/b \ll 1$, and $a/b = 1$, the expressions for δ_c have the forms:

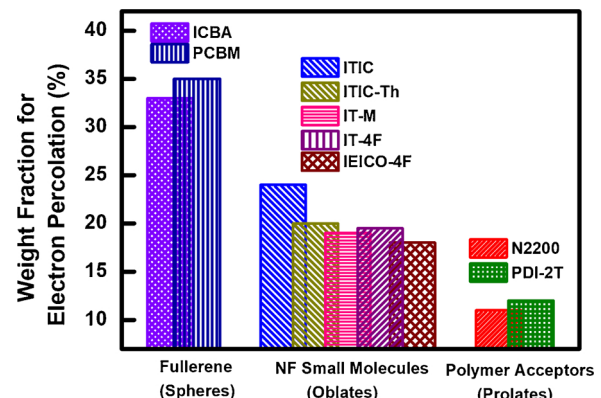


Fig. 29. Weight fractions for electron percolations for BHJs that contain (i) fullerene-based acceptors; (ii) non-fullerene (NF) small molecular acceptors; and (iii) polymer acceptors. The nano-topologies of (i), (ii), and (iii) can be thought to be spheres, oblates (flat plates); and prolates (long rods), respectively.

Reprinted with permission from Ref. [188]. Copyright 2019 Elsevier.

$$\delta_c \approx \frac{\gamma(b/a)^2}{\phi} \times D \text{ Prolate} \quad (6a)$$

$$\delta_c \approx \left[\frac{0.15(a/b)}{\phi} \right]^{4/3} \times D \text{ Oblate} \quad (6b)$$

$$\delta_c \approx \frac{1.65(1-\phi)^3}{12\phi(2-\phi)} \times D \text{ Sphere} \quad (6c)$$

where D is the center-to-center distance between two conducting units, and γ is 0.4 for spheroids. Following the CP model with the conductor filler fraction δ_c expressed in Equation (6), the tunneling conductivity formula in the percolating region in the form of mobility can be expressed as

$$\mu = \mu_{sat} \exp \left[-\frac{2D \gamma(b/a)^2}{\xi \phi} \right] \text{ Prolate} \quad (7a)$$

$$\mu = \mu_{sat} \exp \left\{ -\frac{2D}{\xi} \left[\frac{0.15(a/b)}{\phi} \right]^{4/3} \right\} \text{ Oblate} \quad (7b)$$

$$\mu = \mu_{sat} \exp \left[-\frac{2D}{\xi} \frac{1.65(1-\phi)^3}{12\phi(2-\phi)} \right] \text{ Sphere} \quad (7c)$$

The saturation mobilities μ_{sat} of BHJs are the electron mobilities of pure acceptor films. As shown in Fig. 27(d-f), the intersection of these two regions can be interpreted as the composition at which electron percolation completes. The acceptor weight fraction for the completion of electron percolation is successively reduced in the order of fullerene, NF SMAs, and polymer, indicating good electron transport properties in all-polymer BHJs. Apparently, even after electron percolations complete, BHJs require more electron conduction pathways, and higher acceptor contents to achieve compositions required for optimized PCEs.

From the Ambrosetti model, calculated mobility values are always larger than the experimental results in PC₇₁BM-, ITIC-, and N2200-based BHJs with different D:A weight compositions. Two assumptions were proposed to explain the deviations between the simulation model and experimental results: (i) impenetrable objects are identical, and dispersed uniformly in a continuous insulating medium; and (ii) there are no interactions between conducting/insulating or conducting/conducting phases. However, in BHJs, electron acceptors have self-aggregations, and some of them can even dock with donor molecules. Therefore, the concept of effective weight fraction χ , is introduced to

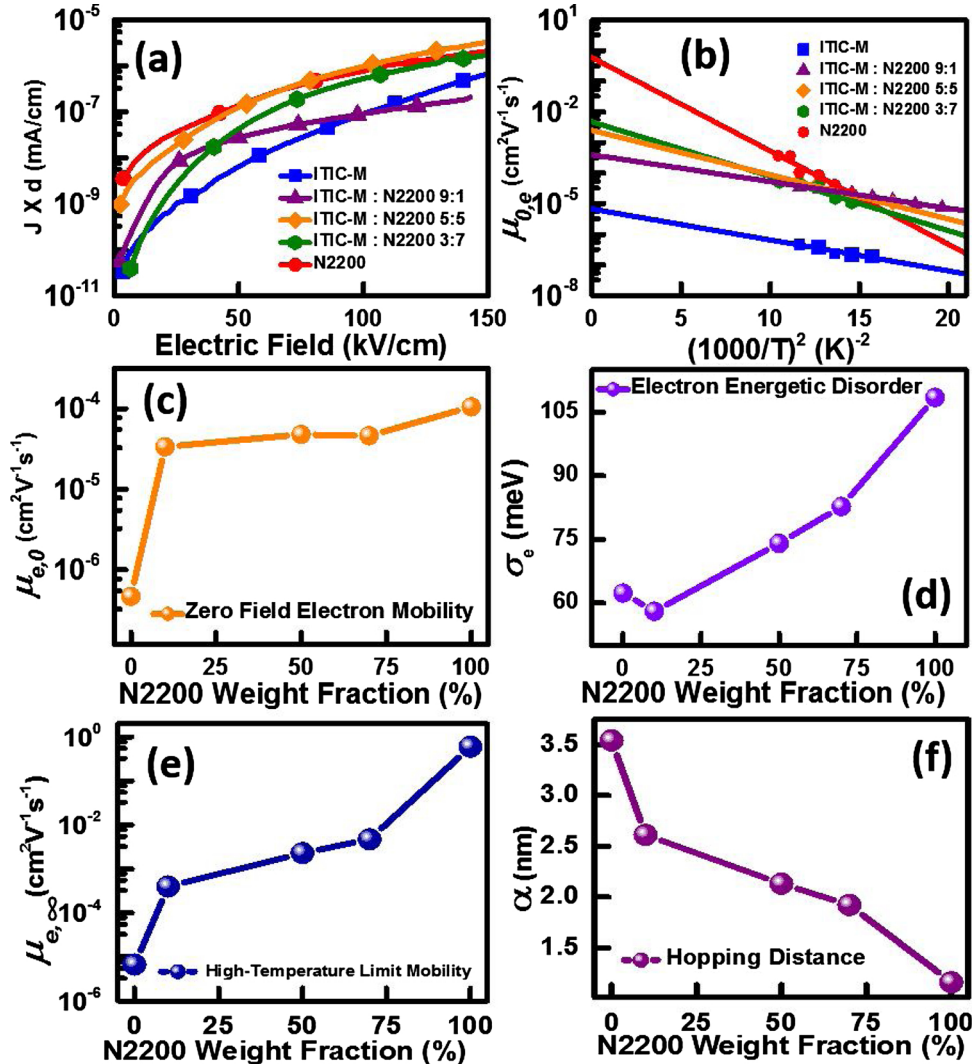


Fig. 30. Electron carrier transport results for the binary PBDB-T:ITIC-M, PBDB-T:N2200, and ternary PBDB-T:N2200:ITIC-M BHJs with different N2200 weight fractions: (a) $J \times d$ as a function of the applied electric field; (b) zero-field electron mobilities $\mu_{e,0}$ vs $1/T^2$; (c) $\mu_{e,0}$ at the room temperature; (d) energetic disorders of electron carriers σ_e ; (e) high-temperature limits of electron mobility $\mu_{e,\infty}$; and (f) average hopping distances of electron carriers α .

Reprinted with permission from Ref. [185]. Copyright 2019 Wiley-VCH.

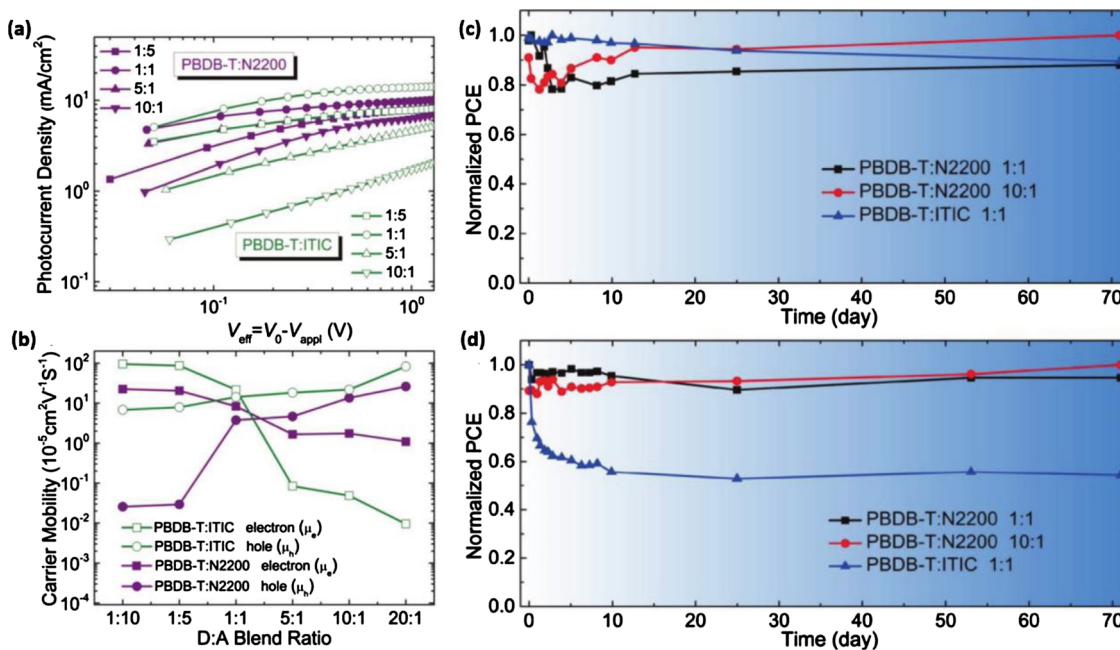


Fig. 31. Photocurrent (a) and (b) electron and hole mobilities of PBDB-T:ITIC and PBDB-T:N2200 with different D:A blend ratios; (c) stability of solar cell devices based on PBDB-T:N2200 (D:A = 1:1 and 10:1) PBDB-T:ITIC (D:A = 1:1) under the dark condition, and (d) thermal stability of solar cell devices based on PBDB-T:N2200 (D:A = 1:1 and 10:1) PBDB-T:ITIC (D:A = 1:1).

Reprinted with permission from Ref. [109]. Copyright 2018 Wiley-VCH.

evaluate the percentage of electron acceptors which indeed contribute the electron transport in BHJs. All-polymer PTB7-Th:N2200 BHJs exhibit large χ values, which is favorable for the electron transport in such BHJs. Fig. 29 lists the weight fractions required for electron percolation in several widely used BHJs with different electron acceptors. The acceptor weight fractions are approximately 0.11 for electron percolation in all-polymer BHJs, whereas fullerene-based and NF SMA-based BHJs require the largest acceptor weight fractions (> 0.3 and ~0.2, respectively) for full percolation to occur.

As polymeric acceptors have larger access to form well-established percolating network for the electron transport, it can be also applied into SMA-based binary BHJs to improve the electron transport properties in such films. Fig. 30 shows how the third component N2200 effects the electronic properties of the binary PBDB-T:PTC-M BHJs. At low electric fields, a low dosage (10 wt%) polymeric acceptor N2200 can already improve the zero-field electron mobility from 4.7×10^{-7} cm²V⁻¹s⁻¹ to 3.4×10^{-5} cm²V⁻¹s⁻¹ in the ternary film. Meanwhile, such N2200-based BHJs exhibit reduced σ_c and α . As the concentration of N2200 increase, α decreases monotonically from 3.5 nm in the PBDB-T:IT-M cell, to 0.83 nm in the binary all-polymer PBDB-T:N2200 BHJ device.

Many papers report that all-polymer solar cells enjoy desirable

device stabilities under different conditions, such as moisture/oxygen exposure and temperature annealing. The morphological tolerance in D:A composition and the intra-molecular electron transport model are two important reasons for the excellent stability of all-polymer solar cells. Zhang et al. investigated the effects of D:A compositions for the carrier transport properties, OPV performance and device stability of SMA-based PBDB-T:ITIC and all-polymer PBDB-T:N2200 BHJ solar cells [109]. Fig. 31 shows the photocurrent of the hole- and electron-only devices with different D:A weight ratios of 1:5, 1:1, 5:1, and 10:1, and the corresponding mobilities are summarized in (b). The all-polymer PBDB-T:N2200 exhibits high mobility tolerance in different D:A weight ratios for the electron transport. Such all-polymer BHJ solar cells enjoy much improved thermal stability as shown in (d). After 70 days, the normalized PCEs for both 1:1 and 10:1 devices still maintain over 90 % of their initial efficiencies, whereas the PBDB-T:ITIC device only exhibits a low normalized PCE ~50 % after the same annealing time.

Pietro et al. investigated the oxygen- and water-induced electron traps and electron transporting stabilities in the n-type polymer P (NDI2OD-T2) [194]. The reduction of electron mobilities in N2200 films (Fig. 32) can be attributed to the interaction between the oxygen molecules and the neutral N2200 polymers when exposure in the oxygen exposure conditions. The density functional theory quantum

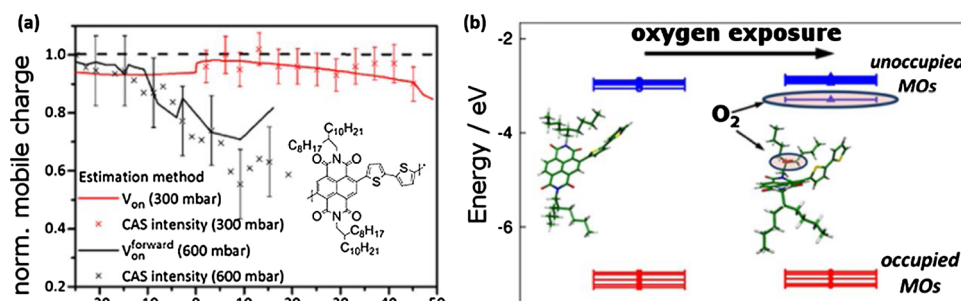


Fig. 32. (a) Normalized mobile charge of the N2200 transistor transfer characteristics upon dry air exposure (pressure 300/600 mbar); and (b) the schematic diagram of the oxygen effect for the electron trap states of the N2200 films.

Reprinted with permission from Ref. [194]. Copyright 2012 American Chemical Society.

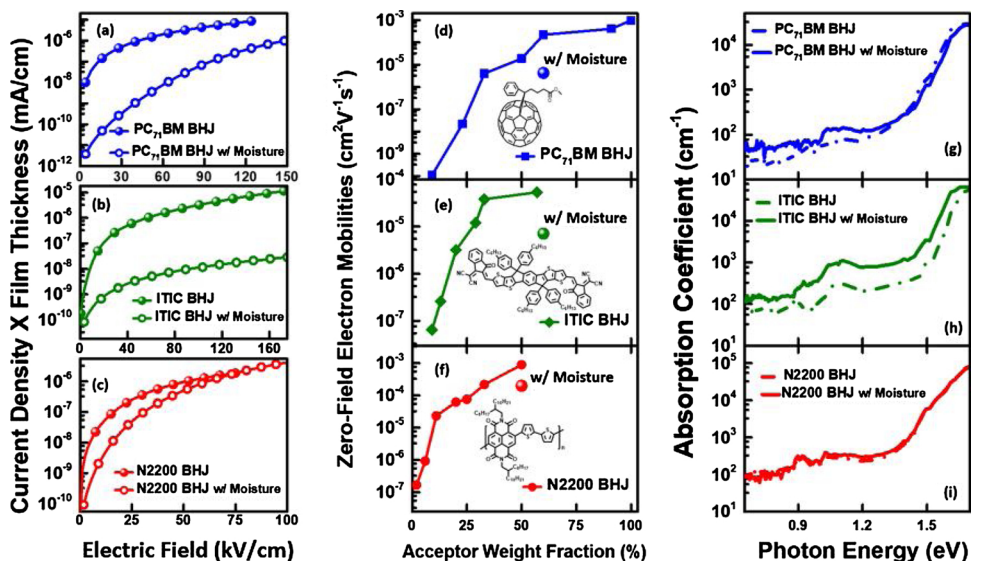


Fig. 33. (a–c) Electron current density \times film thickness of BHJs as a function of the applied electric field for PTB7:PC₇₁BM, PTB7-Th:ITIC and PTB7-Th:N2200 BHJs w/ and w/o the moisture treatment; (d–f) electron mobilities as a function of acceptor weight fraction from the SCLC measurements; (g–i) subgap optical absorption of optimized PTB7:PC₇₁BM, PTB7-Th:ITIC and PTB7-Th:N2200 BHJs w/ and w/o the moisture treatment.

Reprinted with permission from Ref. [188]. Copyright 2019 Elsevier.

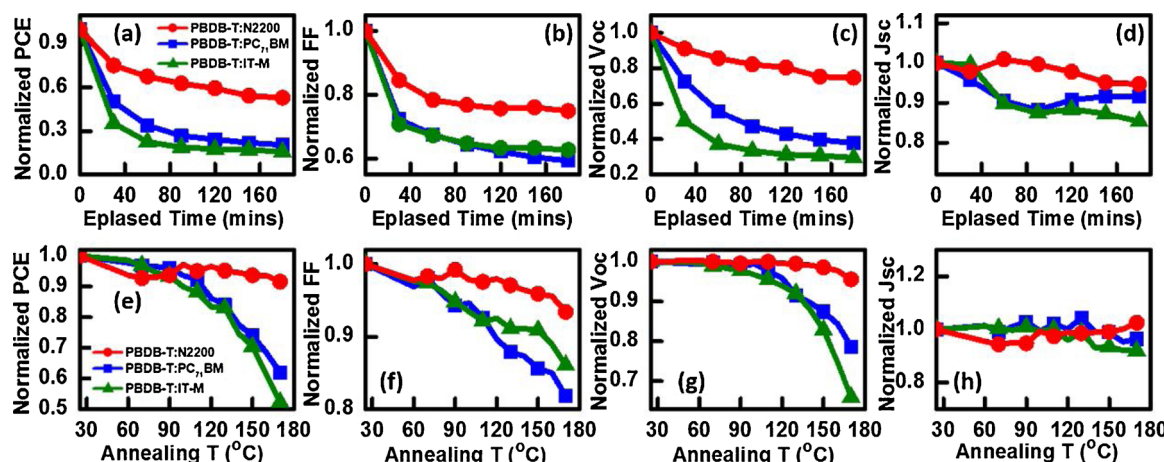


Fig. 34. Normalized OPV parameters of PBDB-T:PC₇₁BM, PBDB-T:IT-M and PBDB-T:N2200 BHJ solar cells under high humidity air (RH \sim 80 %) condition (a–d); and post annealing in N₂ filled glove box with different temperatures.

chemical calculations indicates the degradation in electron mobilities is from the formation of a shallow, localized, oxygen-induced trap level, 0.34 eV below the delocalized lowest unoccupied molecular orbital of P (NDI2OD-T2).

Yin et al. also evaluated the electron mobilities and energetic defects of all-polymer PTB7-Th:N2200 BHJs and their counterpart BHJs with PC₇₁BM and ITIC before and after the exposure in the high humidity condition. As shown in Fig. 33, although electron mobilities decayed in all optimized BHJs with different acceptors after the high-humidity treatment, the N2200-based BHJ reserves a percolated mobility value, whereas the moisture deteriorates the percolation of electron transport in other two SMA-based films. Meanwhile, the moisture-induced energetic defects were evaluated by the photothermal deflection spectroscopy (PDS), and the results indicated that the all-polymer BHJ shows a much improved moisture tolerance than other cases.

Fig. 34 compares the heat- and moisture/oxygen-stability of three PBDB-T-based BHJ solar cells with different acceptors (PC₇₁BM, ITIC-M, or N2200). It can be seen that the all-polymer PBDB-T:N2200 BHJ solar cell has superior device stability to its two counterparts, in both high moisture (RH \sim 75–85 %) and high temperature conditions.

Kim et al. demonstrated a mechanically flexible high-performance all-polymer PBDTTTPD:P(NDI2HD-T) BHJ solar cell system and compared its bending stability with that of its fullerene-based counterpart

PBDTTTPD:PCBM [195]. As shown in Fig. 35 the device was composed of polyimide/BHJ/Au, and the device performance was evaluated after the plastic substrate was subjected to mechanical bending. The results indicate that all-polymer BHJ solar cells display significantly better retention of conductance ability than a fullerene-based system after a variety of bending conditions [radii (*r*) and times]. For the PCBM based BHJ (d), cracks appear in the surface after bending at *r* = 1 mm, whereas the all-polymer blending film exhibit improved bending stability (e).

5. Conclusions and outlook

In recent years, researchers have made great progress in designing and fabricating all-polymer BHJ solar cells. Among several widely used materials such as CN-PPV, BTD-based polymers, and rylene diimide-based polymers, N2200 is still the dominant n-type polymeric acceptor used in OPV devices, and the efficiency of N2200-based solar cells has already exceeded 11 %. Compared to SMA-based (fullerene/non-fullerene) devices, all-polymer solar cells exhibit excellent and unique electron transport properties and display improved morphological tolerance to D:A compositions and (solvent vapor) annealing treatments. Below, we list the key advances in all-polymer BHJ solar cells from the perspective of their chemical structures, film morphology, and charge transport properties.

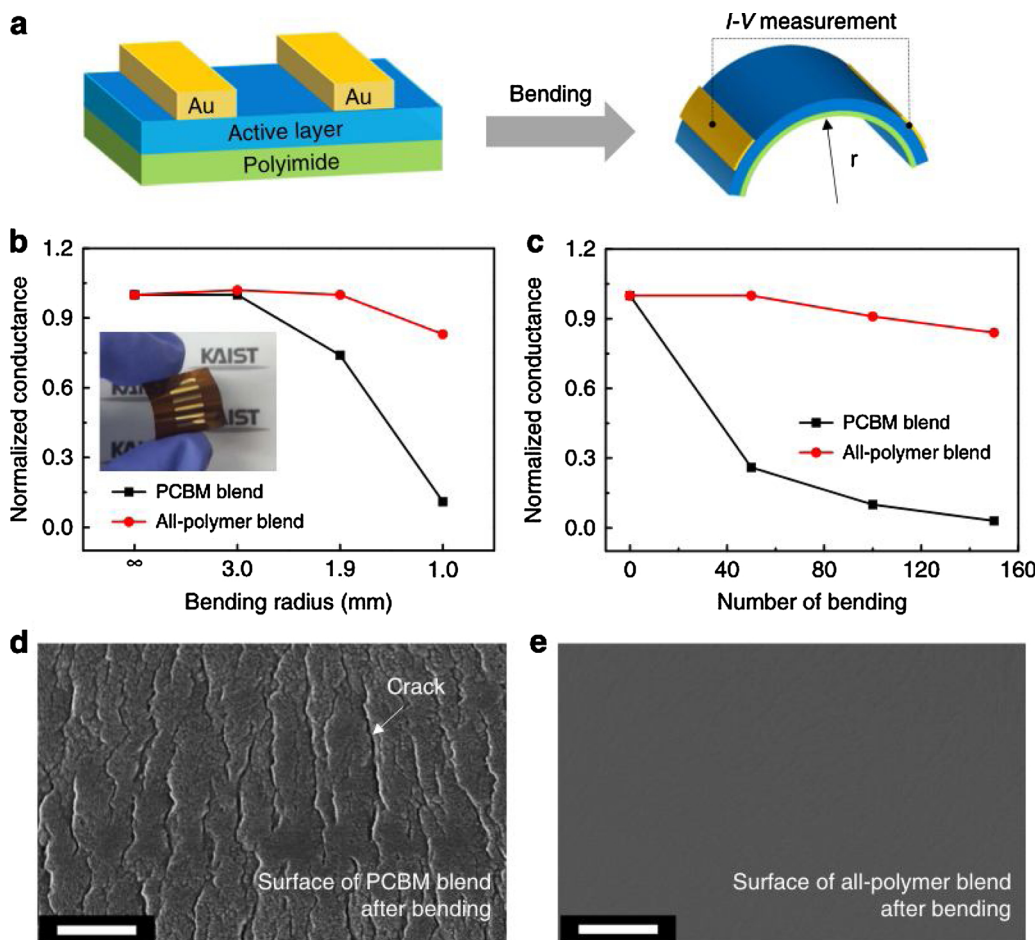


Fig. 35. Blending test of PBDTTTPD:PCBM and PBDTTTPD:P(NDI2HD-T) blend films. (a) Scheme of the BHJ blend film deposited on the flexible plastic substrate under mechanical bending. Normalized conductance of PBDTTTPD:PCBM and PBDTTTPD:P(NDI2HD-T) blend films (b) after bending at various *r* values and (c) after multiple cycles of bending at *r* = 1.5 mm. SEM images of surface morphologies of (d) PBDTTTPD:PCBM and (e) PBDTTTPD:P(NDI2HD-T) blend films after bending at *r* = 1.0 mm. The scale bars are 500 nm.

Reprinted with permission from Ref. [195]. Copyright 2015 Nature Publishing Group.

- 1 Rapid advances have recently been made in the development of polymeric acceptors for the active layer of BHJ OSCs, with rylene diimides providing the most promising results with the champion PCE over 11 %, followed closely by the emerging polymeric acceptors based on B—N, indacenodithiophene, and bithiophene imide.
- 2 The molecular weight of polymer donor(s)/acceptor(s) and their relative ratio not only affect the packing behavior of donor(s)/acceptor(s) molecules, but also the morphology of blended films.
- 3 Active-layer processing engineering plays a critical role in tuning the blend-film morphology, in terms of drying kinetics and molecular orientation control, to achieve an optimized phase-separated structure. This requires the correct choice of solvents, additives, coating methods, and other conditions.
- 4 Post-treatments such as thermal annealing and solvent vapor annealing can also affect the morphology of all-polymer blend films by enhancing the packing of polymer(s)/donor(s) molecules.
- 5 In all-polymer BHJs, electron transport is enhanced by suppressed Poole-Frenkel effect and reduced energetic disorder.
- 6 A high effective volume fraction χ is observed in P(NDI2OD-T2)-(N2200)-based BHJs, indicating a superior electron-transporting pathway exists in all-polymer BHJs, compared to those present in other active-layer type polymers. Therefore, we expect all-polymer BHJs to be highly tolerant to compositional variations.

This review aims to highlight the great potential that exists for rapid

efficiency improvement of all-polymer solar cells, via the use of innovative materials as the n-type polymeric acceptors. In addition, it is noteworthy that all-polymer solar cells have superior electron transport properties and higher processing tolerance than their SMA-based counterpart BHJs. We expect that n-type polymeric acceptors will enable the fabrication of high-performance, air-stable, and large-area all-polymer solar cells, leading to development and commercialization of a new generation of OSCs.

Declaration of Competing Interest

We declare no competing interests.

Acknowledgements

Support of this work by the Research Grant Council of Hong Kong under Grant #NSFC/RGC N-HKBU 202/16, and the Research Committee of HKBU under Grant #RC-ICRS/15-16/4A-SSK is gratefully acknowledged. G. Li thanks the support from Research Grants Council of Hong Kong (Project Nos 15218517, C5037-18G), Shenzhen Science and Technology Innovation Commission (Project No. JCYJ20170413154602102).

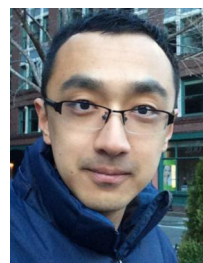
References

- [1] M.Z. Jacobson, Energy Environ. Sci. 2 (2009) 148–173.

- [2] J. Chow, R.J. Kopp, P.R. Portney, *Science* 302 (2003) 1528.
- [3] B.K. Bose, *IEEE Ind. Electron. Mag.* 4 (2010) 6–17.
- [4] I. Dincer, *Renew. Sust. Energy Rev.* 4 (2000) 157–175.
- [5] J.A. Turner, *Science* 285 (1999) 687.
- [6] M. Liserre, T. Sauter, J.Y. Hung, *IEEE Ind. Electron. Mag.* 4 (2010) 18–37.
- [7] S.A. Kalogirou, *Renew. Sust. Energy Rev.* 5 (2001) 373–401.
- [8] S.R. Bull, *IEEE* 89 (2001) 1216–1226.
- [9] N.S. Lewis, *Science* 315 (2007) 798.
- [10] H. Lund, *Energy* 32 (2007) 912–919.
- [11] S. Jacobsson, A. Johnson, *Energy Policy* 28 (2000) 625–640.
- [12] Y.J. Cheng, S.H. Yang, C.S. Hsu, *Chem. Rev.* 109 (2009) 5868–5923.
- [13] H. Hoppe, N.S. Sariciftci, *J. Mater. Res.* 19 (2004) 1924–1945.
- [14] A. Hagfeldt, G. Boschloo, L. Sun, L. Kloo, H. Pettersson, *Chem. Rev.* 110 (2010) 6595–6663.
- [15] J.L. Brédas, J.E. Norton, J. Cornil, V. Coropceanu, *Acc. Chem. Res.* 42 (2009) 1691–1699.
- [16] C. Yan, S. Barlow, Z. Wang, H. Yan, A.K.Y. Jen, S.R. Marder, X. Zhan, *Nat. Rev. Mater.* 3 (2018) 18003.
- [17] S.J. Xu, Z. Zhou, W. Liu, Z. Zhang, F. Liu, H. Yan, X. Zhu, *Adv. Mater.* 29 (2017).
- [18] J. Wang, J. Zhang, Y. Xiao, T. Xiao, R. Zhu, C. Yan, Y. Fu, G. Lu, X. Lu, S.R. Marder, X. Zhan, *J. Am. Chem. Soc.* 140 (2018) 9140–9147.
- [19] Y. Lin, F. Zhao, Q. He, L. Huo, Y. Wu, T.C. Parker, W. Ma, Y. Sun, C. Wang, D. Zhu, A.J. Heeger, S.R. Marder, X. Zhan, *J. Am. Chem. Soc.* 138 (2016) 4955–4961.
- [20] Y. Lin, X. Zhan, *Acc. Chem. Res.* 49 (2016) 175–183.
- [21] Y. Lin, X. Zhan, *Mater. Horiz.* 1 (2014) 470–488.
- [22] Y. Lin, J. Wang, Z.G. Zhang, H. Bai, Y. Li, D. Zhu, X. Zhan, *Adv. Mater.* 27 (2015) 1170–1174.
- [23] S. Dai, F. Zhao, Q. Zhang, T.K. Lau, T. Li, K. Liu, Q. Ling, C. Wang, X. Lu, W. You, X. Zhan, *J. Am. Chem. Soc.* 139 (2017) 1336–1343.
- [24] P. Cheng, G. Li, X. Zhan, Y. Yang, *Nat. Photonics* 12 (2018) 131–142.
- [25] S. Chandrasekhar, K. Chen, A.J. Barker, J.J. Sutton, S.K.K. Prasad, J. Zhu, J. Zhou, K.C. Gordon, Z. Xie, X. Zhan, J.M. Hodgkiss, *J. Am. Chem. Soc.* 141 (2019) 6922–6929.
- [26] Best Research-Cell Efficiency Chart, NREL, (2019) <https://www.nrel.gov/pv/cell-efficiency.html>.
- [27] L. Meng, Y. Zhang, X. Wan, C. Li, X. Zhang, Y. Wang, X. Ke, Z. Xiao, L. Ding, R. Xia, H.L. Yip, Y. Cao, Y. Chen, *Science* 361 (2018) 1094.
- [28] P. Cheng, X. Zhan, *Chem. Soc. Rev.* 45 (2016) 2544–2582.
- [29] K. Kawano, R. Pacios, D. Poplavskyy, J. Nelson, D.D.C. Bradley, J.R. Durrant, *Sol. Energy Mater. Sol. Cells* 90 (2006) 3520–3530.
- [30] M. Jørgensen, K. Norrman, F.C. Krebs, *Sol. Energy Mater. Sol. Cells* 92 (2008) 686–714.
- [31] C. Lee, S. Lee, G. Kim, W. Lee, B.J. Kim, *Chem. Rev.* 119 (2019) 8028–8086.
- [32] X. Zhan, Z.A. Tan, B. Domercq, Z. An, X. Zhang, S. Barlow, Y. Li, D. Zhu, B. Kippelen, S.R. Marder, *J. Am. Chem. Soc.* 129 (2007) 7246–7247.
- [33] J. Choi, K.H. Kim, H. Yu, C. Lee, H. Kang, I. Song, Y. Kim, J.H. Oh, B.J. Kim, *Chem. Mater.* 27 (2015) 5230–5237.
- [34] M.M. Mandoc, W. Veurman, L.J.A. Koster, M.M. Koetse, J. Sweelssen, B. Boer, P.W.M. Blom, *J. Appl. Phys.* 101 (2007) 104512.
- [35] Z. Li, W. Zhang, X. Xu, Z. Genene, D. Di Carlo Rasi, W. Mammo, A. Yartsev, M.R. Andersson, R.A.J. Janssen, E. Wang, *Adv. Energy Mater.* 7 (2017).
- [36] X. Gu, Y. Zhou, K. Gu, T. Kurosawa, Y. Guo, Y. Li, H. Lin, B.C. Schroeder, H. Yan, F. Molina-Lopez, C.J. Tassone, C. Wang, S.C.B. Mannsfeld, H. Yan, D. Zhao, M.F. Toney, Z. Bao, *Adv. Energy Mater.* 7 (2017) 1602742.
- [37] Y. Liu, T.T. Larsen-Olsen, X. Zhao, B. Andreassen, R.R. Søndergaard, M. Helgesen, K. Norrman, M. Jørgensen, F.C. Krebs, X. Zhan, *Sol. Energy Mater. Sol. Cells* 112 (2013) 157–162.
- [38] Z. Li, L. Ying, P. Zhu, W. Zhong, N. Li, F. Liu, F. Huang, Y. Cao, *Energy Environ. Sci.* 12 (2019) 157–163.
- [39] G. Wang, N.D. Eastham, T.J. Aldrich, B. Ma, E.F. Manley, Z. Chen, L.X. Chen, M.O. de la Cruz, R.P.H. Chang, F.S. Melkonyan, A. Facchetti, T.J. Marks, *Adv. Energy Mater.* 8 (2018) 1702173.
- [40] A. Onwubiko, W. Yue, C. Jellett, M. Xiao, H.-Y. Chen, M.K. Ravva, D.A. Hanifi, A.C. Knall, B. Purushothaman, M. Nikolka, J.-C. Flores, A. Salleo, J.-L. Bredas, H. Sirringhaus, P. Hayoz, I. McCulloch, *Nat. Commun.* 9 (2018) 416.
- [41] J.J.M. Halls, C.A. Walsh, N.C. Greenham, E.A. Marseglia, R.H. Friend, S.C. Moratti, A.B. Holmes, *Nature* 376 (1995) 498–500.
- [42] G. Yu, A.J. Heeger, *J. Appl. Phys.* 78 (1995) 4510–4515.
- [43] M. Granström, K. Petritsch, A.C. Arias, A. Lux, M.R. Andersson, R.H. Friend, *Nature* 395 (1998) 257–260.
- [44] A.J. Breeze, Z. Schlesinger, S.A. Carter, H. Tillmann, H.H. Hörrhold, *Sol. Energy Mater. Sol. Cells* 83 (2004) 263–271.
- [45] T. Kietzke, H.H. Hörrhold, D. Neher, *Chem. Mater.* 17 (2005) 6532–6537.
- [46] G. Sang, Y. Zou, Y. Huang, G. Zhao, Y. Yang, Y. Li, *Appl. Phys. Lett.* 94 (2009) 193302.
- [47] C.R. McNeill, A. Abrusci, J. Zaumseil, R. Wilson, M.J. McKiernan, J.H. Burroughes, J.J.M. Halls, N.C. Greenham, R.H. Friend, *Appl. Phys. Lett.* 90 (2007) 193506.
- [48] D. Mori, H. Benten, H. Ohkita, S. Ito, K. Miyake, *ACS Appl. Mater. Inter.* 4 (2012) 3325–3329.
- [49] Y. Cao, T. Lei, J. Yuan, J.-Y. Wang, J. Pei, *Polym. Chem.* 4 (2013) 5228–5236.
- [50] S. Liu, X. Song, S. Thomas, Z. Kan, F. Cruciani, F. Laquai, J.-L. Bredas, P.M. Beaujuge, *Adv. Energy Mater.* 7 (2017) 1602574.
- [51] Q. Hou, Y. Xu, W. Yang, M. Yuan, J. Peng, Y. Cao, J. Mater. Chem. 12 (2002) 2887–2892.
- [52] D. Mori, H. Benten, J. Kosaka, H. Ohkita, S. Ito, K. Miyake, *ACS Appl. Mater. Inter.* 3 (2011) 2924–2927.
- [53] J.E. Anthony, A. Facchetti, M. Heeney, S.R. Marder, X. Zhan, *Adv. Mater.* 22 (2010) 3876–3892.
- [54] J. Wang, X. Zhan, *Trend Chem.* 1 (2019) 869–881.
- [55] X. Zhao, X. Zhan, *Chem. Soc. Rev.* 40 (2011) 3728–3743.
- [56] X. Zhan, D. Zhu, *Polym. Chem.* 1 (2010) 409–419.
- [57] X. Zhan, Z.A. Tan, E.J. Zhou, Y.F. Li, R. Misra, A. Grant, B. Domercq, X.H. Zhang, Z.S. An, X. Zhang, S. Barlow, B. Kippelen, S.R. Marder, *J. Mater. Chem.* 19 (2009) 5794–5803.
- [58] Z.A. Tan, E.J. Zhou, X. Zhan, X. Wang, Y.F. Li, S. Barlow, S.R. Marder, *Appl. Phys. Lett.* 93 (2008) 073309.
- [59] J. Huang, Y. Wu, H. Fu, X. Zhan, J. Yao, S. Barlow, S.R. Marder, *J. Phys. Chem. A* 113 (2009) 5039–5046.
- [60] P. Cheng, L. Ye, X.G. Zhao, J.H. Hou, Y.F. Li, X. Zhan, *Energy Environ. Sci.* 7 (2014) 1351–1356.
- [61] P. Cheng, C.Q. Yan, Y.F. Li, W. Ma, X. Zhan, *Energy Environ. Sci.* 8 (2015) 2357–2364.
- [62] E. Zhou, K. Tajima, C.H. Yang, K. Hashimoto, *J. Mater. Chem.* 20 (2010) 2362–2368.
- [63] E. Zhou, J. Cong, Q. Wei, K. Tajima, C. Yang, K. Hashimoto, *Angew. Chem. Int. Ed.* 50 (2011) 2799–2803.
- [64] Y. Zhou, Q.F. Yan, Y.Q. Zheng, J.Y. Wang, D.H. Zhao, J. Pei, *J. Mater. Chem. A* 1 (2013) 6609–6613.
- [65] Y. Zhou, T. Kurosawa, W. Ma, Y. Guo, L. Fang, K. Vandewal, Y. Diao, C. Wang, Q. Yan, J. Reinschach, J. Mei, A.L. Appleton, G.I. Koleilat, Y. Gao, S.C. Mannsfeld, A. Salleo, H. Ade, D. Zhao, Z. Bao, *Adv. Mater.* 26 (2014) 3767–3772.
- [66] Y. Diao, Y. Zhou, T. Kurosawa, L. Shaw, C. Wang, S. Park, Y. Guo, J.A. Reinschach, K. Gu, X. Gu, B.C. Tee, C. Pang, H. Yan, D. Zhao, M.F. Toney, S.C. Mannsfeld, Z. Bao, *Nat. Commun.* 6 (2015) 7955.
- [67] Y. Guo, Y. Li, O. Awartani, J. Zhao, H. Han, H. Ade, D. Zhao, H. Yan, *Adv. Mater.* 28 (2016) 8483–8489.
- [68] Y.K. Guo, Y.K. Li, O. Awartani, H. Han, J.B. Zhao, H. Ade, H. Yan, D.H. Zhao, *Adv. Mater.* 29 (2017).
- [69] H. Yan, Z. Chen, Y. Zheng, C. Newman, J.R. Quinn, F. Dotz, M. Kastler, A. Facchetti, *Nature* 457 (2009) 679–686.
- [70] J.R. Moore, S. Albert-Seifried, A. Rao, S. Massip, B. Watts, D.J. Morgan, R.H. Friend, C.R. McNeill, H. Sirringhaus, *Adv. Energy Mater.* 1 (2011) 230–240.
- [71] L. Ye, X. Jiao, M. Zhou, S. Zhang, H. Yao, W. Zhao, A. Xia, H. Ade, J. Hou, *Adv. Mater.* 27 (2015) 6046–6054.
- [72] L. Gao, Z.G. Zhang, L. Xue, J. Min, J. Zhang, Z. Wei, Y. Li, *Adv. Mater.* 28 (2016) 1884–1890.
- [73] B.B. Fan, L. Ying, Z.F. Wang, B.T. He, X.F. Jiang, F. Huang, Y. Cao, *Energy Environ. Sci.* 10 (2017) 1243–1251.
- [74] B. Fan, L. Ying, P. Zhu, F. Pan, F. Liu, J. Chen, F. Huang, Y. Cao, *Adv. Mater.* 29 (2017) 1606396.
- [75] Z. Li, X. Xu, W. Zhang, X. Meng, W. Ma, A. Yartsev, O. Inganäs, M.R. Andersson, R.A. Janssen, E. Wang, *J. Am. Chem. Soc.* 138 (2016) 10935–10944.
- [76] Z. Li, W. Zhang, X. Xu, Z. Genene, D. Di Carlo Rasi, W. Mammo, A. Yartsev, M.R. Andersson, R.A.J. Janssen, E. Wang, *Adv. Energy Mater.* 7 (2017) 1602722.
- [77] Z. Li, X. Xu, W. Zhang, X. Meng, Z. Genene, W. Ma, W. Mammo, A. Yartsev, M.R. Andersson, R.A.J. Janssen, E. Wang, *Energy Environ. Sci.* 10 (2017) 2212–2221.
- [78] J.W. Jung, J.W. Jo, C.C. Chueh, F. Liu, W.H. Jo, T.P. Russell, A.K. Jen, *Adv. Mater.* 27 (2015) 3310–3317.
- [79] Y.J. Hwang, G. Ren, N.M. Murari, S.A. Jenekhe, *Macromolecules* 45 (2012) 9056–9062.
- [80] Y.J. Hwang, B.A. Courtright, A.S. Ferreira, S.H. Tolbert, S.A. Jenekhe, *Adv. Mater.* 27 (2015) 4578–4584.
- [81] E. Zhou, J. Cong, M. Zhao, L. Zhang, K. Hashimoto, K. Tajima, *Chem. Commun.* 48 (2012) 5283–5285.
- [82] E. Zhou, J. Cong, K. Hashimoto, K. Tajima, *Adv. Mater.* 25 (2013) 6991–6996.
- [83] X. Li, P. Sun, Y. Wang, H. Shan, J. Xu, X. Song, Z. Xu, Z. Chen, *J. Mater. Chem. C* 4 (2016) 2106–2110.
- [84] L.W. Xue, Y.K. Yang, Z.G. Zhang, X.N. Dong, L. Gao, H.J. Bin, J. Zhang, Y.X. Yang, Y.F. Li, *J. Mater. Chem. C* 4 (2016) 5810–5816.
- [85] F. Liu, H. Li, Y. Wu, C. Gu, H. Fu, *RSC Adv.* 5 (2015) 92151–92158.
- [86] L. Ye, X. Jiao, H. Zhang, S. Li, H. Yao, H. Ade, J. Hou, *Macromolecules* 48 (2015) 7156–7163.
- [87] W. Lee, C. Lee, H. Yu, D.J. Kim, C. Wang, H.Y. Woo, J.H. Oh, B.J. Kim, *Adv. Funct. Mater.* 26 (2016) 1543–1553.
- [88] C. Lee, H. Kang, W. Lee, T. Kim, K.H. Kim, H.Y. Woo, C. Wang, B.J. Kim, *Adv. Mater.* 27 (2015) 2466–2471.
- [89] M.F. Falzon, A.P. Zoombelt, M.M. Wienk, R.A.J. Janssen, *Phys. Chem. Chem. Phys.* 13 (2011) 8931–8939.
- [90] W. Li, W.S.C. Roelofs, M. Turbiez, M.M. Wienk, R.A.J. Janssen, *Adv. Mater.* 26 (2014) 3304–3309.
- [91] Y. Yu, S. Zhou, X. Wang, C. Li, G. Feng, Y. Wu, W. Ma, W. Li, *Org. Electron.* 47 (2017) 133–138.
- [92] Z. Li, X. Xu, W. Zhang, Z. Genene, W. Mammo, A. Yartsev, M.R. Andersson,

- R.A.J. Janssen, E. Wang, *J. Mater. Chem. A* 5 (2017) 11693–11700.
- [93] H.Y. Chen, M. Nikolka, A. Wadsworth, W. Yue, A. Onwubiko, M. Xiao, A.J.P. White, D. Baran, H. Sirringhaus, I. McCulloch, *Macromolecules* 51 (2018) 71–79.
- [94] C. Dou, Z. Ding, Z. Zhang, Z. Xie, J. Liu, L. Wang, *Angew. Chem. Int. Ed.* 54 (2015) 3648–3652.
- [95] R. Zhao, C. Dou, Z. Xie, J. Liu, L. Wang, *Angew. Chem. Int. Ed.* 55 (2016) 5313–5317.
- [96] C. Dou, X. Long, Z. Ding, Z. Xie, J. Liu, L. Wang, *Angew. Chem. Int. Ed.* 55 (2015) 1436–1440.
- [97] Z.C. Ding, X.J. Long, C.D. Dou, J. Liu, L.X. Wang, *Chem. Sci.* 7 (2016) 6197–6202.
- [98] X. Long, Z. Ding, C. Dou, J. Zhang, J. Liu, L. Wang, *Adv. Mater.* 28 (2016) 6504–6508.
- [99] X.J. Long, Z.C. Ding, C.D. Dou, J. Liu, L.X. Wang, *Mater. Chem. Front.* 1 (2017) 852–858.
- [100] R. Zhao, Y. Min, C. Dou, J. Liu, L. Wang, *Chem-Eur. J.* 23 (2017) 9486–9490.
- [101] X. Long, N. Wang, Z. Ding, C. Dou, J. Liu, L. Wang, *J. Mater. Chem. C* 4 (2016) 9961–9967.
- [102] Z.G. Zhang, Y. Yang, J. Yao, L. Xue, S. Chen, X. Li, W. Morrison, C. Yang, Y. Li, *Angew. Chem. Int. Ed.* 56 (2017) 13503–13507.
- [103] H. Yao, F. Bai, H. Hu, L. Arunagiri, J. Zhang, Y. Chen, H. Yu, S. Chen, T. Liu, J.Y.L. Lai, Y. Zou, H. Ade, H. Yan, *ACS Energy Lett.* 4 (2019) 417–422.
- [104] X. Guo, A. Facchetti, T.J. Marks, *Chem. Rev.* 114 (2014) 8943–9021.
- [105] X. Guo, R.P. Ortiz, Y. Zheng, Y. Hu, Y.Y. Noh, K.J. Baeg, A. Facchetti, T.J. Marks, *J. Am. Chem. Soc.* 133 (2011) 1405–1418.
- [106] Y. Wang, Z. Yan, H. Guo, M.A. Uddin, S. Ling, X. Zhou, H. Su, J. Dai, H.Y. Woo, X. Guo, *Angew. Chem. Int. Ed.* 56 (2017) 15304–15308.
- [107] H. Sun, Y. Tang, C.W. Koh, S. Ling, R. Wang, K. Yang, J. Yu, Y. Shi, Y. Wang, H.Y. Woo, X. Guo, *Adv. Mater.* 31 (2019).
- [108] D. Mori, H. Benten, I. Okada, H. Ohkita, S. Ito, *Adv. Energy Mater.* 4 (2014) 1301006.
- [109] Y. Zhang, Y. Xu, M.J. Ford, F. Li, J. Sun, X. Ling, Y. Wang, J. Gu, J. Yuan, W. Ma, *Adv. Energy Mater.* 8 (2018) 1800029.
- [110] Y. Zhou, Q. Yan, Y.-Q. Zheng, J.-Y. Wang, D. Zhao, J. Pei, *J. Mater. Chem. A* 1 (2013) 6609–6613.
- [111] T. Earmme, Y.J. Hwang, N.M. Murari, S. Subramanyan, S.A. Jenekhe, *J. Am. Chem. Soc.* 135 (2013) 14960–14963.
- [112] K.D. Deshmukh, T. Qin, J.K. Gallaher, A.C.Y. Liu, E. Gann, K. O'Donnell, L. Thomsen, J.M. Hodgkiss, S.E. Watkins, C.R. McNeill, *Energy Environ. Sci.* 8 (2015) 332–342.
- [113] N.D. Eastham, A.S. Dudnik, T.J. Aldrich, E.F. Manley, T.J. Fauvell, P.E. Hartnett, M.R. Wasielewski, L.X. Chen, F.S. Melkonyan, A. Facchetti, R.P.H. Chang, T.J. Marks, *Chem. Mater.* 29 (2017) 4432–4444.
- [114] Y. Liu, J. Zhao, Z. Li, C. Mu, W. Ma, H. Hu, K. Jiang, H. Lin, H. Ade, H. Yan, *Nat. Commun.* 5 (2014) 5293.
- [115] H. Kang, M.A. Uddin, C. Lee, K.-H. Kim, T.L. Nguyen, W. Lee, Y. Li, C. Wang, H.Y. Woo, B.J. Kim, *J. Am. Chem. Sci.* 137 (2015) 2359–2365.
- [116] S.C. Veenstra, J. Loos, J.M. Kroon, *Prog. Photovoltaics* 15 (2007) 727–740.
- [117] N. Zhou, A.S. Dudnik, T.I.N.G. Li, E.F. Manley, T.J. Aldrich, P. Guo, H.-C. Liao, Z. Chen, L.X. Chen, R.P.H. Chang, A. Facchetti, M. Olvera de la Cruz, T.J. Marks, *J. Am. Chem. Sci.* 138 (2016) 1240–1251.
- [118] S. Fabiano, Z. Chen, S. Vahedi, A. Facchetti, B. Pignataro, M.A. Loi, *J. Mater. Chem.* 21 (2011) 5891–5896.
- [119] S. Fabiano, S. Himmelberger, M. Drees, Z. Chen, R.M. Altamimi, A. Salleo, M.A. Loi, A. Facchetti, *Adv. Energy Mater.* 4 (2014) 1301409.
- [120] H. Benten, D. Mori, H. Ohkita, S. Ito, *J. Mater. Chem. A* 4 (2016) 5340–5365.
- [121] H.C. Liao, C.C. Ho, C.Y. Chang, M.H. Jao, S.B. Darling, W.F. Su, *Mater. Today* 16 (2013) 326–336.
- [122] X. Liu, S. Huettner, Z. Rong, M. Sommer, R.H. Friend, *Adv. Mater.* 24 (2012) 669–674.
- [123] L. Ye, Y. Xiong, H. Yao, A. Gadisa, H. Zhang, S. Li, M. Ghasemi, N. Balar, A. Hunt, B.T. O'Connor, J. Hou, H. Ade, *Chem. Mater.* 28 (2016) 7451–7458.
- [124] Y. Xia, X. Xu, L.E. Aguirre, O. Inganäs, J. Mater. Chem. A 6 (2018) 21186–21192.
- [125] Y. Diao, Y. Zhou, T. Kuroswa, L. Shaw, C. Wang, S. Park, Y. Guo, J.A. Reinschbach, K. Gu, X. Gu, B.C.K. Tee, C. Pang, H. Yan, D. Zhao, M.F. Toney, S.C.B. Mannsfeld, Z. Bao, *Nat. Commun.* 6 (2015) 7955.
- [126] H. Ade, H. Stoll, *Nat. Mater.* 8 (2009) 281.
- [127] G. Li, Y. Yao, H. Yang, V. Shrotriya, G. Yang, Y. Yang, *Adv. Funct. Mater.* 17 (2007) 1636–1644.
- [128] Z. Li, X. Xu, W. Zhang, X. Meng, W. Ma, A. Yartsev, O. Inganäs, M.R. Andersson, R.A.J. Janssen, E. Wang, *J. Am. Chem. Soc.* 138 (2016) 10935–10944.
- [129] S. Günes, H. Neugebauer, N.S. Sariciftci, *Chem. Rev.* 107 (2007) 1324–1338.
- [130] C.H.Y. Ho, Q. Dong, H. Yin, W.W.K. Leung, Q. Yang, H.K.H. Lee, S.W. Tsang, S.K. So, *Adv. Mater. Interfaces* 2 (2015) 1500166.
- [131] C.J. Brabec, G. Zerza, G. Cerullo, S. De Silvestri, S. Luzzati, J.C. Hummelen, S. Sariciftci, *Chem. Phys. Lett.* 340 (2001) 232–236.
- [132] Y. Park, C. Fuentes-Hernandez, X. Jia, F.A. Larraín, J. Zhang, S.R. Marder, B. Kippelen, *Org. Electron.* 58 (2018) 290–293.
- [133] N.A. Mica, S.A.J. Thomson, I.D.W. Samuel, *Org. Electron.* 63 (2018) 415–420.
- [134] L. Zhang, B. Lin, Z. Ke, J. Chen, W. Li, M. Zhang, W. Ma, *Nano Energy* 41 (2017) 609–617.
- [135] Z. Zhao, Y. Duan, Q. Pan, Y. Gao, Y. Wu, Y. Geng, L. Zhao, M. Zhang, Z. Su, *J. Photochem. Photobiol. A* 375 (2019) 1–8.
- [136] X. Song, N. Gasparini, D. Baran, *Adv. Electron. Mater.* 4 (2018) 1700358.
- [137] E. von Hauff, V. Dyakonov, J. Parisi, *Sol. Energy Mater. Sol. Cells* 87 (2005) 149–156.
- [138] R. Steyrleuthner, R.D. Pietro, B.A. Collins, F. Polzer, S. Himmelberger, M. Schubert, Z. Chen, S. Zhang, H. Ade, A. Facchetti, D. Neher, *J. Am. Chem. Soc.* 136 (2014) 4245–4256.
- [139] A. Melianas, V. Pranculis, Y. Xia, N. Felekidis, O. Inganäs, V. Gulbinas, M. Kemerink, *Adv. Energy Mater.* 7 (2017) 1602143.
- [140] M.M. Mandoc, L.J.A. Koster, P.W.M. Blom, *Appl. Phys. Lett.* 90 (2007) 133504.
- [141] A. Pivrikas, N.S. Sariciftci, G. Juška, R. Österbacka, *Prog. Photovoltaics* 15 (2007) 677–696.
- [142] W. Tress, K. Leo, M. Riede, *Phys. Rev. B* 85 (2012) 155201.
- [143] J.T. Sheeh, C.H. Liu, H.F. Meng, S.R. Tseng, Y.C. Chao, S.F. Horng, *J. Appl. Phys.* 107 (2010) 084503.
- [144] P.H. Wöbbkenberg, D.D.C. Bradley, D. Kronholm, J.C. Hummelen, D.M. de Leeuw, M. Cölle, T.D. Anthopoulos, *Synthetic Met.* 158 (2008) 468–472.
- [145] T.M. Clarke, J. Peet, A. Nattestad, N. Drolet, G. Dennler, C. Lungenschmied, M. Leclerc, A.J. Mozer, *Org. Electron.* 13 (2012) 2639–2646.
- [146] S. Bertho, G. Janssen, T.J. Cleij, B. Conings, W. Moens, A. Gadisa, J. D'Haen, E. Goovaerts, L. Lutsen, J. Manca, D. Vanderzande, *Sol. Energy Mater. Sol. Cells* 92 (2008) 753–760.
- [147] J.M. Kroon, M.M. Wienk, W.J.H. Verhees, J.C. Hummelen, *Thin Solid Films* 403–404 (2002) 223–228.
- [148] S.A. Choulis, J. Nelson, Y. Kim, D. Poplavskyy, T. Kreouzis, J.R. Durrant, D.D.C. Bradley, *Appl. Phys. Lett.* 83 (2003) 3812–3814.
- [149] H. Yin, K.L. Chiu, C.H.Y. Ho, H.K.H. Lee, H.W. Li, Y. Cheng, S.W. Tsang, S.K. So, *Org. Electron.* 40 (2017) 1–7.
- [150] H. Yin, P. Bi, S.H. Cheung, W.L. Cheng, K.L. Chiu, C.H.Y. Ho, H.W. Li, S.W. Tsang, X. Hao, S.K. So, *Sol. RRL* 2 (2018) 1700239.
- [151] C.H.Y. Ho, S.H. Cheung, H.-W. Li, K.L. Chiu, Y. Cheng, H. Yin, M.H. Chan, F. So, S.-W. Tsang, S.K. So, *Adv. Energy Mater.* 7 (2017) 1602360.
- [152] K.R. Graham, C. Cabanatos, J.P. Jahnke, M.N. Idso, A. El Labban, G.O. Ngongang Ndjawa, T. Heumueller, K. Vandewal, A. Salleo, B.F. Chmelka, A. Amassian, P.M. Beaujuge, M.D. McGehee, *J. Am. Chem. Soc.* 136 (2014) 9608–9618.
- [153] Y. Lin, Q. He, F. Zhao, L. Huo, J. Mai, X. Lu, C.-J. Su, T. Li, J. Wang, J. Zhu, Y. Sun, C. Wang, X. Zhan, *J. Am. Chem. Soc.* 138 (2016) 2973–2976.
- [154] Q. Zhang, X. Xu, S. Chen, G.B. Bodedla, M. Sun, Q. Hu, Q. Peng, B. Huang, H. Ke, F. Liu, T.P. Russell, X. Zhu, *Sustain. Energy Fuels* 2 (2018) 2616–2624.
- [155] H. Yin, S. Chen, P. Bi, X. Xu, S.H. Cheung, X. Hao, Q. Peng, X. Zhu, S.K. So, *Organ. Electron.* 65 (2019) 156–161.
- [156] D. Zhao, Q. Wu, Z. Cai, T. Zheng, W. Chen, J. Lu, L. Yu, *Chem. Mater.* 28 (2016) 1139–1146.
- [157] J. Hou, O. Inganäs, R.H. Friend, F. Gao, *Nat. Mater.* 17 (2018) 119.
- [158] W. Li, L. Ye, S. Li, H. Yao, H. Ade, J. Hou, *Adv. Mater.* 30 (2018) 1707170.
- [159] M.A. Abkowitz, H.A. Mizes, J.S. Facci, *Appl. Phys. Lett.* 66 (1995) 1288–1290.
- [160] A.K. Jonscher, *J. Vac. Sci. Technol.* 8 (1971) 135–144.
- [161] L.J.A. Koster, E.C.P. Smits, V.D. Mihailescu, P.W.M. Blom, *Phys. Rev. B* 72 (2005) 085205.
- [162] Y.W. Tan, Y. Zhang, H.L. Stormer, P. Kim, *Eur. Phys. J-Spec. Top.* 148 (2007) 15–18.
- [163] H.T. Nicolai, M. Kuik, G.A. Wetzelar, B. de Boer, C. Campbell, C. Risko, J.L. Bredas, P.W. Blom, *Nat. Mater.* 11 (2012) 882–887.
- [164] J.C. Blakesley, H.S. Clubb, N.C. Greenham, *Phys. Rev. B* 81 (2010) 045210.
- [165] A. Mondon, M.N. Jawaid, J. Bartsch, M. Glatthaar, S.W. Glunz, *Sol. Energy Mater. Sol. Cells* 117 (2013) 209–213.
- [166] C.C. Koch, *Nanostruct. Mater.* 2 (1993) 109–129.
- [167] R. Noriega, J. Rivnay, K. Vandewal, F.P.V. Koch, N. Stingelin, P. Smith, M.F. Toney, A. Salleo, *Nat. Mater.* 12 (2013) 1038.
- [168] A. Salleo, *Mater. Today* 10 (2007) 38–45.
- [169] J.R. Yeargan, H.L. Taylor, *J. Appl. Phys.* 39 (1968) 5600–5604.
- [170] L. Pautmeier, R. Richert, H. Bässler, *Synthetic Met.* 37 (1990) 271–281.
- [171] S.W. Tsang, S.K. So, J.B. Xu, *J. Appl. Phys.* 99 (2006) 013706.
- [172] H. Yin, L.K. Ma, Y. Wang, J. Huang, H. Yu, J. Zhang, P.C.Y. Chow, W. Ma, S.K. So, H. Yan, *Adv. Mater.* 31 (2019) 1903998.
- [173] P. Bi, C.R. Hall, H. Yin, S.K. So, T.A. Smith, K.P. Ghiggino, X. Hao, *J. Phys. Chem. C* 123 (2019) 18294–18302.
- [174] H. Yin, C. Zhang, H. Hu, S. Karuthedath, Y. Gao, H. Tang, C. Yan, L. Cui, P.W.K. Fong, Z. Zhang, Y. Gao, J. Yang, Z. Xiao, L. Ding, F. Laquai, S.K. So, G. Li, *ACS Appl. Mater. Inter.* 11 (2019) 48095–48102.
- [175] H. Wu, H. Deng, M. Qin, H. Yin, T. Lau, P.W.K. Fong, Z. Ren, Q. Liang, L. Cui, H. Wu, X. Lu, W. Zhang, I. McCulloch, G. Li, *Mater. Today Energy* 12 (2019) 398–407.
- [176] H. Yin, J.K.W. Ho, S.H. Cheung, R.J. Yan, K.L. Chiu, X. Hao, S.K. So, *J. Mater. Chem. A* (6) (2018) 8579–8585.
- [177] H. Yin, S.H. Cheung, J.H.L. Ngai, C.H.Y. Ho, K.L. Chiu, X. Hao, H.W. Li, Y. Cheng, S.W. Tsang, S.K. So, *Adv. Electron. Mater.* 3 (2017) 1700007.
- [178] E. Kozma, D. Kotowski, M. Catellani, S. Luzzati, M. Cavazzini, A. Bossi, S. Orlandi, F. Bertini, *Mater. Chem. Phys.* 163 (2015) 152–160.
- [179] C. Yan, Y. Wu, J. Wang, R. Li, P. Cheng, H. Bai, Z. Zhan, W. Ma, X. Zhan, *Dyes Pigments* 139 (2017) 627–634.
- [180] H. You, D. Kim, H.-H. Cho, C. Lee, S. Chong, N.Y. Ahn, M. Seo, J. Kim, F.S. Kim, B.J. Kim, *Adv. Funct. Mater.* 28 (2018) 1803613.
- [181] J.H. Park, E.H. Jung, J.W. Jung, W.H. Jo, *Adv. Mater.* 25 (2013) 2583–2588.

- [182] T. Kurosawa, X. Gu, K.L. Gu, Y. Zhou, H. Yan, C. Wang, G.-J.N. Wang, M.F. Toney, Z. Bao, *Adv. Energy Mater.* 8 (2018) 1701552.
- [183] N. Gasparini, A. Salleo, I. McCulloch, D. Baran, *Nat. Rev. Mater.* 4 (2019) 229–242.
- [184] P. Bi, X. Hao, *Sol. RRL* 3 (2019) 1800263.
- [185] H. Yin, K.L. Chiu, P. Bi, G. Li, C. Yan, H. Tang, C. Zhang, Y. Xiao, H. Zhang, W. Yu, H. Hu, X. Lu, X. Hao, S.K. So, *Adv. Electron. Mater.* (2019) 1900497.
- [186] N. Zhou, A. Facchetti, *Mater. Today* 21 (2018) 377–390.
- [187] G. Wang, F.S. Melkonyan, A. Facchetti, T.J. Marks, *Angew. Chem. Int. Ed.* 58 (2019) 4129–4142.
- [188] H. Yin, J. Yan, J.K.W. Ho, D. Liu, P. Bi, C.H.Y. Ho, X. Hao, J. Hou, G. Li, S.K. So, *Nano Energy* 64 (2019) 103950.
- [189] S. Kirkpatrick, *Rev. Mod. Phys.* 45 (1973) 574–588.
- [190] J.W. Essam, *Rep. Prog. Phys.* 43 (1980) 833–912.
- [191] V.K.S. Shante, S. Kirkpatrick, *Adv. Phys.* 20 (1971) 325–357.
- [192] B. Bridge, *J. Mater. Sci. Lett.* 8 (1989) 102–103.
- [193] G. Ambrosetti, C. Grimaldi, I. Balberg, T. Maeder, A. Danani, P. Ryser, *Phys. Rev. B* 81 (2010) 155434.
- [194] R. Di Pietro, D. Fazzi, T.B. Kehoe, H. Sirringhaus, *J. Am. Chem. Soc.* 134 (2012) 14877–14889.
- [195] T. Kim, J. Kim, T.E. Kang, C. Lee, H. Kang, M. Shin, C. Wang, B. Ma, U. Jeong, T. Kim, B.J. Kim, *Nat. Commun.* 6 (2015) 8547.



Hang Yin is currently a Postdoctoral Research Scholar in Department of Physics, Hong Kong Baptist University. He received his Ph.D. degree supervised by Prof. Shu Kong So in Physics from Hong Kong Baptist University in 2017. His current research focuses on device physics and engineering of organic and perovskite solar cells.



Cenqi Yan received her Ph.D. degree in Mechanics (Advanced Materials and Mechanics) from Peking University in 2018 under the supervision of Prof. Xiaowei Zhan. Currently, she is a postdoctoral researcher in the Hong Kong Polytechnic University. Her current research interests are high-performance organic solar cells and perovskite solar cells.



Hanlin Hu received his Ph.D. degree from the Department of Materials Science and Engineering at the King Abdullah University of Science and Technology (KAUST), Jeddah, Kingdom of Saudi Arabia, in October 2017. Then, he worked as a postdoctoral fellow in Prof. Gang Li's group in the Department of Electronic and Information Engineering, at the Hong Kong Polytechnic University, Hong Kong. Now, he is an associate researcher in the college of materials science and engineering at Shenzhen University. His research interests include synchrotron based crystallography characterization, printing thin film solar cells and transistors.



Johnny K. W. HO is a PhD student in Physics under the supervision of Professor S. K. So at Hong Kong Baptist University. He will graduate with a doctoral degree in 2020. His research interests include electrical properties of organic semiconductors and organometallic hybrid perovskite materials as well as device physics of thin film transistors and organic photovoltaics. His current investigation focus is on indoor organic photovoltaics and perovskite transistors.



Xiaowei Zhan obtained a PhD degree in chemistry from Zhejiang University in 1998. He was then a postdoctoral researcher at the Institute of Chemistry, Chinese Academy of Sciences (ICCAS) from 1998 to 2000, and in 2000 he was promoted to Associate Professor at ICCAS. Dr Zhan worked in the University of Arizona and the Georgia Institute of Technology from 2002 to 2006 as a Research Associate and a Research Scientist. He has been a full professor at ICCAS since 2006. In 2012 he moved to Peking University. His research interests are in the development of materials for organic electronics and photonics. Prof. Zhan is a Highly Cited Researcher since 2017 and a Fellow of the Royal Society of Chemistry.



Gang Li is a Professor in the Department of Electronic and Information Engineering, Hong Kong Polytechnic University. His research interests are organic semiconductor and hybrid semiconductor materials, device engineering and physics for energy applications. He obtained BS degree from Wuhan University, MS and PhD degrees from Iowa State University. He was a research professor in UCLA, and VP of Solarmer Energy Inc. He is a Highly Cited Researcher since 2014, and most recently in the categories of Materials Science, Physics and Chemistry. He published ~110 papers, with over 50k citations. He is a Fellow of Royal Society of Chemistry.



Shu Kong So obtained his bachelor degree from Hamilton College and Ph.D. in Physics from Cornell University. In Cornell, he did research on surface physics and chemistry of small molecules on metal and semiconductor surfaces. He was a postdoctoral fellow in the Chemistry Department of the University of Toronto where he used scanning tunneling microscope to study surface photochemistry. In 1992, he joined the Department of Physics, Hong Kong Baptist University. Now he is a Professor of Physics. His major research interest is in the physics and the chemistry of thin film materials including transport and defect study of organic films, fabrication of organic solar cells and thin film transistors, surface and optical spectroscopies of materials,

and pulsed laser deposition.